RADAR CROSS SECTION ANALYSIS BY
SHOOTING AND BOUNCING RAYS METHOD

MUSTAFA KAĞAN ÇAKIR

SEPTEMBER 2015

RADAR CROSS SECTION ANALYSIS BY
SHOOTING AND BOUNCING RAYS METHOD

A THESIS SUBMITTED TO
THE GRADUATE SCHOOL OF NATURAL AND APPLIED SCIENCES
OF
MIDDLE EAST TECHNICAL UNIVERSITY

BY

MUSTAFA KAĞAN ÇAKIR

IN PARTIAL FULFILLMENT OF THE REQUIREMENTS
FOR
THE DEGREE OF DOCTOR OF PHILOSOPHY
IN
ENGINEERING SCIENCES

SEPTEMBER 2015

Approval of the thesis:

RADAR CROSS SECTION ANALYSIS BY
SHOOTING AND BOUNCING RAYS METHOD

submitted by **MUSTAFA KAĞAN ÇAKIR** in partial fulfillment of the requirements for the degree of **Doctor of Philosophy in Engineering Sciences Department, Middle East Technical University** by,

Prof. Dr. Gülbin Dural Ünver   _____
Dean, Graduate School of **Natural and Applied Sciences**

Prof. Dr. Murat Dicleli   _____
Head of Department, **Engineering Sciences**

Prof. Dr. Turgut Tokdemir   _____
Supervisor, **Engineering Sciences Dept., METU**

Examining Committee Members:

Prof. Dr. Yavuz Yaman   _____
Aerospace Engineering Dept., METU

Prof. Dr. Turgut Tokdemir   _____
Engineering Sciences Dept., METU

Assoc. Prof. Dr. Utku Kanoğlu   _____
Engineering Sciences Dept., METU

Assoc. Prof. Dr. Sabahattin Aykaç   _____
Civil Engineering Dept., Gazi University

Assist. Prof. Dr. Murat Demiral   _____
Mechanical Engineering Dept., Uni. of Turkish Aeronautical Assoc.

Date: 17/09/2015

I hereby declare that all information in this document has been obtained and presented in accordance with academic rules and ethical conduct. I also declare that, as required by these rules and conduct, I have fully cited and referenced all material and results that are not original to this work.

Name, Last name: Mustafa Kağan ÇAKIR

Signature   :

ABSTRACT

RADAR CROSS SECTION ANALYSIS BY
SHOOTING AND BOUNCING RAYS METHOD

Çakır, Mustafa Kağan

Ph.D., Department of Engineering Sciences

Supervisor: Prof. Dr. Turgut Tokdemir

September 2015, 121 pages

In this study, a MATLAB code incorporating `Shooting and Bouncing Rays (SBR) Method` is developed for calculating Radar Cross Section (RCS) of complex shapes. The code can calculate ray paths, magnetic current sheets, incident and scattered electric fields and RCS in horizontal, vertical and cross polarizations. While reflection effects are calculated by SBR algorithm, diffraction effects due to edges and corners are handled by `Equivalent Edge Currents (EEC's)`. Wave frequency, aspect angle and number of rays are the input parameters of the code. Primitive geometries can be generated and analyzed by the code. In case of complex shapes, the input to the program is generated by 3D CAD tools in STL format. Several conclusions drawn from the calculation results are presented.

ÖZ

SEKEN IŞIN YÖNTEMİ İLE
RADAR KESİT ALAN ANALİZLERİ

Çakır, Mustafa Kağan

Doktora, Mühendislik Bilimleri Bölümü

Tez Yöneticisi: Prof. Dr. Turgut Tokdemir

Eylül 2015, 121 sayfa

Bu çalışmada, Seken Işın Yöntemi (SIY) ile kompleks cisimlerin Radar Kesit Alanı`nı (RKA) hesaplayabilen bir MATLAB kodu hazırlanması amaçlanmıştır. Kod, ışın yollarını, yüzey akımlarını, gelen ve saçılan elektrik alanları ve dikey, yatay ve çapraz dalga polarizasyonlarındaki RKA değerlerini hesaplayabilmektedir. Gelen dalga frekansı, tarama açısı, polarizasyon ve ışın sayısı gibi parametreler, hazırlanan MATLAB koduna girdi oluşturmaktadır. RKA analizi yapılacak olan temel geometrik şekiller gelistirilen kod icinde oluşturulabilmekte, bunun yanında karmaşık geometriler ise 3D CAD programları aracılığı ile oluşturulup STL formatında MATLAB koduna girdi olarak tanıtilabilmektedir. Ayrıca, örnek çözümlemelerden elde edilen sonuçlar, tez çalışmasında sunulmuştur.

Anahtar Kelimeler: Seken Işın Yöntemi, Radar Kesit Alanı, RKA, Işın tüpü integrali

To my love Zeynep

ACKNOWLEDGMENTS

TABLE OF CONTENTS

LIST OF TABLES

TABLES

LIST OF FIGURES

FIGURES

CHAPTER 1

INTRODUCTION

1.1 Literature Review

James Clerk Maxwell formed the foundations of the classical theory of electromagnetism in 19th century. Main application scope of Maxwell equations is calculation of electromagnetic fields scattered from targets. Backscatter from military targets has been widely investigated since the beginning of World War II.

The principles of '*Radar*' are mainly based on Maxwell's equations. "Radar is an object-detection system that uses radio waves to determine the range, altitude, direction, or speed of objects. It can be used to detect aircraft, ships, cavitycraft, guided missiles, motor vehicles, weather formations, and terrain. The radar dish (or antenna) transmits pulses of radio waves or microwaves that bounce off any object in their path. The object returns a tiny part of the wave's energy to a dish or antenna that is usually located at the same site as the transmitter. The term RADAR was coined in 1940 by the United States Navy as an acronym for RAdio Detection And Ranging. The term radar has since entered English and other languages as a common noun, losing all capitalization.

Hertz proved that electromagnetic waves are reflected back from metallic and dielectric surfaces. Research and development studies on radar systems gained significance due to the tactical advantages obtained on the combat field of World War II. In radar applications, electromagnetic power scattered by the target is modeled in hypothetical field called the 'Radar Cross Section' (RCS). Today, calculating the RCS of a target is one of the important issues in radar engineering.

"The radar cross section (RCS) of a target is defined as the effective area intercepting an amount of incident power which, when scattered isotropically, produces a level of reflected power at the radar equal to that from the target. RCS calculations require broad and extensive technical knowledge, thus many scientists and scholars find the subject challenging and intellectually motivating. This is a very complex field that defies simple explanation, and any short treatment is only a very rough approximation.

The units of radar cross section are square meters; however, the radar cross section is NOT the same as the area of the target. Because of the wide range of amplitudes typically encountered on a target, RCS is frequently expressed in dBsm, or decibels relative to one square meter. The RCS is the projected area of a metal sphere that is large compared with the wavelength and that, if substituted for the object, would scatter identically the same power back to the radar. However, the RCS of all but the simplest scatterers fluctuates greatly with the orientation of the object, so the notion of an equivalent sphere is not very useful.

Different structures will exhibit different RCS dependence on frequency than a sphere. However, three frequency regimes are identifiable for most structures. In the Rayleigh region at low frequencies, target dimensions are much less than the radar wavelength. In this region RCS is proportional with the fourth power of the frequency. In the Resonance or Mie Region at medium frequencies, target dimensions and the radar wavelength are in the same order. The RCS oscillates in the resonance region. In the Optical Region of high frequencies, target dimensions are very large compared to the radar wavelength. In this region RCS is roughly the same size as the real area of target. The RCS behaves more simply in the high-frequency region. In this region, the RCS of a sphere is constant." **[32]**
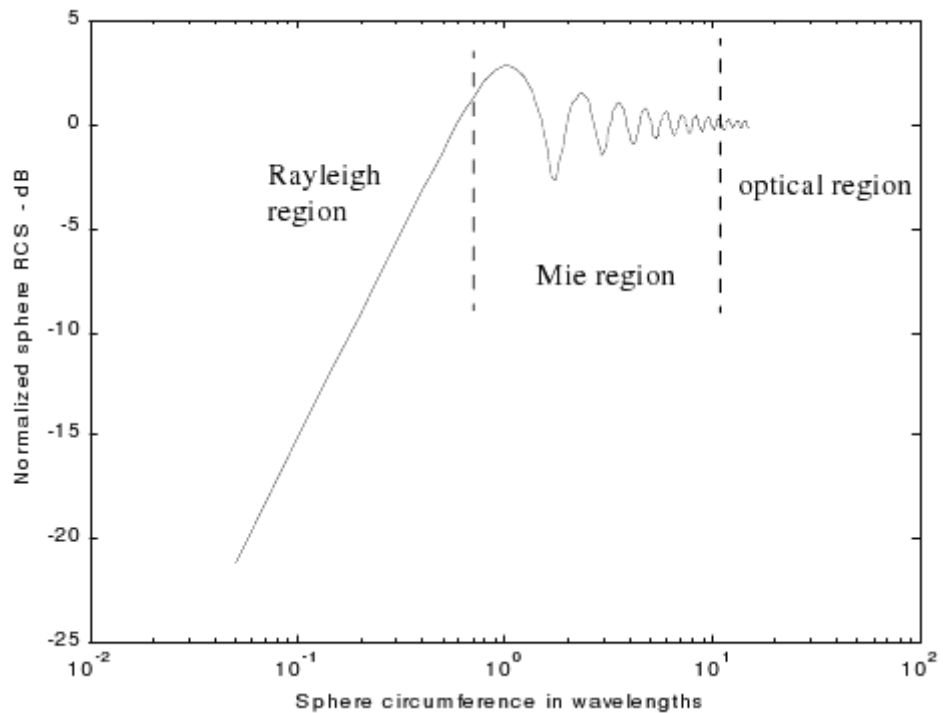
Figure 1 Normalized backscattered RCS for a perfectly conducting sphere using semi-log scale

Computational electromagnetics methods are based on numerical approaches of Maxwell equations which model interaction of physical targets and electromagnetic fields. In the last few decades this discipline has been critical for low observability technologies. Methods of this discipline have been widely adapted for problems such as antenna design and installation, radomme design, electromagnetic compatibility, RF parts design and bioelectromagnetism.

"In general, codes based on the methods-of-moments (MOM) solution to the electrical field integral equation (EFIE) are used to calculate scattering in the Rayleigh and resonance regions. Codes based on physical optics (PO) and the physical theories of diffraction (PTD) are used in the optical or high-frequency region. The target's electrical size (which is proportional to frequency and inversely proportional to the radar wavelength) that determines the appropriate algorithm to calculate the scattering. When the target length is less than 5 to 10 wavelengths, the

EFIE-MOM algorithm is used. Alternatively, if the target wavelength is above 5 to 10 wavelengths, the PO-PTD algorithm is used. **[32]**

Many different methods have been developed since World War II for calculating Radar Cross Section of complex shapes. In the earlier techniques, electromagnetic waves in the microwave frequency are assumed to obey the laws of optics. These approximate techniques are used in the solution of numerically large problems. Since these techniques are effective at high frequencies, they are called high frequency solution techniques. Among the high frequency techniques are Physical Optics (PO), Geometric Optics (GO), Physical Theory of Diffraction (PTD), Geometric Theory of Diffraction (GTD)) and Uniform Theory of Diffraction (UTD). In most of these approaches, diffraction effects have also been taken into consideration when modeling interaction of electromagnetic wave with the target. Among these methods, physical optics and geometric optics provide accurate predictions unless there exists sharp edges on the target. However, in case of sharp edges and corners, methods that neglect diffraction effects have large error percentages. Error percentages in optic methods depend on the shape of the target.
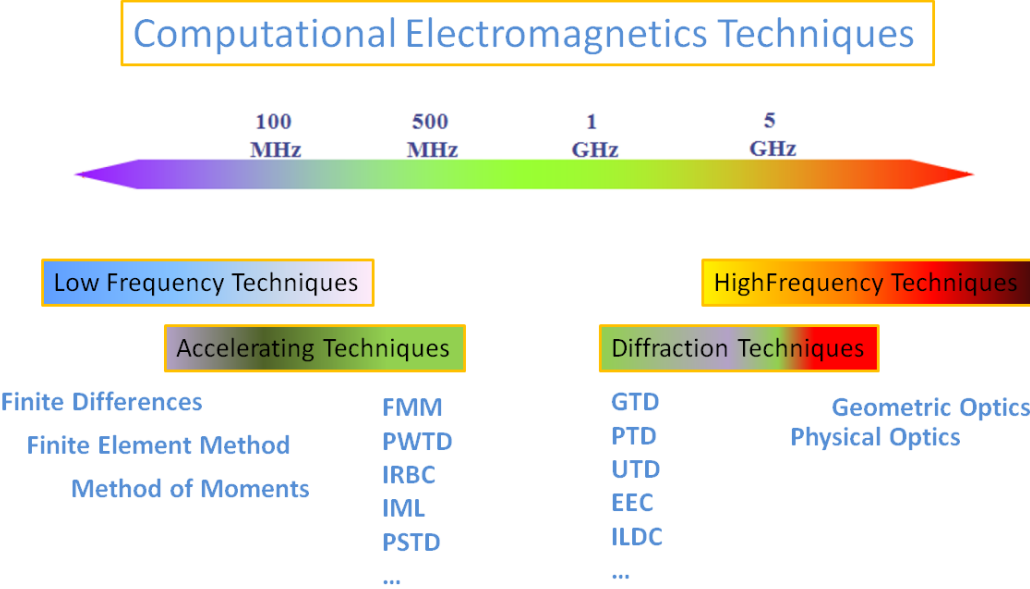
Figure 2 Computational Electromagnetics Techniques

4

Since 80's there has been a rapid increase in computational power of processing units. Correspondingly, new methods which reduce approximations in RCS calculations have been developed. Techniques developed for RCS calculations after 1980 are classified under two main groups. Basically, these techniques are high frequency techniques which adopt optical approaches and low frequency techniques which aims to solve the problem without any approximations.

Full wave techniques have been developed by the approach of numerical discretization of Maxwell equations. Methods of Moments, Finite Difference Time Domain and Finite Element Method. These techniques are sometimes called the low frequency techniques. Electrically large problems in GHz frequencies cannot be solved by these low frequency techniques. However, low frequency techniques model the interaction of the target and electromagnetic wave and the resulting percent error is generally much lower than what is dictated by most engineering approaches. Recently, new methods based on full wave solution have been developed. This new method is called the Multilevel Fast Multi Pole Method (MLFMM) and uses the Method of Moments formulation. The main difference from MoM is that MLFMM groups the main functions and calculates the interaction between these groups. Today, this method is used for electrical large and dielectric problems that are difficult to solve even with today's high computation power.

The most effective solution for high frequency problems is high frequency techniques supported by diffraction theories. In these techniques, single and multiple reflections, shadowing and diffraction effects are also considered. The contribution of diffraction is calculated by the Physical Theory of Diffraction. Recently, a new method called the Shooting and Bouncing Rays (SBR) method is developed. Multiple reflections can be handled with this method. SBR is method is composed of combination of GO and PO methods. Ray tracing technique is an appropriate method used for low observability design.

Multiple scattering plays a crucial role in RCS calculations. Cavities are locations where multiple scattering occurs mostly. The solution to this problem has been a main issue since multiple scatters around cavities have significant contributions on RCS.

In general, RCS of cavities is calculated by means of either modal analysis or full wave solution methods. For complex structures, neither modal analysis method nor full wave solution methods are not sufficient for solving electrically large problems. Shooting and Bouncing Rays (SBR) method for cavities first used by *Chou et al.* in 1989 in a project supported by NASA **[2]** In this method, rays are shot into the cavity and propagate in the cavity according to GO rules. Besides, material properties can be taken into consideration by this method **[2].**

In Geometric Optics, electromagnetic propagation is first represented with the reflection, refraction, and divergence of optical rays. The electromagnetic properties of magnitude, direction, and phase are then added on top of the ray traces to mimic the properties of waves. In Physical Optics, incident electromagnetic waves are converted into equivalent surface currents on the scattering surfaces of the structure under study, using the surface equivalence principles. The current is then integrated and re-radiated as electromagnetic waves towards the observation points everywhere in the computational domain **[1]**.
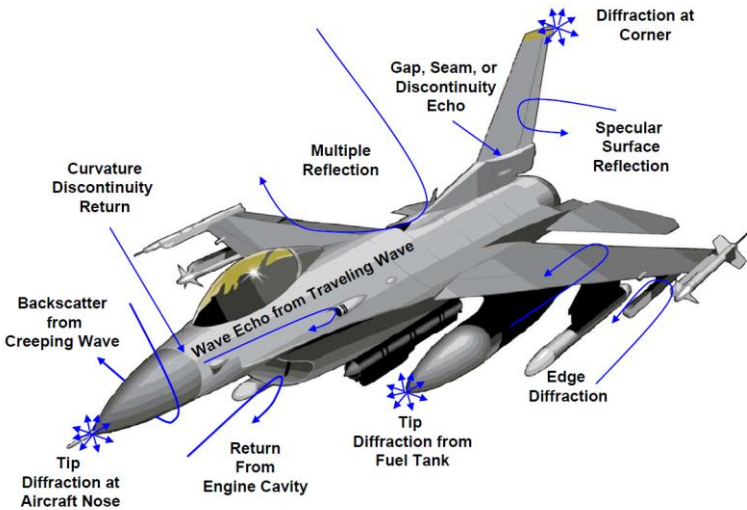
Figure 3 Various mechanisms contributing the Radar Cross Section (RCS) of an aircraft

Combining Geometric Optics and Physical Optics methods, PO-SBR begins the computation by launching numerous rays from the sources, usually antennas or regions of plane waves. The magnitude of the rays is dependent upon the pattern of

the source. Each ray then propagates through the computational domain and bounces between the target surfaces under study using the GO method. Next, the electromagnetic fields at each hit point are converted into surface currents using the PO methods and re-radiated towards all observation points. Finally, the fields at each observation point are summed up to represent the final electromagnetic field computed at the corresponding location of the computational domain. Although the optical approximation is not a precise electromagnetic theory compared to the full wave methods, asymptotic methods are able to provide a very fast and reasonable estimation of the field strength in presence of electrically large structures **[1]**.

Scattering from open ended rectangular cavities has been analyzed by two methods. These are 'waveguide modal analysis method' and 'shooting and bouncing rays method'. Cavity is defined according to waveguide modes whose electrical field is a known quantity. Unknown mode coefficients are determined by applying the Kirchoff approach and reciprocity relationship. The second approach is the ray tracing method **[3]** which also known as shooting and bouncing rays.

The solution to scattering from open ended waveguides and electromagnetic coupling problems has been investigated by *Pathak et al.* **[4]**. A relatively simple and efficient high-frequency analysis of electromagnetic modal reflection and transmission coefficients for waveguide discontinuities which are formed by joining different waveguide sections has been investigated. "The analysis extends the concept of geometrical theory of diffraction based equivalent edge currents and utilizes it in conjunction with the reciprocity theorem to describe interior (waveguide) scattering effects. It is noted that the previous use of equivalent edge currents was mostly restricted to exterior scattering by edged bodies, and its application to deal with interior scattering was limited to those guide geometries for which image theory could be used effectively to account for the interior wall effects. The present extension allows one to treat more general two and three-dimensional waveguide geometries provided the waveguide modes and their associated modal rays can be found explicitly. In particular, expressions for two-dimensional reflection and transmission coefficients are developed, and numerical results are shown for a flanged, semi-infinite parallel plate waveguide and for the junction between two

linearly tapered waveguides. One sample result is also shown for the reflection coefficient of a three-dimensional open-ended circular waveguide. Detailed expressions for three-dimensional waveguide discontinuities are being reported separately." **[4]**

As a result of the literature survey, it is concluded that there is a deviation between the results deduced from the computations conducted by SBR and modal analysis methods at low frequencies. Modal analysis method yields to accurate results at low frequencies whereas SBR at high frequencies. Other advantages of the SBR method are providing flexibility and applicability to problems whose waveguide modes cannot be determined easily.

Baldauf et al. modified the SBR method which was originally developed for cavities. In cavity structures, rays leaving the cavity are captured at the aperture. However, for the open scatterers, it is troublesome to determine the area where the electrical field integral is solved **[5]**. Baldauf proposes a cavity equivalent to the scatterer. With this proposition, the solution is similar to conventional PO method except for multiple reflections. In this study, the baseline of this method is explained by Huygens principle.

In this method, both basic and complex targets can be produces in STL (stereolithography) format. In STL mesh format, targets consist of triangular flat elements. Node coordinates and surface normal of triangular elements are clearly defined in this format.

Complex targets can be handled as a geometry consisting of triangular flat elements. Ray-triangle intersection test has significance as most of the computation time is spent for this intersection test. Basic intersection algorithms in the literature first calculate three planar boundaries and then tests whether the intersection point lies within the boundaries of the triangle. One of the most frequent methods used in SBR for ray-triangle intersection is Badouel algorithm and the other is *Moller-Trumbore* **[7]** algorithm.

In Badouel algorithm, the intersection of the ray with the plane that the triangle lies on is tested. If the ray is intersecting the plane, then the intersection point is tested

whether it lies inside the triangle or not. If the intersection point lies within the triangle, the intersection coordinates are calculated.

In Moller-Trumbore algorithm, since the intersection of the ray with the plane that the triangle lies on is not calculated, there is no need for the plane's equation parameters. Therefore, ray/triangle intersection test is accelerated. The most significant advantage of this method is efficient usage of the memory.

The asymptotic solution to the canonical problem of scattering of planar waves from perfectly electric conducting cylinder has been investigated by *Pathak* **[8]** and 'Uniform Theory of Diffraction (UTD)' has been proposed as the solution. Pathak solved the problem of scattering of planar waves from perfectly electric conducting cylinder in a manner similar to the method of Fock and by means of heuristic approaches he converted the total field into a uniform field. This solution is also valid for surface boundary layer transition zone. Fock also developed an asymptotic theory that investigates the diffraction of waves at large convex surfaces and proposed the solution in the shape of a canonic integral.

Paknys **[9]**. investigated the radar cross section of the large rectangular shaped cavity embedded inside a finite cylinder. The geometry used in this analysis has also been used for analyzing cockpit like structures in air vehicle. Aperture Integration method has been used for analysis of waveguide modes propagating in cavity. Creeping wave effects have been calculated by 'Geometric Theory of Diffraction'. Diffractions outside the cylinder have been handled by the 'Theory of Equivalent Edge Waves'.

1.2 Overview of the Thesis

In this thesis study, basic SBR code is developed by MATLAB[®]. This code has been applied for open end scatterers for which the selected aperture is critical for the aperture integral. If the electromagnetic field values at the exit aperture are exactly known, far field RCS results can be acquired without considering the selected exit aperture. Huygens principles are applied to determine the electromagnetic field at the exit aperture. According to these principles it is assumed that the scattering surface is

contained by a surface called the Huygens surface. Equations of Huygens surface hypothesis has been used for numerical integration on the aperture surface. Results obtained from this code have been compared with the results obtained from PO methods. SBR can automatically handle shadowing and multiple bounce problems by means of ray tracing capability. However, since SBR algorithm does not consider diffraction effects, SBR code shall be supported by Physical Theory of Diffraction (PTD) or Uniform Theory of Diffraction (UTD) to achieve more accurate computation results.

The broadest method in the literature which can handle edge diffraction effects is the *Micheali*'s method **[10]**. In this study, Micheali formulated the 'Equivalent Edge Waves' and claimed that diffraction effects can be solved by using them inside a linear radiance integral presented by Thomas Young almost 300 years ago. Although, Micheali, himself, did not perform any software applications, there have been numerous researchers using his method of 'Equivalent Edge Waves' for RCS analysis.

1.3 Outline of the Thesis

In the 2nd chapter of this thesis study, formulation of the basic SBR method has been investigated. Also, ray-triangle intersection test has been analyzed by different methods and a new accelerated ray-triangle intersection test method has been investigated and compared by other conventional methods. In the last phase of the code, Huygens principles are made use of in the scattered field analysis and explained in detail. The code developed by using MATLAB has been tested on targets like square plate, cube and cylinder.

In the 3rd chapter of the study SBR code developed has been used to verify RCS of complex targets such as F117, Eurofighter and F16 aircrafts.

In the 4th chapter, Physical Theory of Diffraction (PTD) – Equivalent Edge Waves method has been superposed on SBR and diffraction effects have been investigated.

In the 5th chapter, a case study on modelling a generic cockpit geometry of an air vehicle has been investigated. Cockpit geometry has been analyzed by using SBR and uniform theory of diffraction.

CHAPTER 2

SHOOTING AND BOUNCING RAYS METHOD

In this chapter, Shooting and Bouncing Rays (SBR) method is explained. SBR algorithm defined in this section is a ray based technique capable of calculating Radar Cross Section of perfectly electric conducting targets. This technique is also applied to electromagnetic scattering and antenna radiation problems. Basically, the algorithm is composed of ray tracing, amplitude tracing and aperture integration parts.

Main blocks of the algorithm are defined in following sections: 'Definition of the Ray', 'Ray-Triangle Intersection Test' and 'Reflected Ray' .In section 2.1 SBR analysis results for problems such as scattering from cavities and simple and complex targets are provided. Numerical results of the SBR code are compared with results obtained by Physical Optics (PO). Benefits and drawbacks of these two methods are also explained.

2.1 Shooting and Bouncing Ray Method Formulation

Shooting and Bouncing Ray (SBR) Method is based on principles of geometric optics **[2]**. Scattering analysis are performed on 3 levels. First, SBR traces the hit points and updates the incident electromagnetic fields from the source onto those hit points. Next, PO paints the equivalent surface current using the surface equivalence theory. The re-radiations of the surface currents from all hit points are then collected and summed at the desired observation points. And finally, the source radiates directly towards the observation points using SBR, and the resulting fields are added on top of the summation from the surface currents to become the final field solution at the observation points. In this step, scattered field is calculated by ray tube integration method according to Huygens principles.

SBR has two main advantages against PO. First, shadowing effects are naturally taken into consideration while in PO there is serious effort to calculate shadow effects. The second and more significant advantage is the ability of SBR to calculate multiple bounce effects whereas PO does not have that capability.
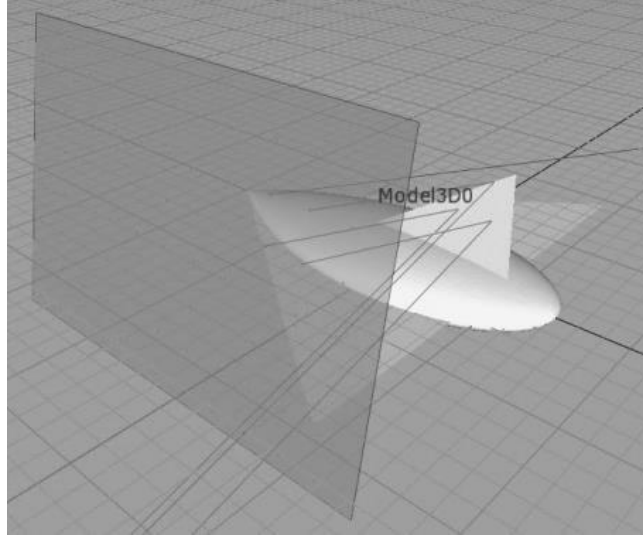
Figure 4 Incident wave illuminating the target

2.1.1 Ray Definition

In order to perform SBR analysis, a stack of parallel rays shall be produced in order to mimic incident wave. Origin vector of each ray is defined as follows:

$$\overline{O} = \overline{O}_{origin} = x_0 \hat{x} + y_0 \hat{y} + z_0 \hat{z} \qquad (2.1)$$

The direction vector of the ray is:

$$\hat{D} = x_d \hat{x} + y_d \hat{y} + z_d \hat{z} \quad \text{where;} \ x_d^2 + y_d^2 + z_d^2 = 1 \qquad (2.2)$$

The directional components of the incident waves in Cartesian coordinate system are as follows:

$$x_d = -sin\theta^i cos\emptyset^i \ , \quad y_d = -sin\theta^i sin\emptyset^i$$

and $z_d = -cos\emptyset^i$
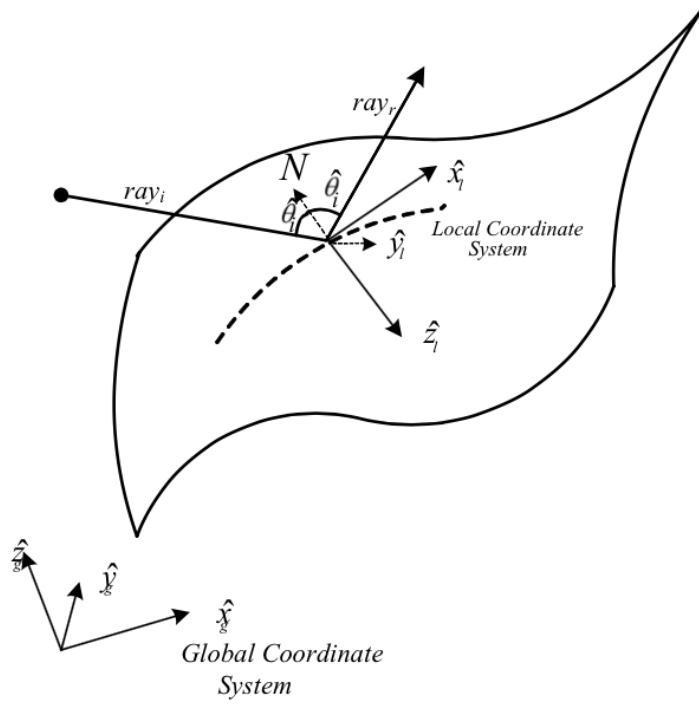
Figure 5 Incident ray intersecting the target surface

Ray equation defined by the origin vectors is as follows:

$$\bar{R}(t) = \bar{O} + t\widehat{D} \tag{2.3}$$

$$(x_1, y_1, z_1) = (x_0, y_0, z_0) + (x_d, y_d, z_d)t \tag{2.4}$$

denotes the coordinates of the ending point. In above equations, t denotes time, $\bar{R}(t)$

2.1.2 Ray-triangle intersection tests and reflected ray

This phase includes calculations of reflection plane, surface normal, reflection point, distance from reflection point to the origin of the ray, amplitude and phase of

incident ray, reflection and transmissivity vectors, field magnitudes corresponding to reflecting and transmitted rays.

When the ray reaches the target surface, ray-triangle intersection test shall be realized. If there is an intersection, plane of reflection, reflection and transmission vectors and point of reflection are found. Exact locations of the reflection and diffraction are necessary for calculating polarization components and traces of reflecting and diffracting fields.

"Algorithms solving ray-triangle intersection test, simply calculates the intersection with three boundary planes defining the size of the triangle and then tests whether the intersection point is inside edges of the triangle or not." **[11]** This approach requires a significant amount of storage space.

Fig. 6 shows the boundary planes (i.e. plane AB, plane BC and plane CA) of triangle ABC.
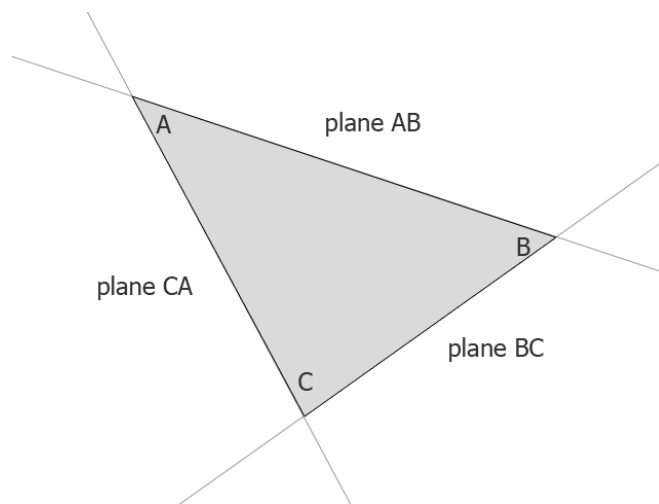
Figure 6 Boundary Planes of a Triangle

Ray-triangle intersection test has two logical sequences:

- The distance from the origin of the ray to the intersection point of ray end triangle is calculated. This is called the distance test.

- Whether the ray-triangle intersection point lies within the triangle or not is tested. This is called the aperture test.

In this study, three algorithms governing ray-triangle intersection have been used. These are Badouel's algorithm [6], Moller-Trumbore algorithm [7] and Plucker algorithm [11].

2.1.2.1 Badouel Method

The scattering surface is defined by the equation $z = f(x, y)$. Intersection point on the ray and plane is determined by simultaneously solving plane and ray equations as shown in Figure 7.
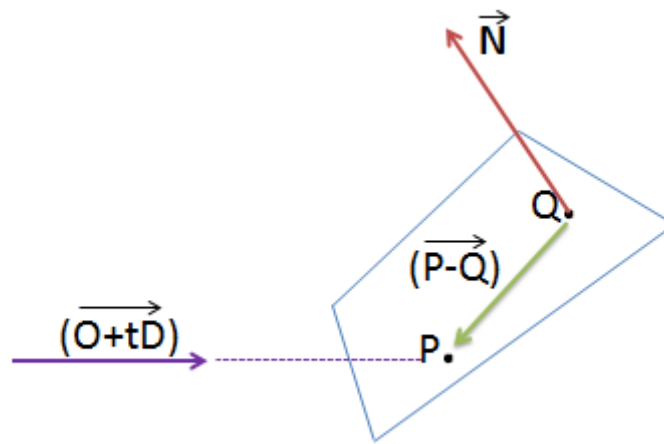
Figure 7 Ray and the plane on which the triangle lies

For instance, if the scattering surface is a flat plate, the intersection point is determined as follows. Plane is defined by a point (Q) on it and the unit normal vector ($\vec{N}$).

Since the dot product of two perpendicular vectors is equal to zero, for any point (P) on the plane following equation can be written,

$$\vec{N} \cdot \overrightarrow{(P - Q)} = 0 \tag{2.5}$$

The following equation is obtained by simultaneously solving ray and the plane equations:

$$\vec{N} \cdot \overrightarrow{(O + tD - Q)} = 0 \tag{2.6}$$

Here t is defined as

$$t = \frac{\vec{N}\overrightarrow{(Q-O)}}{\vec{N}\cdot\vec{D}} \tag{2.7}$$

Shape of the basic geometries like plate, sphere or cylinder can be defined by one single equation. Complex geometries can be handled by treating them as combination of triangular flat plates. In this case, intersection of a triangle and ray is more complicated than primitive geometries. "Basically, ray-triangle intersection test is applied in two steps:

- Intersection of the ray and the plane of the triangle
- Checking whether the intersection point lies within the triangle or not." [11]

Ray-triangle intersection is explained by equations 2.5 thru 2.7. After defining the intersection point, it is decided whether the point lies inside the triangle or not. Triangle is defined by corners p0, p1 and p2 as shown in Figure 8. The unit normal vector ($\vec{n}$) is defined by the right hand rule and expressed as follows:

$$\vec{n} = \overrightarrow{(p_1 - p_0)} \times \overrightarrow{(p_2 - p_0)} \tag{2.8}$$
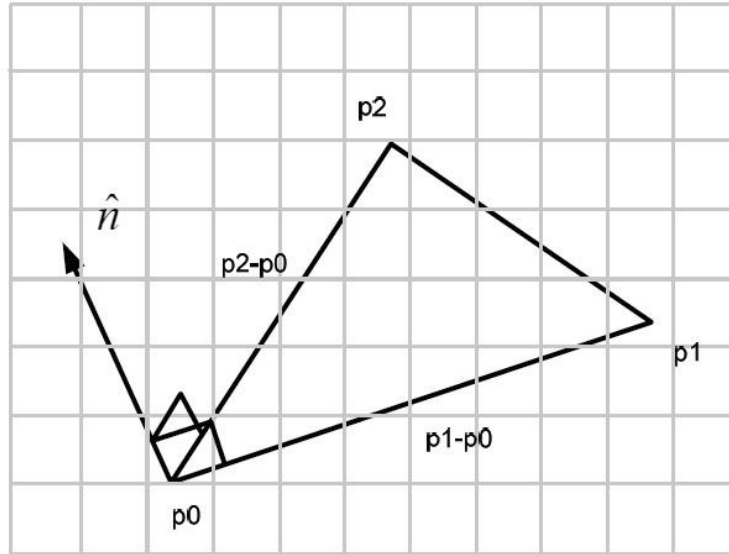
Figure 8 Triangle defined by the right hand rule

The triangle is the intersection of 3 planes as shown in Figure 6. Provided that the point is at the right side of the each line (edge) then the point lies inside the triangle.

Using this definition, if a point is at the left hand side of each edge then the point is outside the triangle. By means of vector multiplication and using the equations 2.9 thru 2.11 it can be decided whether point *P* (ray-traingle intersection point) is at the right hand or left hand side of the specific edge.

Since three corners of the triangle and the intersection point lies on the 3D space, vector multiplication is the best way to calculate the clockwise (CW) / counterclockwise (CCW) directions. The unit normal vector ($\hat{n}$) shall be perpendicular to and outward the surface. The following equations shall be satisfied in order the point to be inside the triangle:

$$\left| \overrightarrow{(p_1 - p_0)} \times \overrightarrow{(x - p_0)} \right| \cdot \vec{n} \geq 0 \tag{2.9}$$

$$\left| \overrightarrow{(p_2 - p_1)} \times \overrightarrow{(x - p_1)} \right| \cdot \vec{n} \geq 0 \tag{2.10}$$

$$\left| \overrightarrow{(p_0 - p_2)} \times \overrightarrow{(x - p_2)} \right| \cdot \vec{n} \geq 0 \tag{2.11}$$
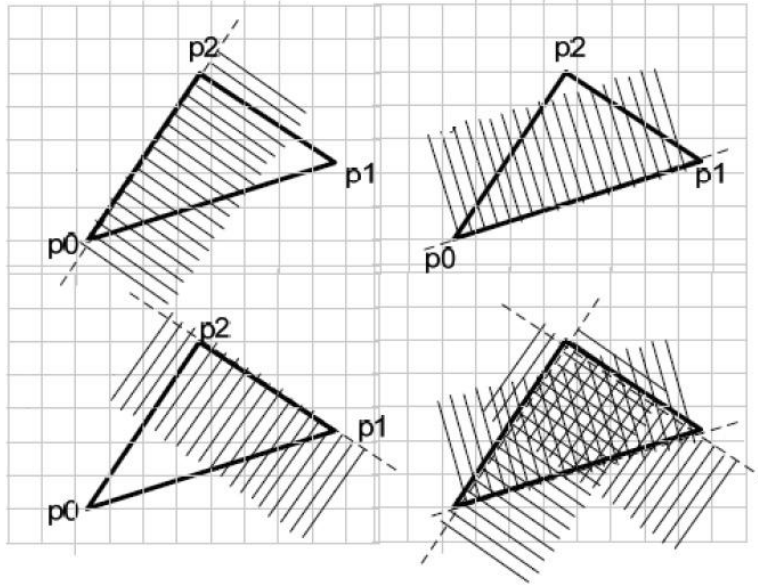
Figure 9 Method of testing whether a point is inside the triangle or not

2.1.2.2 Moller-Trumbore Method

This method yields to a faster algorithm since there is no need for the surface equation. Moller-Trumbore Method can be expressed as follows:

Ray *R(t)* with origin *O* and normalized direction *D* can be defined as follows:

$$\vec{R}(t) = \vec{O} + t\vec{D} \qquad\qquad (2.12)$$

Say the corners of the triangle are P_0, P_1 and P_2 respectively. *t* is the intersection distance and (u,v) are the coordinates at the intersection point.

2.1.2.2.1 Intersection Algorithm

A point T (*u, v*) on the triangle is defined by the following equation:

$$T(u,v)=(1-u-v)P_0+uP_1+vP_2 \qquad\qquad (2.13)$$

where *(u,v)* are baricentric coordinates, $u \geq 0$, $v \geq 0$ and $u + v \leq 1$ must be satisfied. When calculating the intersection between ray *R(t)* and triangle *T(u,v)*, *R(T)=T(u,v)* equation must be satisfied and defined as follows:

$$O+tD = (1-u-v)P_0+uP_1+vP_2 \tag{2.14}$$

This equation can also be defined as follows:

$$[-D, \quad P_1 - P_2, \quad P_2 - P]\begin{bmatrix} t \\ u \\ v \end{bmatrix} = O - P_0 \tag{2.15}$$

The distance (t) between the ray's origin and intersection point and its baricentric coordinates can be determined by solving the linear system of equations given in **Eq. 2.15.**
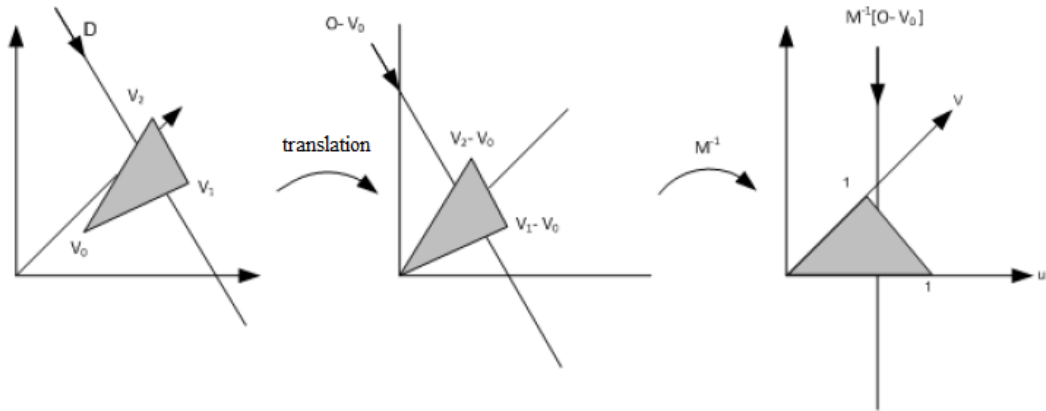
Figure 10 Translation of the ray's origin

In Figure 10, M=[-D, V_1-V_0, V_2-V_0] is the matrix in Eq. 2.15.

Given E_1= P_1-P_0, E_2= P_2-P_0 and T=O-P_0, Eq. 2.15 can be solved by Kramer's rule.

$$\begin{bmatrix} t \\ u \\ v \end{bmatrix} = \frac{1}{|-D \quad E_1 \quad E_2|}\begin{bmatrix} T & E_1 & E_2 \\ -D & T & E_2 \\ -D & E_1 & T \end{bmatrix} \tag{2.16}$$

21

$|A \quad B \quad C| = -(A \times C) \cdot B = -(C \times B) \cdot A$ equation is known from linear algebra and can be solved Eq. 2.16 can be arranged as follows:

$$\begin{bmatrix} t \\ u \\ v \end{bmatrix} = \frac{1}{(D \times E_2) \cdot E_1} \begin{bmatrix} (T \times E_1) \cdot E_1 \\ (D \times E_2) \cdot T \\ (T \times E_1) \cdot D \end{bmatrix} = \frac{1}{P \cdot E_1} \begin{bmatrix} Q \cdot E_2 \\ P \cdot T \\ Q \cdot D \end{bmatrix} \qquad (2.17)$$

where; P=(D x E_2) and Q=(T x E_1)

2.1.2.3 Plucker Test Method

Another method used to accelerate ray-triangle intersection test is the Plucker test. This test is faster than Moller-Trumbore test. Main idea of the Plucker test is to store the ray's coordinates (i.e. origin and direction) and the edges of the triangle in Plucker coordinates. In Plucker method, first the intersection distance parameter and then intersection point is calculated [11].
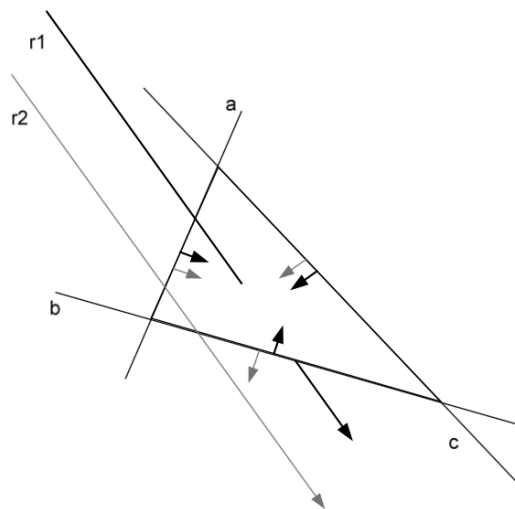
Figure 11 Illustration of Plucker Test

22

In Figure 11 a, b and c show the edges of the triangle. Since, all the black arrows attached to the edges of the triangle are directed towards the ray *r1* and towards inside of the triangle, it can be concluded that the ray intersects the triangle. All the grey arrows attached to the edges of the triangle are directed towards the ray *r2* but not all of them are directed towards inside of the triangle, it can be concluded that the ray does not intersect the triangle.

The general strategy of the methods in the literature is first to perform the distance test and pass to the aperture test if the distance test fails. The Plucker algorithm performs a fast aperture test that makes use of the Plucker coordinates along with distance calculations. The following section explains the Plucker coordinates.

2.1.2.3.1 Plucker Coordinates

Plucker coordinates developed by Julius Plucker in 19th century, is a method that assigns 6 homogenous coordinates for each line in the projective 3D space (P^3).

2.1.2.3.2 Geometric Intuition

In the 3 dimensional Euclid space, line L is defined by two points or two planes containing the points.
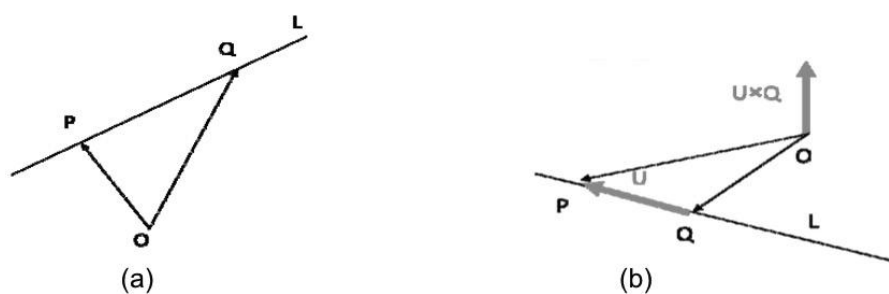
Figure 12 (a) Representation of two points in a line **(b)** Representation of direction and moments of two points on the line

The displacement vector from point $P = (p_1, p_2, p_3)$ to point $Q = (q_1, q_2, q_3)$ is different from 0 as long as the points are not collocated. The displacement vector

also shows the direction of the line. Each displacement between the points on Line L is given by the scalar multiplication of $U=P-Q$. If a physical particle having a unit mass is moved from point P to point Q then it has a moment about the origin. This moment is equal to the cross product of the U and Q. The area of the triangle OPQ is proportional to the distance between P and Q which is considered as the triangle's base and the area doe no change if the triangle is moved along the line. The moment vector V is perpendicular to the displacement as stated in its definition hence $U \cdot V = 0$.

$(U{:}V) = (u_1{:}\ u2{:}\ u3{:}\ v1{:}\ v2{:}\ v3)$ are homogeneous coordinates of L.

2.1.2.3.3 Algebraic Definition

In the 3D projective space (P^3), line L includes point P and point Q with homogeneous coordinates ($p_x{:}\ py{:}\ pz{:}\ 1$) and ($q_x{:}\ qy{:}\ qz{:}\ 1$) respectively. These coordinates when embedded into the columns of M, a matrix of 4 x 2 is formed.

$$M = \begin{bmatrix} p_x & q_x \\ p_y & q_y \\ p_z & q_z \\ 1 & 1 \end{bmatrix} \tag{2.18}$$

Since *P* and *Q* are different points, the columns of *M* are linearly independent and rank 2. Plucker coordinates of line L is defines as follows:

L={P-Q: P×Q}

$$\underbrace{\begin{vmatrix} p_x & q_x \\ 1 & 1 \end{vmatrix} \begin{vmatrix} p_y & q_y \\ 1 & 1 \end{vmatrix} \begin{vmatrix} p_z & q_z \\ 1 & 1 \end{vmatrix}}_{P\text{-}Q} \quad \underbrace{\begin{vmatrix} p_y & q_y \\ p_z & q_z \end{vmatrix} \begin{vmatrix} p_z & q_z \\ p_x & q_x \end{vmatrix} \begin{vmatrix} p_z & q_z \\ p_y & q_y \end{vmatrix}}_{P \times Q} \tag{2.19}$$

The Plucker coordinates of A, B and C edges of the triangle are expressed using following 18 coefficients, where (x_0,y_0,z_0), (x_1,y_1,z_1) and (x_2,y_2,z_2) are the coordinates of the corners respectively [12].

Table 1 Coefficients for Plucker Test

A	B	C
$A_0 = x_0 y_1 - x_1 y_0$	$B_0 = x_1 y_2 - x_2 y_1$	$C_0 = x_2 y_0 - x_0 y_2$
$A_1 = x_0 z_1 - x_1 z_0$	$B_1 = x_1 y_2 - x_2 y_1$	$C_1 = x_2 z_0 - x_0 z_2$
$A_2 = x_0 - x_1$	$B_2 = x_1 z_2 - x_2 z_1$	$C_2 = x_2 - x_0$
$A_3 = y_0 z_1 - y_1 z_0$	$B_3 = y_1 z_2 - y_2 z_1$	$C_3 = y_2 z_0 - y_0 z_2$
$A_4 = z_0 - z_1$	$B_4 = z_1 - z_2$	$C_4 = z_2 - z_0$
$A_5 = y_1 - y_0$	$B_5 = y_2 - y_1$	$C_5 = y_0 - y_2$

Following equations can be deduced from Table 1:

$$A_2 + B_2 + C_2 = x_0 - x_1 + x_1 - x_2 + x_2 - x_0 = 0 \qquad\qquad \textbf{(2.20)}$$

$$A_4 + B_4 + C_4 = z_0 - z_1 + z_1 - z_2 + z_2 - z_0 = 0 \qquad\qquad \textbf{(2.21)}$$

$$A_5 + B_5 + C_5 = y_1 - y_0 + y_2 - y_1 + y_0 - y_2 = 0 \qquad\qquad \textbf{(2.22)}$$

Equations above yield:

$$C_2 = -A_2 - B_2 \qquad\qquad \textbf{(2.23)}$$

$$C_4 = -A_4 - B_4 \qquad\qquad \textbf{(2.24)}$$

$$C_5 = -A_5 - B_5 \qquad\qquad \textbf{(2.25)}$$

As a result, for a triangle only 15 coefficients are enough instead of 18 coefficients yielding a memory saving 20 %. Non-normalized unit normal vector of the triangular surface can be defined as follows [13].
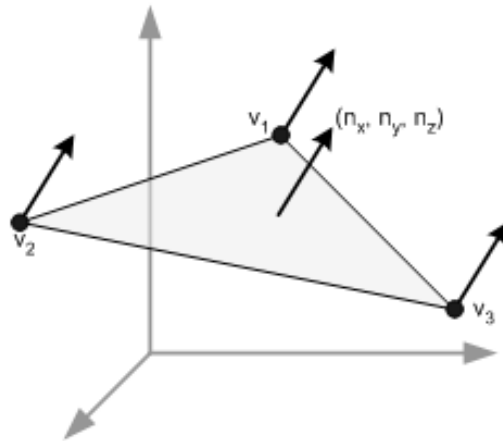
Figure 13 Unit normal vector components of a triangle

$$n_x = A_3 + B_3 + C_3 \tag{2.26}$$

$$n_y = -A_1 - B_1 - C_1 \tag{2.27}$$

$$n_z = A_0 + B_0 + C_0 \tag{2.28}$$

2.1.2.3.4 Basics of the Plucker Test

"Plucker coordinates are an alternate way of describing directed lines in three space using six numbers **[11]**. By performing a six dimensional permuted inner product of these numbers we can determine whether two directed lines intersect (the inner product is 0.0) or whether one passes to one side or the other (depending on the sign of the inner product). These three possibilities are illustrated in figure 14." **[11]**
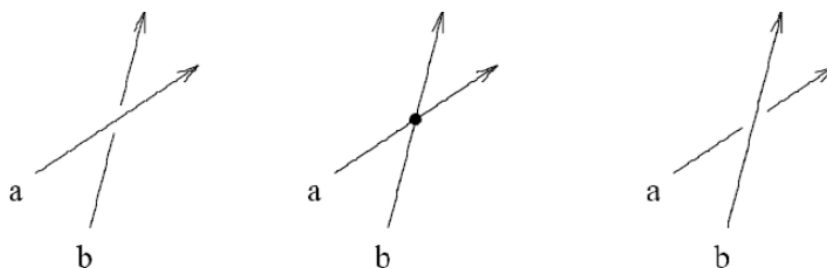
Figure 14 Three possibilities for two directed lines whether one passes to one side or the other (depending on the sign of the inner product).

By determining on which side a line passes with respect to another we can determine if a ray passes through a triangle **[11]**.

So if 6-dim vectors defining edges and a ray are:

$$e_0 = \{p - p_0, p \times p_0\} \tag{2.29}$$

$$e_1 = \{p_1 - p, p_1 \times p\} \tag{2.30}$$

$$e_2 = \{p_0 - p_1, p_0 \times p_1\} \tag{2.31}$$

$$R = \{d \times o, d\} \tag{2.32}$$

Ray intersection test is performed by checking whether the dot products of the following 6 dimensional vectors have the same sign or not.

$$t_0 = (e_0, R), \ t_1 = (e_1, R), \ t_2 = (e_2, R) \tag{2.33}$$
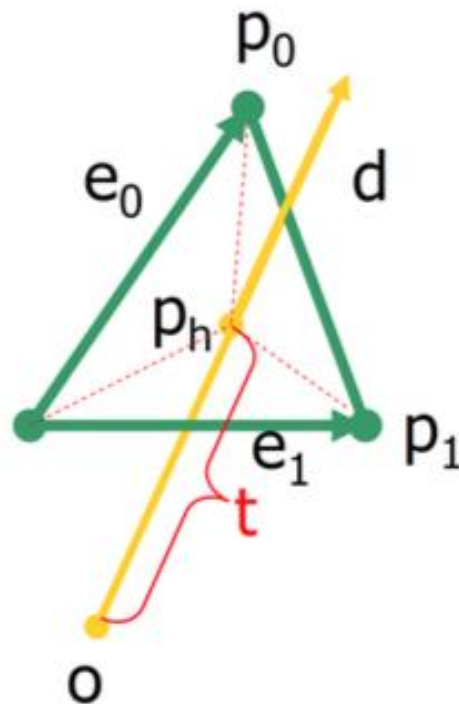
Figure 15 Ray-Triangle Intersection Algorithm finds whether intersection point p_h exists. If yes, computes the u, v parameters of intersection (such as $p_h = p + e_0 \cdot u + e_1 \cdot v$) as well as distance $t = \{o, p_h\}$.

Fast test is performed by pre-calculation and storage of the triangle edges in Plucker coordinates.

2.1.2.3.5 Intersection Algorithm

In the following sections, accelerating techniques for ray-triangle intersection test with Plucker coordinates. First, necessary amount of calculation during rendering process, and how it's reduced is explained in detail. Second, Plucker test which used for data processing, in the previous section is explained. Finally, whole intersection test is described.

2.1.2.3.5.1 Pre-calculated Triangle Data

In the pre-processing phase, all the information about the tringle is based on indexing the coordinates of normalized unit normal vector, corner p and two edges (e_0 and e_1).

2.1.2.3.5.1.1 Storing the Unit Normal Vector

The unit normal vector of the triangle is defined as follows: $\hat{n} = (n_0, n_1, n_2)$. One of the perpendicular components is assumed to be equal to 1 and since the defined intersection algorithm does not include any perpendicular length, there is no need to store it. Similar to the projection test, the perpendicular component with the largest amplitude is chosen and all the proper values can be scaled by the inverse of this component.

$$n_w = \max(\text{abs}(n_i)) \quad \text{where i=0,1,2} \tag{2.34}$$

Then the last two remaining components can be determined:

$$n_u = n_u/n_w \tag{2.35}$$
$$n_v = n_v/n_w \tag{2.36}$$

where $u < v$ and $u + v + w = 3$.

Choosing the perpendicular component with the largest amplitude is not compulsory. Preferably a component with non-zero amplitude can be chosen but small amplitude can effect sensitivity.

2.1.2.3.5.1.2 Storing the Vortex Data of the Triangle

The data of two components of the corner p of the triangle with indices u and v are simply stored in pu and pv.

$$pu = p_u \qquad\qquad (2.37)$$
$$pv = p_v \qquad\qquad (2.38)$$

The vectorial product of the corner p and scaled unit normal vector is stored as n_p.

$$n_p = n_u \times p_u + n_v \times p_v \; p_w \qquad\qquad (2.39)$$

Instead of storing the dot product, it is possible to stoe the p_w component of p but storing the dot product allows the best memory usage during intersection test phase.

2.1.2.3.5.1.3 Storing the Edge Data of the Triangle

It is necessary to store only two components of each edge with indices u and v (e_{0u}, e_{0v}, e_{1u}, e_{1u}). There is no need to store the component having w index considering an edge is a 3 dimensional vector. The scaled components of e_0 are calculated as in e_1 in the following manner:

$$e_{0u} = (-1)^w e_{0u}/n_w \qquad\qquad (2.40)$$
$$e_{0v} = (-1)^w e_{0v}/n_w \qquad\qquad (2.41)$$
$$e_{1u} = (-1)^w e_{1u}/n_w \qquad\qquad (2.42)$$
$$e_{1v} = (-1)^w e_{1v}/n_w \qquad\qquad (2.43)$$

The w index itself is stored and used for reloading the coordinate components for indexing. The other two indices (u, v) can be reloaded in order to be used for the bias ($u < v$) or ($v < u$) which are used in the pre processing and intersection test phases.

2.1.2.3.5.2 Intersection Algorithm

Generally speaking the ray-triangle intersection problem leads to solving of simple linear system (see Figure 1 for description of vectors):

$$p + u_{e\,0} + v_{e1} = o + dt \qquad\qquad (2.44)$$

if ray hits triangle than ,

$$u + v \leq 1 \qquad\qquad (2.45)$$

$$u, v, t \geq 0 \qquad\qquad (2.46)$$

"The intersection algorithm defined here is based on two methods:

α) Fast hit test based on Plücker coordinates. Using three edges of a triangle, a ray calculation is determined against each edge and whether the ray is clockwise or counterclockwise with respect to the edge is determined. The ray intersects the triangle only when the ray is inside the triangle;

β) Intersection point calculation. If ray passed the hit test (thus it is inside the triangle) then intersection point barycentric coordinates namely u,v and scalar distance *t* (see Figure 15) are calculated." **[11]** This done by solving linear system written in **Eq. 2.44**.

2.1.2.3.5.2.2 Improved Hit Test for Axis Aligned Triangles

Axis aligned triangles have only one non-zero normal's coordinate. In our case this will be n_u and n_v fields equal to zero. Thus, calculations from previous section could be simplified to:

$$\det = d_w \qquad\qquad (2.57)$$

$$\det t = n_p - o_w \qquad\qquad (2.58)$$

$$D_u = d_u \cdot \det t - (p_u - o_u) \cdot \det \qquad\qquad (2.59)$$

$$D_v = d_v \cdot \det t - (p_v - o_v) \cdot \det \qquad\qquad (2.60)$$

$$\det_u = (e_{1v} \cdot D_u - e_{1u} \cdot D_v) \qquad\qquad (2.61)$$

$$\det_v = (e_{0u} \cdot D_v - e_{0v} \cdot D_u) \qquad\qquad (2.62)$$

2.1.2.3.5.2.3 Intersection point calculation

"After it is determined that the ray intersects the triangle, the exact position of intersection point is computed by solving linear system of ray-triangle intersection equations using Kramer's rule." **[11]**

$$rdet = 1/det \qquad\qquad\qquad \textbf{(2.63)}$$

$$t = dett \times rdet \qquad\qquad\qquad \textbf{(2.64)}$$

$$ubar = det_u \times rdet \qquad\qquad\qquad \textbf{(2.65)}$$

$$vbar = det_v \times rdet \qquad\qquad\qquad \textbf{(2.66)}$$

Found *ubar*, *vbar* parameters are baricentric coordinates (see section 1), and *t* - distance of intersection.

2.1.3 Calculation of the Reflected Wave

"Next, the reflected ray is determined by using the rules of Snell's law **[2]**;

1) Reflected ray must lie in the plane of incidence

2) The angle of reflection must be equal to the angle of incidence."
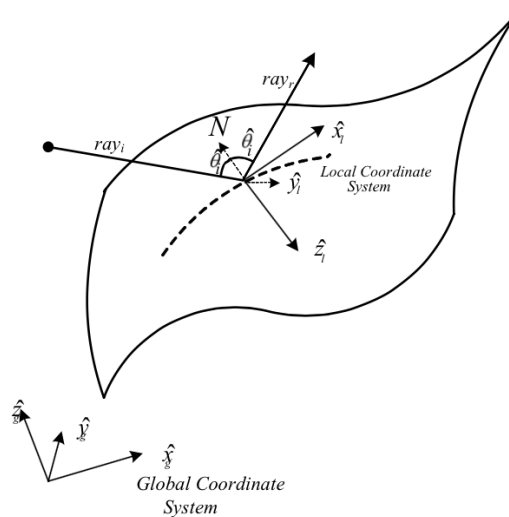
Figure 16 Reflection of a ray

Referring to Figure 16 the reflected ray can be determined according to Snell's law. Let m be a unit vector,

$$\hat{m} = (ray_i \times N)/\sin\theta_i \tag{2.66}$$

where ray_i is the incident ray and N is the reflection normal. Note that m is perpendicular to the plane of incidence. Referring to Figure 14, one can define local coordinates as follows:

$$y_l = \hat{m} \tag{2.67}$$

$$z_l = -N \tag{2.68}$$

$$x_l = -(\hat{m} \times N) \tag{2.69}$$

In spherical coordinates ray_r can be defined as follows

$$ray_r = (r, \theta, \varphi) \tag{2.70}$$

$$r = 1, \ \theta = -(\pi/2 - \theta_i), \ \varphi = 0 \tag{2.71}$$

"Next, (x_l, y_l, z_l) coordinates of ray_r in the local coordinate system can be calculated by spherical to Cartesian coordinate transformation." Finally, local to global coordinate transformation can be performed as follows;

$$A = \begin{bmatrix} 1 & 0 & 0 \\ 0 & 1 & 0 \\ 0 & 0 & 1 \end{bmatrix} \tag{2.72}$$

$$C = \begin{bmatrix} x_l(1) & x_l(2) & x_l(3) \\ y_l(1) & y_l(2) & y_l(3) \\ z_l(1) & z_l(2) & z_l(3) \end{bmatrix} \tag{2.73}$$

$$B = A \cdot C^{-1} \tag{2.74}$$

$$(x_g, y_g, z_g) = B(x_l, y_l, z_l) \tag{2.75}$$

where, B is the transformation matrix. By using the reflected ray as a new incident ray this procedure is applied until the ray ends to bounce in the geometry.

2.1.4 Amplitude Tracing and Calculation of the Scattered Field

In ray paths the field amplitude is also traced. In Geometrical Optics, the amplitude, phase and polarization of electric field can be updated with the following equation.

$$E(x_{i+1}, y_{i+}, z_{i+1}) = (DF)_i \cdot \Gamma_i \cdot E(x_i, y_i, z_i) \cdot e^{-j\varphi} \tag{2.76}$$

Where $\varphi = k_0[(x_{i+1}-x_i)^2+(y_{i+1}-y_i)^2+(z_{i+1}-z_i)^2]^{1/2}$ and *DF* is the divergence factor which calculates the spreading of ray tubes. DF is applicable for curved surfaces and for planar surfaces takes the value of 1. Γ_i is the planar reflection coefficient. For PECs, planar reflection coefficient can be applied with the equation 2.77.

$$\vec{E_r} = (-E_i) + (2(\hat{n} \times \vec{E_i}) \times \hat{n})$$
(2.77)

The scattered far field can be computed by applying the basic physical optics approximation in the aperture where exit rays are gathered. The magnetic current sheet $\vec{M_s}$ over the aperture is;

$$\vec{M_s} = 2\vec{E}(x, y, z) \times \hat{n}_a \tag{2.78}$$

where, $\vec{n}_a$ is aperture normal.

"From this magnetic current sheet, the scattered field can be calculated. The scattered far field is the sum of contributions from individual ray tubes." The contribution of a ray tube is calculated as;

$$\vec{E}^s = \frac{e^{-jk_0 r}}{r} [\hat{\theta}_i A_\theta + \hat{\emptyset}_i A_\emptyset] \tag{2.79}$$

and,

$$\vec{M_s} = [E_{0\theta}\hat{\theta} + E_{0\emptyset}\hat{\emptyset}] \times 2\hat{z} \tag{2.80}$$

where,

$$\hat{\varphi} = \cos\theta\cos\varphi\hat{x} + \cos\theta \sin\varphi\hat{y} - \sin\theta\hat{z} \tag{2.81}$$

$$\hat{\hat{\theta}} = -\sin\varphi\hat{x} + \cos\varphi\hat{y} \tag{2.82}$$

$$\vec{M}_S = 2E_{0\theta}[\sin(\varphi)\hat{y} + \cos(\varphi)\hat{x}] + 2E_{0\varphi}[-\cos(\theta)\cos(\varphi)\hat{y} + \cos(\theta)\hat{y}\sin(\varphi)\hat{x}] \tag{2.83}$$

$$A = \frac{jk_0}{4\pi} \iint M_S \, e^{jkr} dxdy \tag{2.84}$$

$$A_\theta = \frac{jk_0}{2\pi} \iint_{\Sigma_A} dxdy e^{jk_0(ux+uy)} \cdot [E_x\cos\phi_i + E_y\sin\phi_i] \tag{2.85}$$

$$A_\theta = \frac{jk_0}{2\pi} \iint_{\Sigma_A} dxdy e^{jk_0(ux+uy)} \cdot [(-E_x\cos\phi_i + E_y\sin\phi_i)\cos\theta_i] \tag{2.86}$$

$$u = \sin\theta_i\cos\phi_i \tag{2.87}$$

$$v = \sin\theta_i\sin\phi_i \tag{2.88}$$

For the bistatic case, θ^i and φ^i values in equations (2.85), (2.86), (2.87) and (2.88) are replaced with observation angles.

Since the outgoing rays are not uniform, the integrations cannot be evaluated easily [2]. At this point, shooting and bouncing ray method has a way out. A small ray tube is shot into the geometry. The ray tube bounces on the geometry and comes to the aperture finally. Then the scattered field is calculated from this ray tube. Enough ray tubes are shot into the geometry to model the incident plane wave. The total scattered field is the sum of all contributions from the ray tubes.[2]
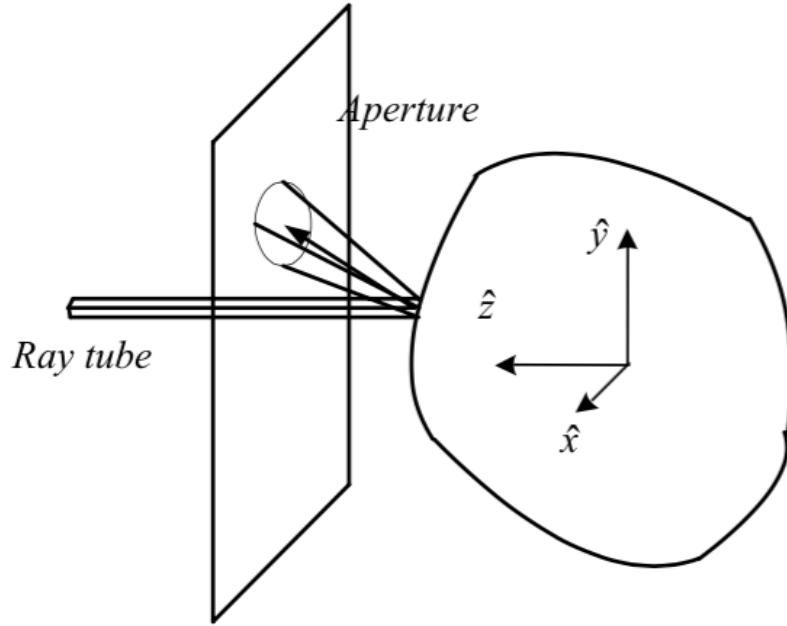
Figure 17 Ray Tube

Assume that the incident ray tube has an area of $(\Delta x_0 \Delta y_0)$. The central ray with direction vector $(s_x,\ sy,\ sz)$ hits the aperture. The ray tube will have an area of $(\Delta x_s \Delta y_s)$ on the aperture and the field within the existing ray tube can be approximated as

$$\begin{bmatrix} E_x(x,y) \\ E_y(x,y) \end{bmatrix} = \begin{bmatrix} E_x(x,y) \\ E_y(x,y) \end{bmatrix} e^{-jk_0\left[s_x(x-x_i)+s_y(y-y_i)\right]} \tag{2.89}$$

This means that the amplitude of the field is same on the ray tube and across the ray tube there is a linear phase variation **[2]**. If the size of existing ray tube is too large, the approximation will not be valid. Components of scattered electric field can be calculated using equations below;

$$A_\theta = \frac{jk_0}{2\pi} \sum_i \iint_{\substack{\text{ray} \\ \text{tube}}} dxdy e^{jk_0(ux+vy)} e^{-jk_0\left[s_x(x-x_i)+s_y(y-y_i)\right]} \\ \cdot \left[E_x(x_i,y_i)\cos\emptyset^i + E_y(x_i,y_i)\sin\emptyset^i\right] \tag{2.90}$$

$$A_\phi = \frac{jk_0}{2\pi} \Sigma_i \frac{\iint_{\substack{ray\\tube}} dxdy e^{jk_0(ux+vy)} e^{-jk_0[s_x(x-x_i)+s_y(y-y_i)]}}{\cdot \left[E_x(x_i,y_i)sin\emptyset^i + E_y(x_i,y_i)cos\emptyset^i)cos\theta^i\right]} \qquad (2.91)$$

Since $E_x(x_i, y_i)$ and $E_y(x_i, y_i)$ are independent of integral variables they can be taken out of the integral;

$$A_\theta = \frac{jk_0}{2\pi} \Sigma_i \left[E_x(x_i,y_i)cos\emptyset^i + E_y(x_i,y_i)sin\emptyset^i\right] \cdot e^{jk_0(s_xx_i+s_yy_i)}(\Delta x_i \Delta y_i)I_i \qquad (2.92)$$

$$A_\phi = \frac{jk_0}{2\pi} \Sigma_i \left[-E_x(x_i,y_i)sin\emptyset^i + E_y(x_i,y_i)cos\theta^i\right] \cdot e^{jk_0(s_xx_i+s_yy_i)}(\Delta x_i \Delta y_i)I_i \qquad (2.93)$$

where

$$I_i = \frac{1}{(\Delta x_i \Delta y_i)} \iint_{\substack{ray\\tube}} dxdy e^{jk_0[(u-s_x)x+(v-s_y)y]} \qquad (2.94)$$

The integral in equation (2.94) is the phase factor in standard physical optics theory [5]. Sometimes it is called shape function and it is the Fourier Transform of the ray tube shape.

In order to take advantage of this method for each ray tube, four rays around a central ray are shot into the geometry.
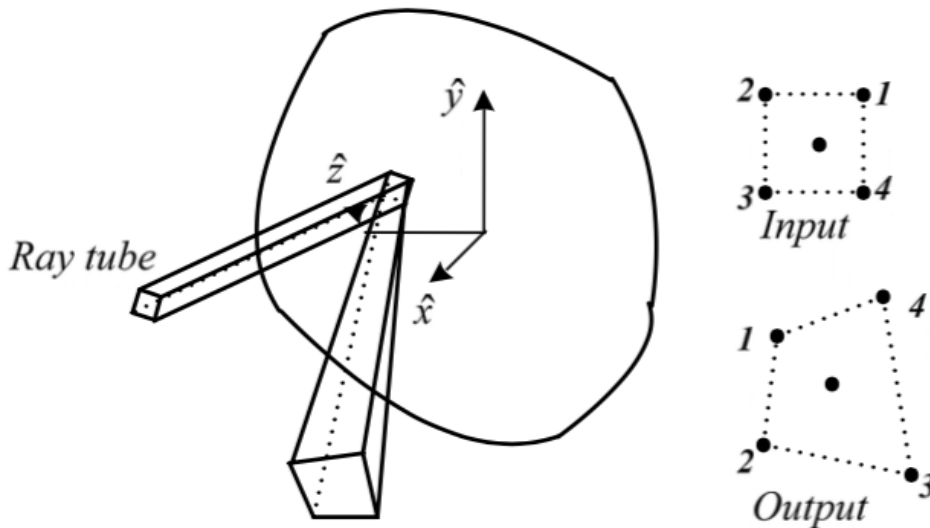
Figure 18 Shape of Exit Ray Tube

"The position vectors of rays are denoted by $\vec{\gamma}_{\hat{n}} = x_n\hat{x} + y_n\hat{y}$, n=1,2,3,4. Fourier transform can be evaluated as described in **[2]** and **[15]**. Simpler proof of this method based on Stokes' theorem can also be considered in **[16]**."

$I_i = S(p,q)/S(0,0)$ **(2.94)**

where,

$$S(p, q) = \sum_{n=1}^{4} e^{jw \cdot \gamma_n} \frac{(x_{n+1}-x_n)(y_n-y_{n-1})-(y_{n+1}-y_n)(x_n-x_{n-1})}{[(x_n-x_{n-1})p+(y_n-y_{n-1})q][(x_{n+1}-x_n)p+(y_{n+1}-y_n)q]}$$ **(2.95)**

$$S(0,0)=(x_1y_2 - x_2y_1)+(x_2y_3 - x_3y_2)+(x_3y_4 - x_4y_3)+(x_4y_1 - x_1y_4)/2$$ **(2.96)**

$$p = k_0 (u - s_x)$$ **(2.97)**

$$q = k_0 (v - s_y)$$ **(2.98)**

$$\vec{w} = p\hat{x} + q\hat{y}$$ **(2.99)**

As a final step, RCS can be calculated as in equations (2.100) and (2.101).

$$RCS_{\theta\theta} = 4\pi \cdot |A_\theta|^2 \quad \text{(Vertical polarization)}$$ **(2.100)**

$$RCS_{\emptyset\emptyset} = 4\pi \cdot |A_\phi|^2 \quad \text{(Horizontal polarization)}$$ **(2.101)**

2.2 Numerical Results

2.2.1 RCS Analysis of Cavity

In this section, RCS analysis of a cavity geometry is performed by SBR method. The SBR algorithm used for these analyses is compiled at MATLAB®. Befor explaining RCS results in detailed, brief information concerning azimuth and elevation angles shall be provided to better understand the results.

2.2.1.1 Definition of Azimuth and elevation Angles

"Azimuth and elevation are angles used to define the apparent position of an object in the sky, relative to a specific observation point. The observer is usually (but not necessarily) located on the earth's surface.

| h = elevation angle, measured up from horizon | z = zenith angle, measured from vertical | A = Azimuth angle, measured clockwise from North |
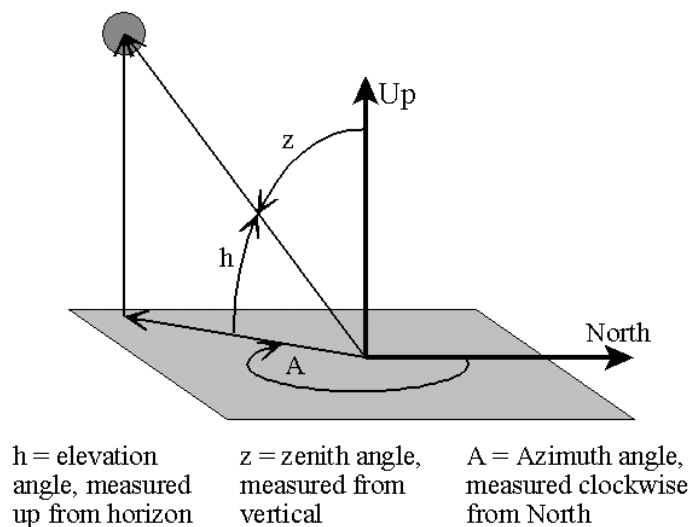
Figure 19 Presentation of azimuth and elevation angles used in the analysis

The azimuth (ϕ) angle is the compass bearing, relative to true (geographic) north, of a point on the horizon directly beneath an observed object. The horizon is defined as a huge, imaginary circle centered on the observer, equidistant from the zenith (point straight overhead) and the nadir (point exactly opposite the zenith). As seen from

above the observer, compass bearings are measured clockwise in degrees from north. Azimuth angles can thus range from 0 degrees (north) through 90 (east), 180 (south), 270 (west), and up to 360 (north again).

The elevation (θ) angle, also called the altitude, of an observed object is determined by first finding the compass bearing on the horizon relative to true north, and then measuring the angle between that point and the object, from the reference frame of the observer. Elevation angles for objects above the horizon range from 0 (on the horizon) up to 90 degrees (at the zenith). Sometimes the range of the elevation coordinate is extended downward from the horizon to -90 degrees. This is useful when the observer is located at some distance above the surface, such as in an aircraft."

In RCS analysis azimuth and elevation angles define incident ray's direction with respect to target's longitudinal and normal axes respectively.

2.2.1.2 Results of RCS Analysis of Cavity

The length of the cavity is 1.8 m and the cross section is a square with dimensions 0.6m×0.6m.
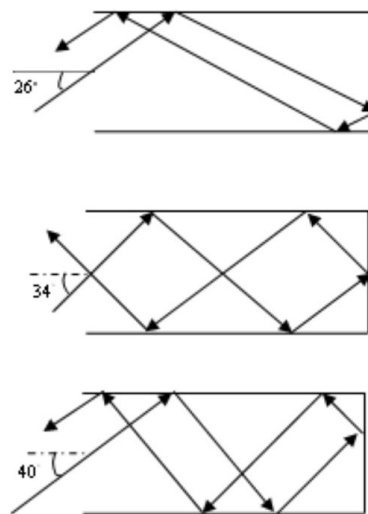
Figure 20 Predicted Ray Path in the Cavity

The incident ray angle ϕ^i is set to zero in order to bound the study in *xz* plane and the excitation is 5 GHz. The estimated propagation directions of the rays incident on the cavity is shown in Figure 20.

RCS values obtained by using the SBR method is plotted in Figures 21 thru 24 are vertical polarization values (RCS$_{\theta\theta}$) and horizontal polarization values (RCS$_{\phi\phi}$). The azimuth angle of the incident ray is assumed to be $\phi = 0$ and the elevation interval is set to [0°-80°] in the analysis as shown in Figure 21. Incidence angles in following results are $\phi = 45°$ (Figure 22), $\phi = 60°$ (Figure 23) and $\phi = 90°$ (Figure 24).
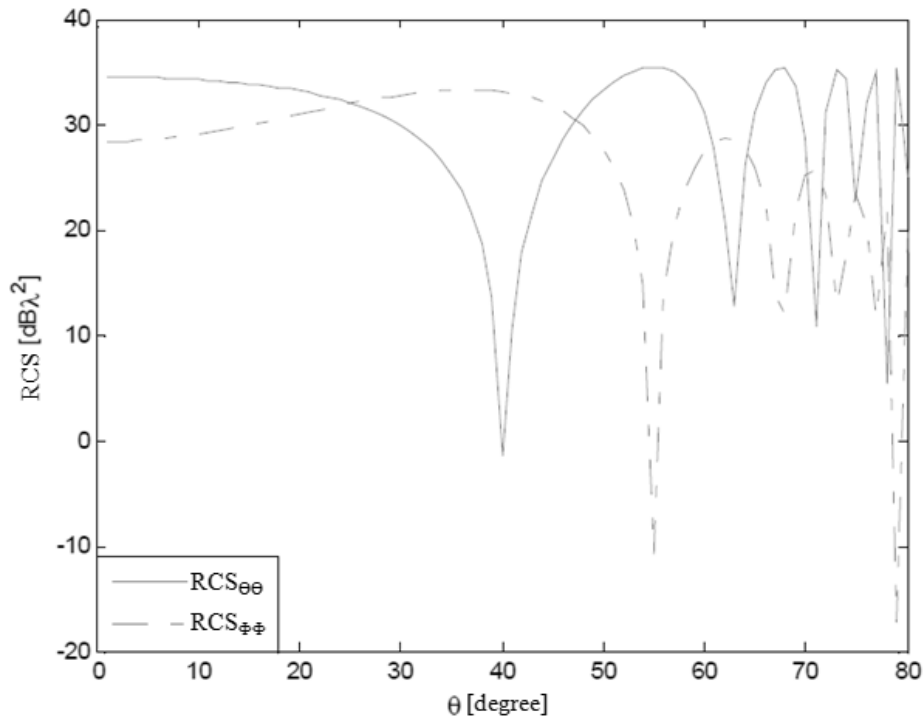
Figure 21 RCS values of a square cross section cavity obtained by SBR method at horizontal and vertical polarizations at φ=0°
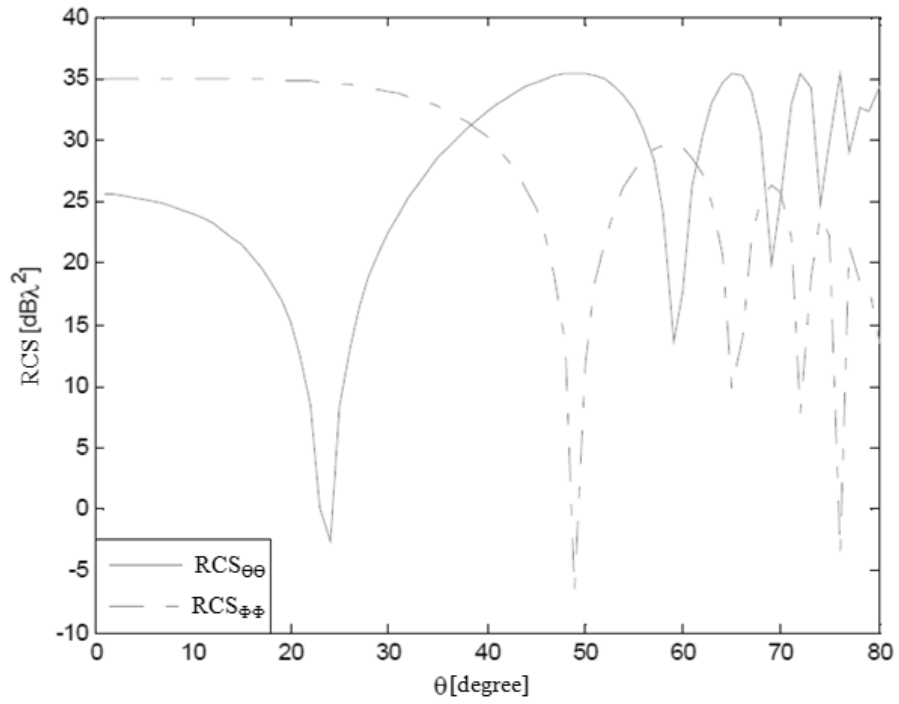
Figure 22 RCS values of a square cross section cavity obtained by SBR method at horizontal and vertical polarizations at φ=45°
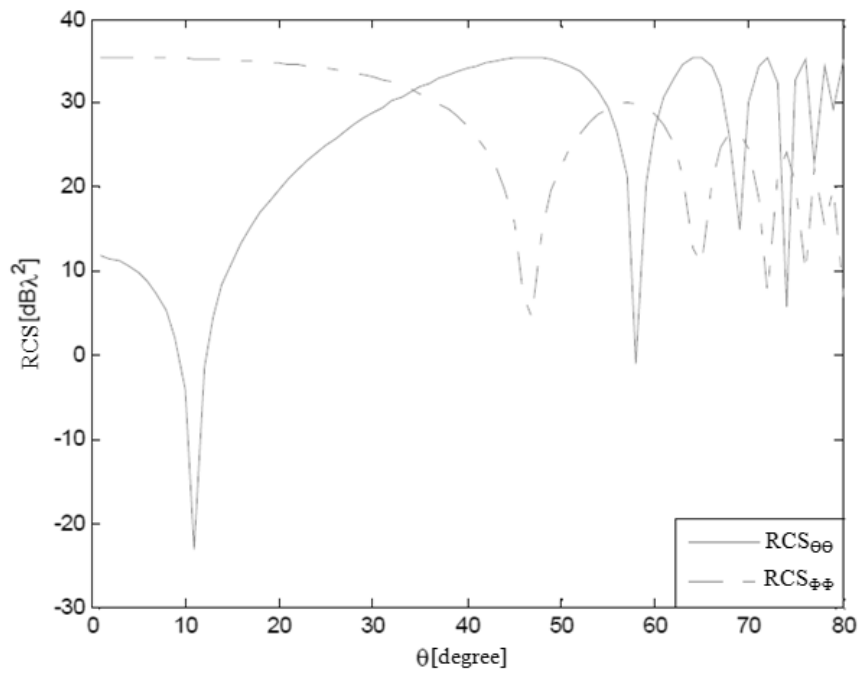
Figure 23 RCS values of a square cross section cavity obtained by SBR method at horizontal and vertical polarizations at φ=60°
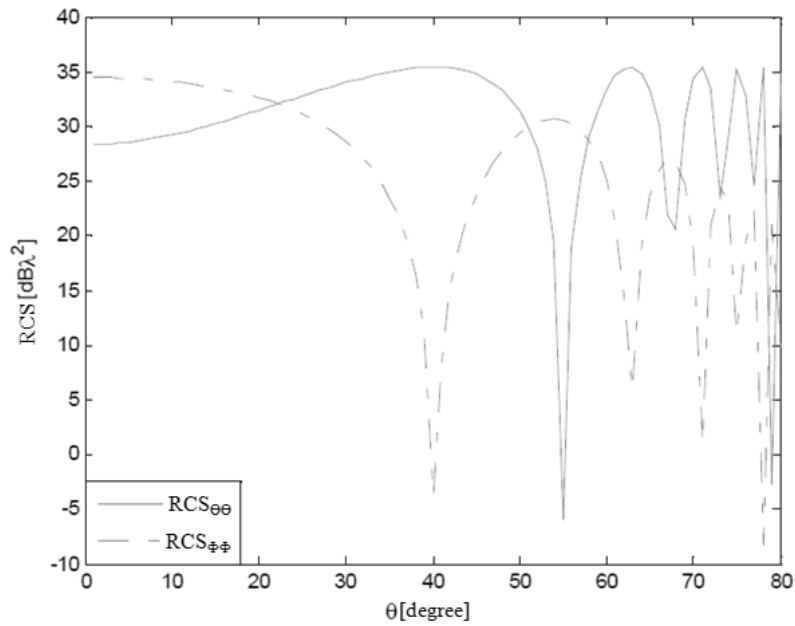
Figure 24 RCS values of a square cross section cavity obtained by SBR method at horizontal and vertical polarizations at φ=90°

As seen from above figures, RCS value is dependent on the incidence angle (φ). RCS value decreases as φ increases at both θθ ve φφ polarizations and there is phase difference at both polarizations.

RCS values obtained by using the SBR method is plotted in Figures 25 thru 27 are vertical polarization values ($RCS_{\theta\theta}$) and horizontal polarization values ($RCS_{\phi\phi}$). The elevation angle interval is set to [0°-80°] in the analysis as shown in following figures. Azimuth angles in following results are $\phi = 45°$ (Figure 24), $\phi = 60°$ (Figure 25). The excitation frequency is 3 GHz.
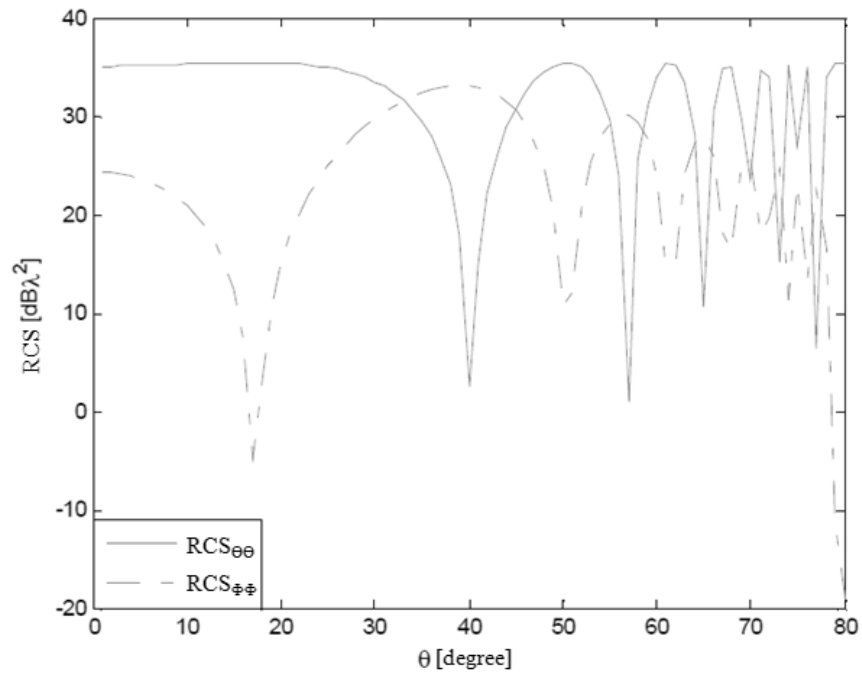
Figure 25 RCS values of a square cross section cavity obtained by SBR method at horizontal and vertical polarizations at φ=0°

.
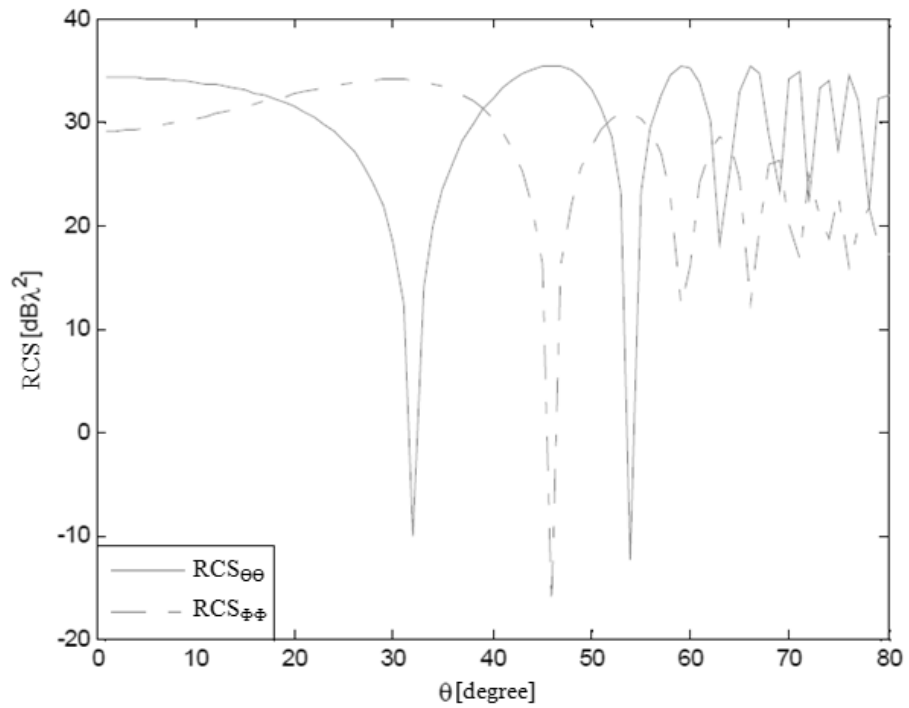
Figure 26 RCS values of a square cross section cavity obtained by SBR method at horizontal and vertical polarizations at φ=45°
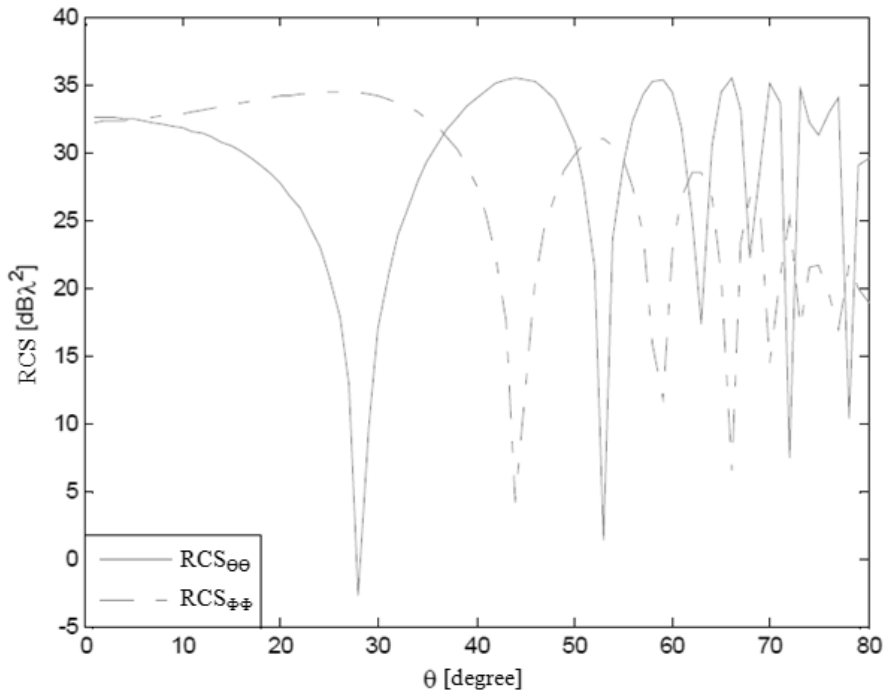
Figure 27 RCS values of a square cross section cavity obtained by SBR method at horizontal and vertical polarizations at φ=60°

As seen from the Figures 25 thru 27, RCS values at θθ polarization have not been changed significantly whereas RCS values at φφ have increased with increasing incidence angle φ*i*. Also, there is phase difference at both polarizations.

RCS values at 1 GHz and 10 GHz frequency values, [0°-80°] elevation interval and φi=0° are presented in Figures 28 and 29.
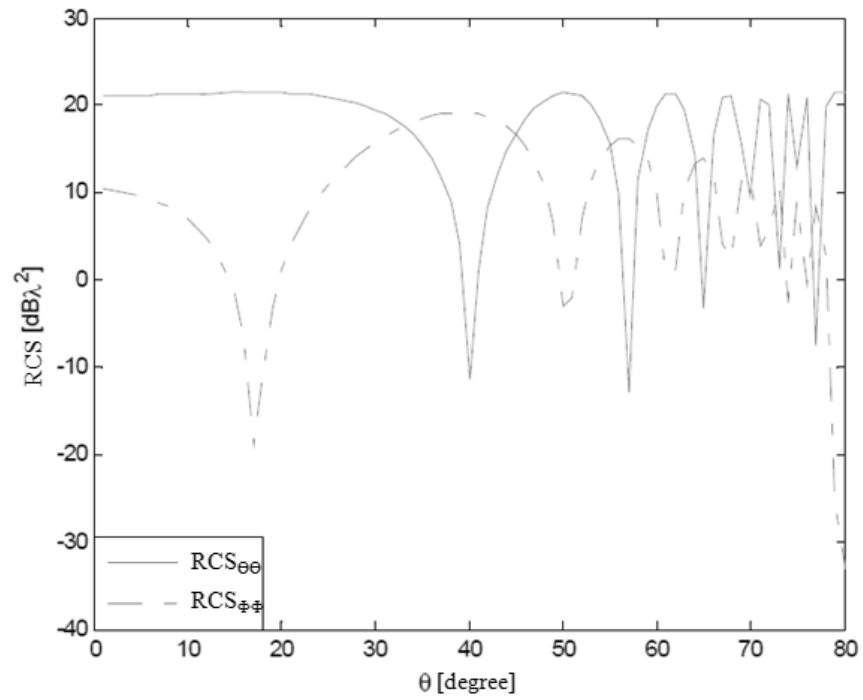
Figure 28 RCS results at 1 GHZ obtained by SBR method
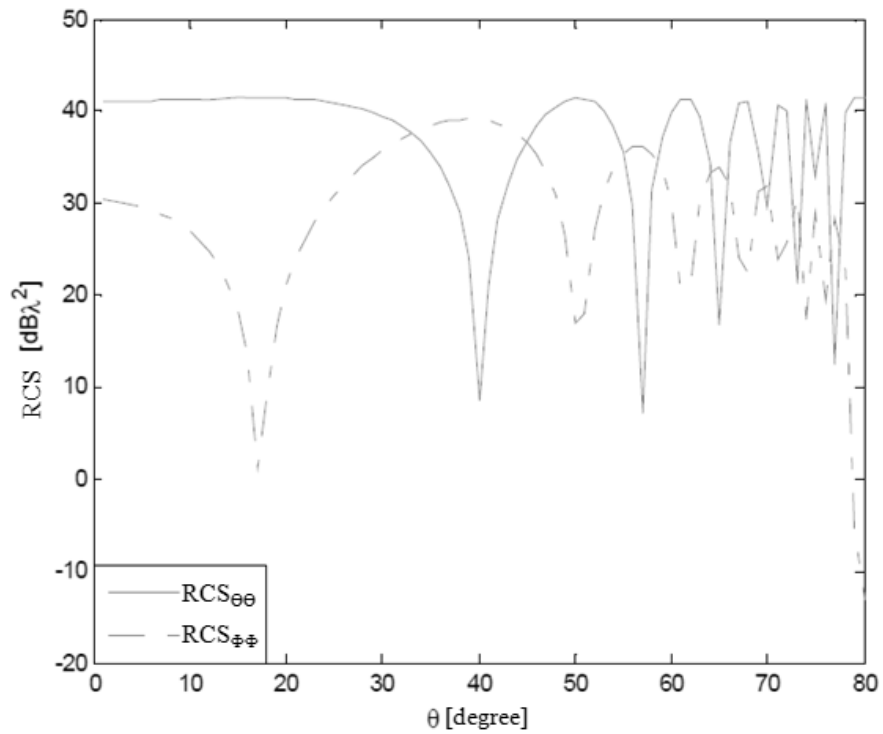
Figure 29 RCS results at 10 GHZ obtained by SBR method

45

As seen from Figures 28 and 29 it can be concluded that there is an average difference of 20 dB's between RCS amplitudes calculated at 1 GHz and 10 GHz. According to results of analysis conducted at 1 GHz results maximum value of RCS is 20 dB at horizontal and 10 dB at vertical polarization. On the other hand Results obtained from 10 GHz analysis show that maximum value of RCS is 40 dB at horizontal polarization and 30 dB at vertical polarization.

2.2.2 Numerical Results for Simple Targets

SBR algorithm computing the RCS of basic and complex shapes is compiled by MATLAB. The code has the ability to read geometries produced in *.stl* format. STL format transforms surface geometries into discrete geometries made of flat triangles.

The code can calculate the RCS of any shape discretized into triangular panels. Target geometries are modeled by triangular plates and scattering field integral is calculated by PO as explained in SBR method. The scattering field from each triangular element is superposed in a simple and fast manner. Therefore computation time is independent from size of the plates.

In this section, RCS values calculated by SBR method for some simple shapes have been presented. RCS values of simple shapes such as square plate, plate with a hole, cube, corner reflector and cylinder are presented at different frequencies, aspect angles and polarizations. Numerical values obtained by SBR is compared by PO method.

Various mesh models of a 1m x 1m square plate is presented in Figure 28. Triangular mesh models of the square plate composed of 2, 4 and 232 triangles are presented in Figures 30 (a), (b) and (c) respectively.

<center>(a)   (b)   (c)</center>
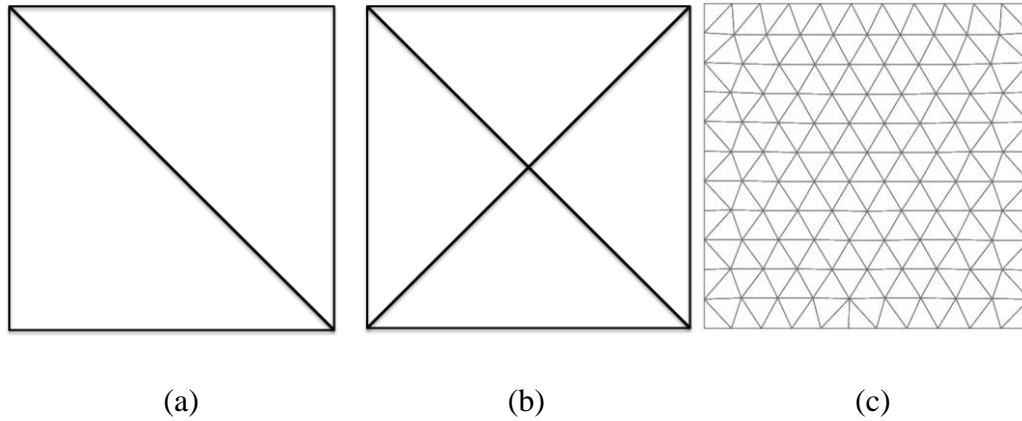
Figure 30 (a) Square plate modeled by two triangular elements**, (b)** Square plate modeled by four triangular elements, **(c)** Square plate modeled by 232 triangular elements

Since a triangle has 3 sides, ray-triangle intersection test can be performed by checking the location of a certain ray with respect to only 3 sides. Quadrilateral (quad) elements (elements with 4 sides) could also be used in the analysis. However since a quad element has 4 sides, ray-quad intersection test would take longer computation times but the results would not improve much as the accuracy of RCS analysis results inrease with number of rays shot into the geometry.

Physical Optics (PO) method cannot calculate the multiple scatter effects. However in SBR method, shadowing effects and multiple reflections can be taken into consideration. The ray window illuminating the target is composed of different number of rays at different frequencies. As the frequency changes, computation time as well as the number of rays change.
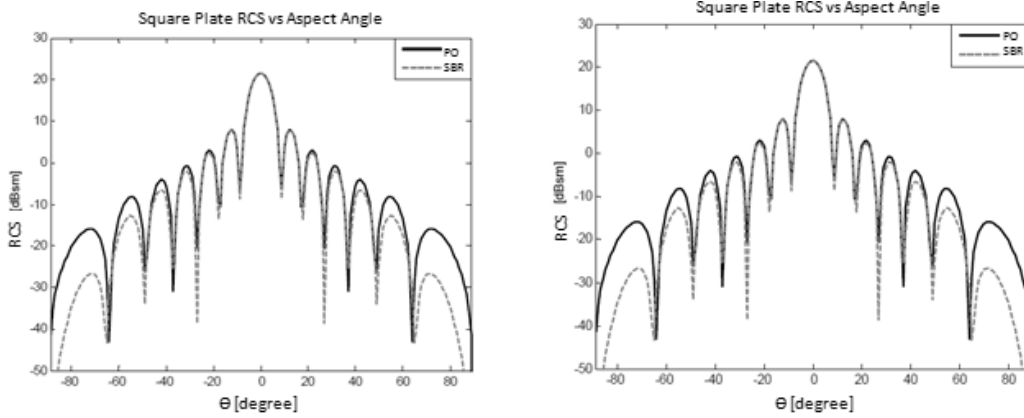
Figure 31 RCS of square plate vs aspect angle with PO and SBR methods **(a)** Vertical polarization, **(b)** Horizontal polarizationf

RCS values of the square plate in Figure 31 (a) illuminated at φ=0° and [-90°,90°] θ interval and 1 GHz frequency at vertical polarization (a) and horizontal polarization (b) with both SBR and PO methods are given in Figure 31. RCS value is given in terms of dBsm. In SBR method, rays are shot into the geometry with spacings of λ/20 which results in 4356 rays at 1 GHz. Intersection test of these rays with the triangles are also performed. RCS of square plate reaches the maximum value at θ=0°. SBR and PO techniques result in similar results at 4 consecutive peaks from θ=0°.

RCS of square plates in Figure 30 (b) and Figure 30 (c) at 1 GHz frequency, φ=0° and θ interval of [-90°,90°] are given in Figures 32 and 33 respectively.
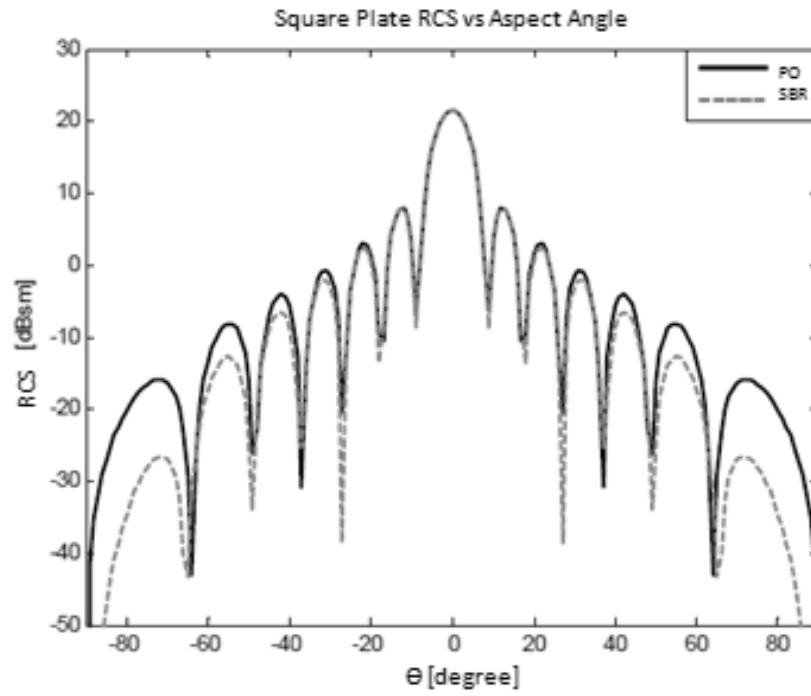
Figure 32 RCS of square plate vs aspect angle with PO and SBR methods at Vertical polarization
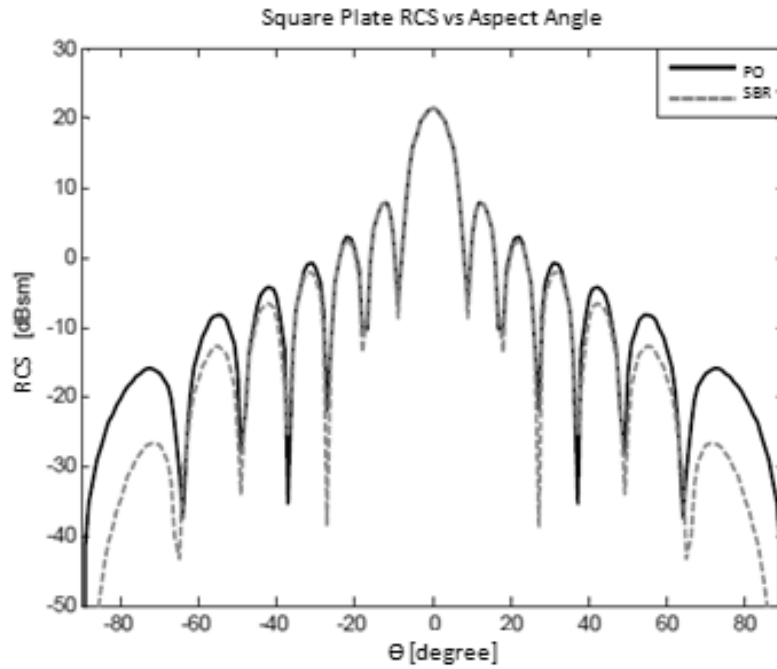
Figure 33 RCS of square plate vs aspect angle with PO and SBR methods at Vertical polarization

Figures 32 and 33 show that RCS values obtained from squares plates of Figure 30 (b) and (c) are almost identical to those presented in Figure 31. Therefore it can be concluded that for a flat square plate RCS is independent of the size of the triangular elements. Provided that the target surface is flat, surface properties like unit normal vector and surface impedance are constant, the surface can be partitioned by using larger elements since even relatively larger elements can represent flat surfaces perfectly. Therefore number of elements necessary to represent a flat surface is relatively small. Providing that the target surface is curved, number of flat elements needed to represent the surface perfectly is relatively large. In othe words element sizes decrease dramatically. Table 2 shows the increase in computation time as the number of triangular elements increases.

Table 2 Computation time vs number of elements on the target surface [sec]

Number of triangular plates	2	4	232	600	800	1000	1250	1700	2200
Badouel Method	34	37	600	800	1200	1550	2000	2800	3800
Moller-Trumbore Method	30	35	280	650	820	1000	1500	2000	2550
Plucker Method	32	34	210	450	600	790	1100	1500	2200

Table 2 shows the computation time necessary for intersection tests during RCS analysis of flat square plate. It can be concluded that Plucker test is almost twice as faster as Badouel test.
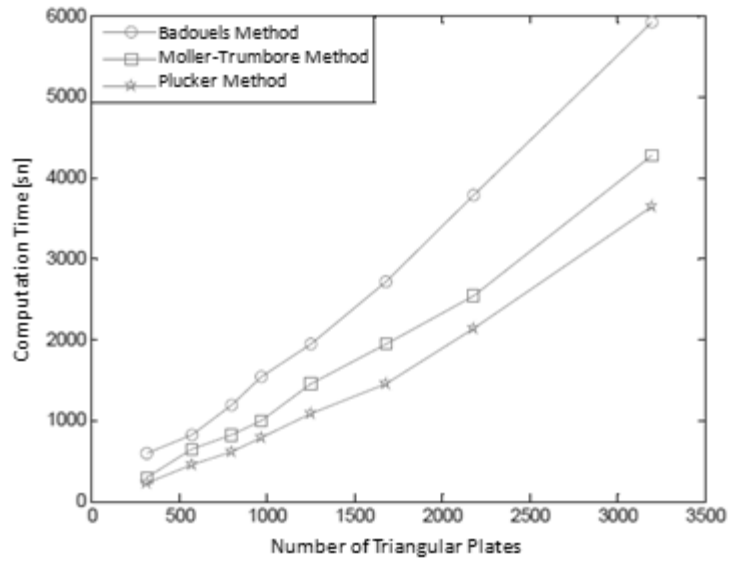
Figure 34 Change in time of computation in SBR method when Badouel, Moller-Trumbore and Plucker methods are used

Figure 34 shows the variation in time of computation in SBR method when Badouel, Moller-Trumbore and Plucker methods are used for ray-triangle intersection test. Plucker method provides much faster computation compared to other methods.

Figure 35 shows monostatic RCS values of the square plate presented in Figure 30 (b) at 4 GHz, $\varphi=0°$ and vertical polarization.
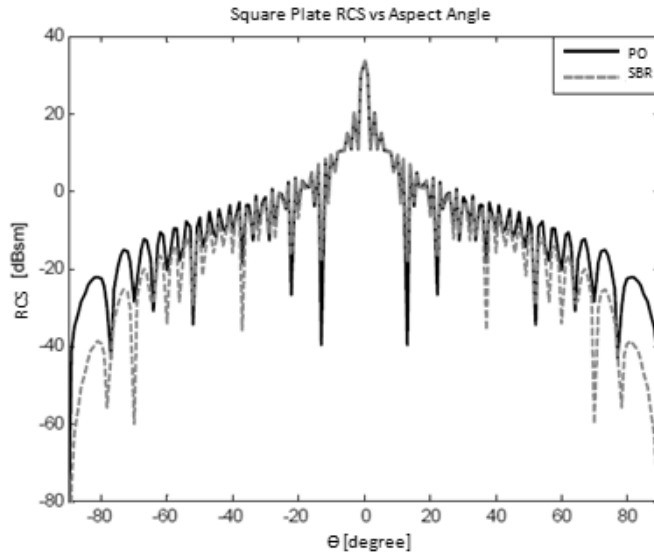
Figure 35 RCS of square plate vs aspect angle with PO and SBR methods at Vertical polarization

Compared to Figure 33, in Figure 35 both number of peaks and the amplitude of RCS has increased. While at 1 GHz RCS value is 22 dB, at 4 GHz it is 34 dB at $\varphi=0°$.

Figure 36 shows monostatic RCS values of the square plate at 1 GHz, $\varphi=30°$ and vertical polarization.
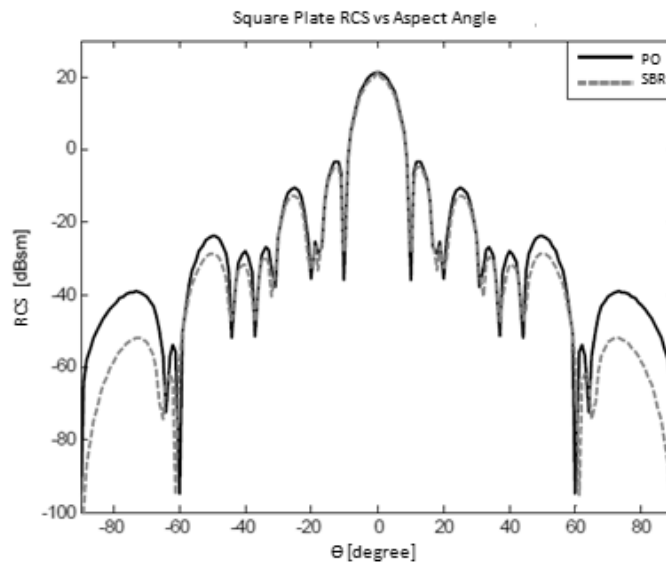
Figure 36 RCS of square plate vs aspect angle with PO and SBR methods at Vertical polarization and $\varphi=30°$

52

When the results presented in Figure 36 compared to those in Figure 32, it can be concluded that the peak value at φ=0° is the same. The RCS value changes with the aspect angle.

Figure 37 shows monostatic RCS values of the square plate at 1 GHz, φ=45° and vertical polarization. 1090 rays are shot to the meshed square plate with a spacing value of λ /10.
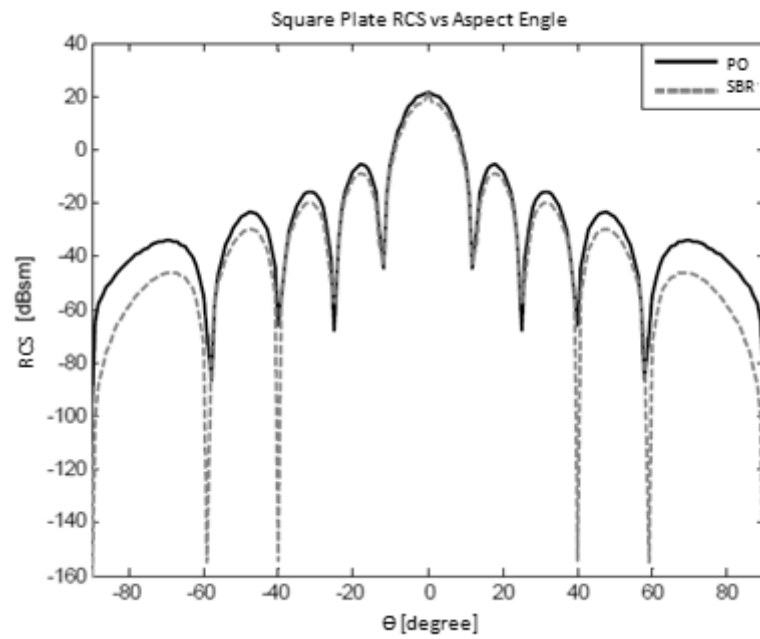
Figure 37 RCS of square plate vs aspect angle with PO and SBR methods at Vertical polarization and φ=45°
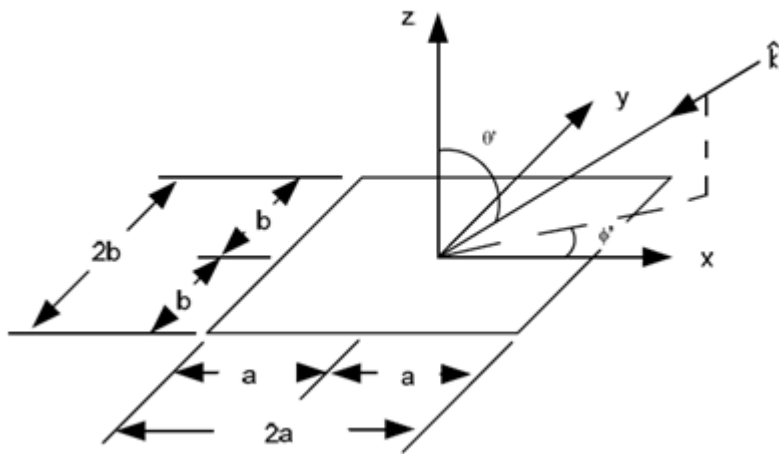
Figure 38 A square plate mounted on xy plane

In addition to the results presented above, monostatic RCS of a square plate mounted on *xy* plane (Fig. 38) has been investigated at 2-18 frequency interval, vertical polarization and $\theta=0^o$, $\varphi=0^o$.
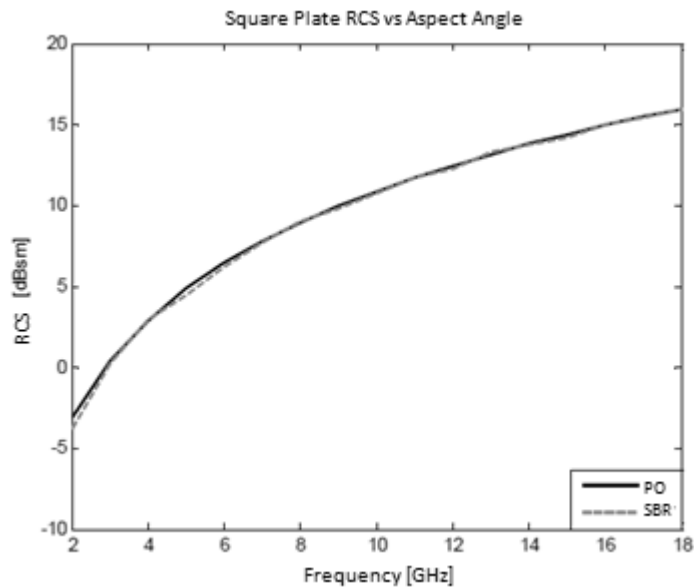
Figure 39 RCS of square plate vs frequency with PO and SBR methods at Vertical polarization

As shown in Figure 39, RCS results obtained by SBR perfectly matches PO results. Monostatic RCS results at vertical polarization, $\varphi=0°$ and θ interval [-90°,90°] frequency values 5 and 12 GHz are given in Figures 40 and 41. Ray windows

illuminating the target are formed with λ /20 spacing and number of rays at 5 and 12 GHz are given in Table 3.

Table 3 Number rays with respect to frequency

Frequency [GHz]	Number of Rays
5	3250
12	18750
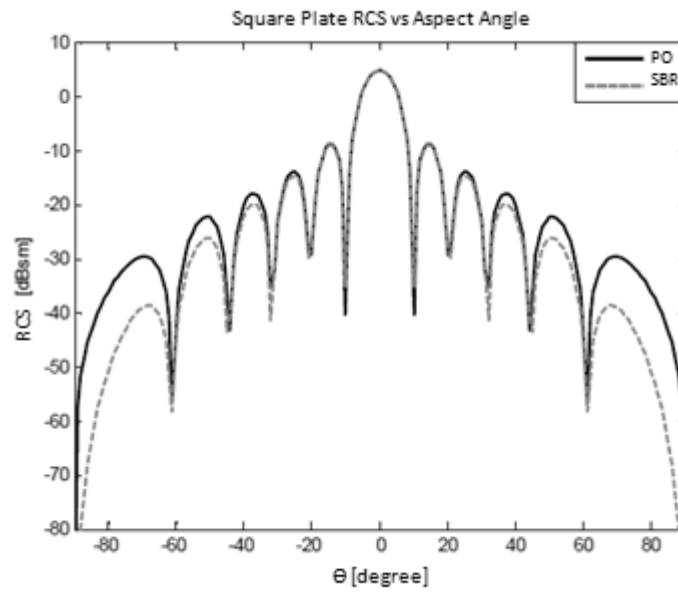
Figure 40 RCS of square plate vs frequency with PO and SBR methods at Vertical polarization and 5 GHz
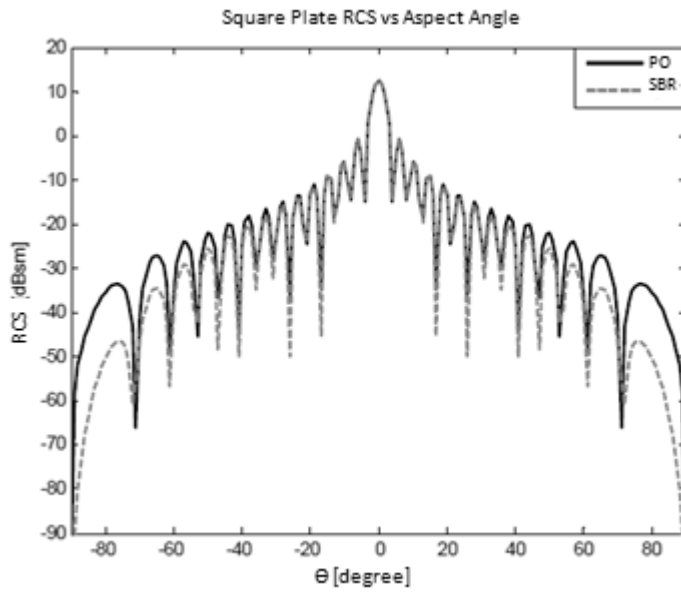
Figure 41 RCS of square plate vs frequency with PO and SBR methods at Vertical polarization and 12 GHz

As seen in figures 40 and 41 as the frequency increases more peaks occur and the peak value at $\theta = 0°$ increases.
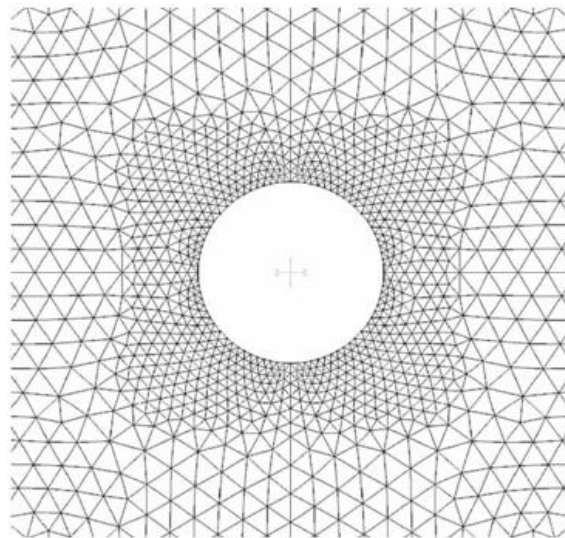
Figure 42 Discretized geometry of the square plate with a hole at the center

Monostatic RCS of a square mounted on *xy* plane with a hole at the center and edge length of 5m at 500 MHz, φ=0° at vertical polarization is given in Figure 42. The square plate with the hole consist of 950 of triangular elements. The ray window for this case consist of 27500 rays at a spacing value of λ/10.
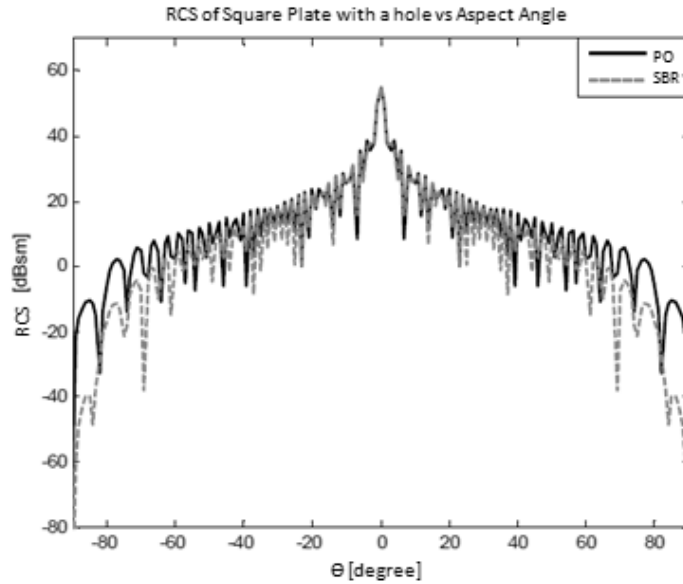
Figure 43 RCS of square plate vs aspect angle with PO and SBR methods at vertical polarization and 500 MHz frequency

In Figure 43, RCS value of square plate vs aspect angle is given with PO and SBR methods at Vertical polarization and 500 MHz frequency. The results obtained by PO and SBR methods perfectly match ing the [-40°,40°] interval.

In Figure 44 a cube with edge length of 1 m and consisting of 12 triangular elements is shown. Ray window illuminating the cube consist of 4400 rays at a frequency of 1 GHz at a spacing of λ/10.
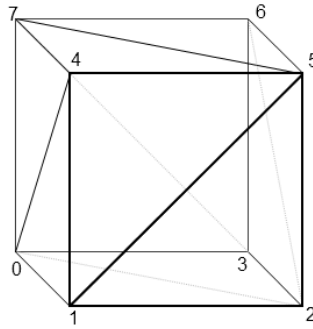
Figure 44 Cube geometry discretized into triangles

Figure 44 shows monostatic RCS results of the cube geometry at a frequency value of 1 GHz, azimuth angle of φ=0° and a θ angular interval of [-90°,90°] at vertical polarization. Results obtained by SBR and PO methods are compared.
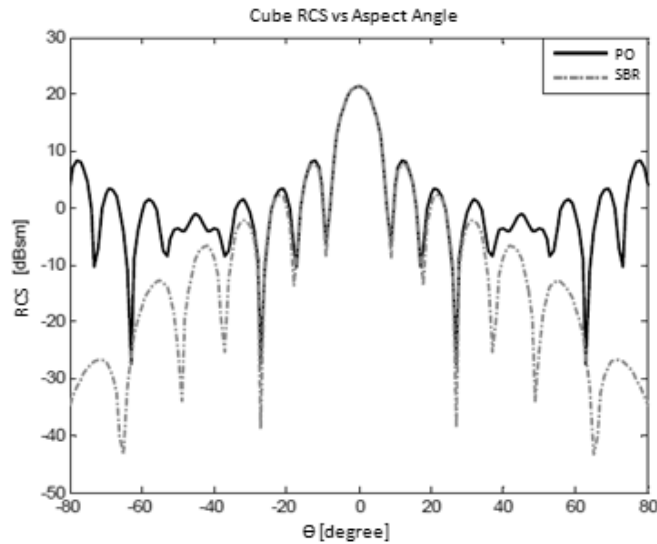
Figure 45 RCS of cube vs aspect angle with PO and SBR methods at vertical polarization and 1 GHz frequency

As seen from the above figure the results obtained from SBR and PO match perfectly inside the θ angular interval of [-25°,25°] where specular turns from the target are dominant.

Figure 46 shows monostatic RCS results of the cube geometry at a frequency value of 1 GHz, azimuth angle of φ=25° and a θ angular interval of [-90°,90°] at vertical polarization. Results obtained by SBR and PO methods are compared.
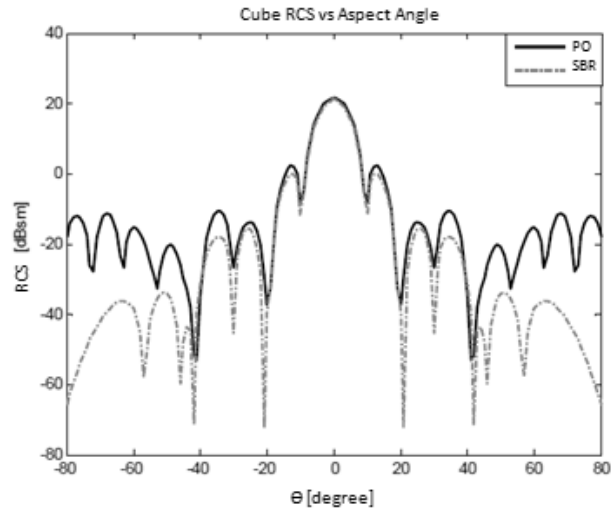
Figure 46 RCS of cube vs aspect angle with PO and SBR methods at vertical polarization φ=25° and 1 GHz frequency

The results provided in Figure 46 when compared with the results in Figure 43 shows that the peak value at θ=0° does not change, however the whole envelope of the graph has changed. Also, SBR and PO match perfectly inside the θ angular interval of [-30°,30°] where specular turns from the target are dominant.

Figure 47 shows monostatic RCS results of the cube geometry at a frequency value of 5 GHz, azimuth angle of φ=0° and a θ angular interval of [-80°,80°] at vertical polarization. Results obtained by SBR and PO methods are compared.
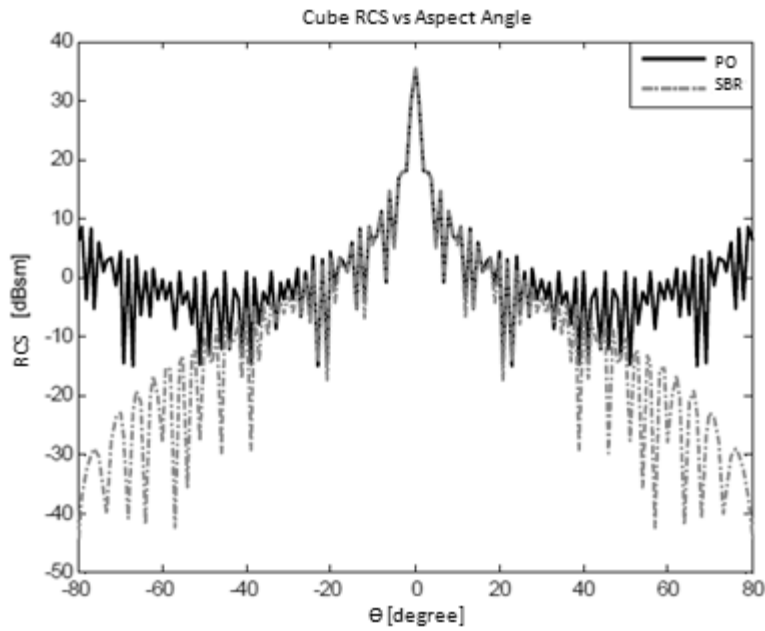
Figure 47 RCS of the cube vs aspect angle with PO and SBR methods at vertical polarization φ=0° and 5 GHz frequency

The results provided in Figure 47 shows that SBR and PO methods match perfectly inside the θ angular interval of [-30°,30°] where specular turns from the target are dominant.
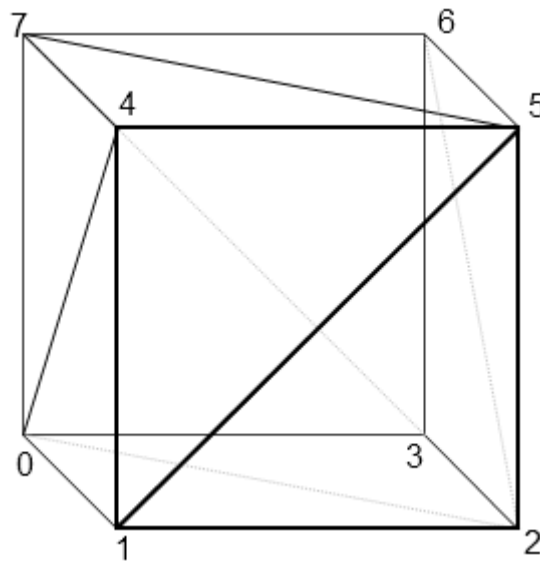
Figure 48 Cube geometry discretized into triangles

Figure 48 shows a cube with dimensions x=7 m, y=7 m and z=7 m. The surface of the cube is composed of 24 triangular elements. Monostatic RCS of the cube has been investigated at vertical polarization, φ=0° and an angular interval of [0°,180°] for θ. The analysis has been conducted at 2 GHz frequency where 218000 rays have been shot into the target with standard spacings of λ /10.
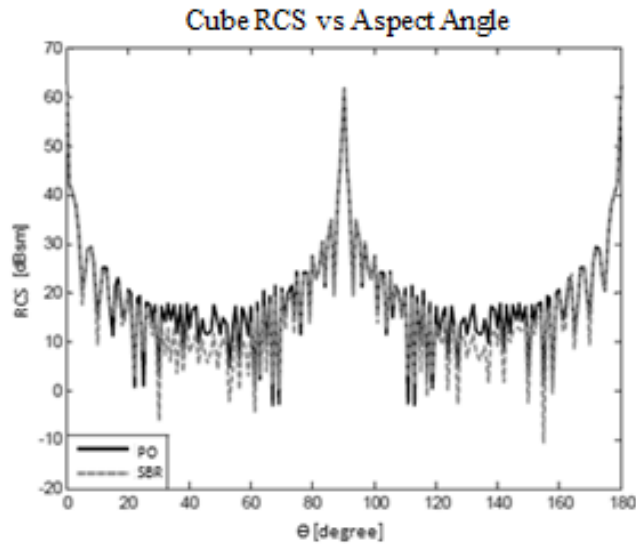
Figure 49 RCS of the cube vs aspect angle with PO and SBR methods at vertical polarization φ=0° and 2 GHz frequency

Figure 49 shows that inside elevation angle intervals of [30°-60°] and [120°-150°] results obtained from SBR and PO methods do not match due to edge and corner effects. Except these boundaries, SBR and PO results match in regions where specular surface returns are dominant.

Table 4 Computation time for RCS analysis of the cube

Intersection test method	Number of Triangular Plates	Computation Time [sec]
Badouel	36	750
Moller-Trumbore	36	510
Plucker	36	450

Table 4 shows computation times for analysis when Badouel, Moller-Trumbore and Plucker test methods are used for ray-triangle intersection test. As seen from the

table, Plucker test method provides 40% less computation time compared to Badouel test.

Figure 50 shows monostatic RCS results of the cube geometry at a frequency value of 6 GHz, azimuth angle of φ =90° and an elevation angular interval of [0°,360°] The analysis have been conducted at vertical polarization with angular increments of 1°. Results obtained by SBR and PO methods are compared.
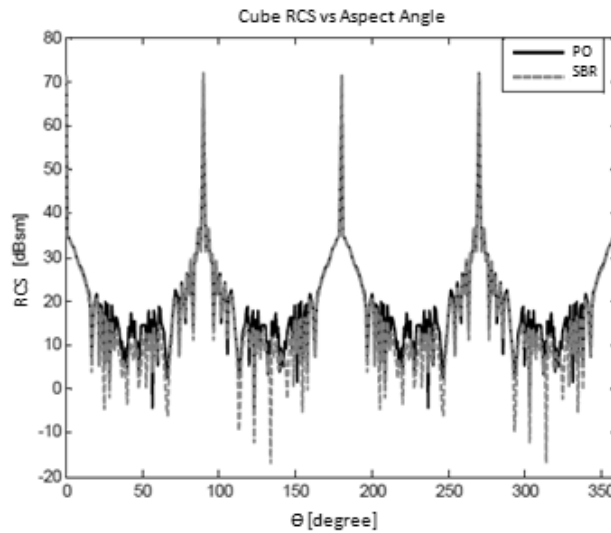
Figure 50 RCS of the cube vs aspect angle with PO and SBR methods at vertical
polarization φ =90° and 6 GHz frequency

Figure 50 shows that inside elevation angle intervals of [30°-60°], [120°-150°] [300°-330°], [210°-210°] results obtained from SBR and PO methods do not match due to edge and corner effects. Except these intervals, SBR and PO results match in regions where specular turns are dominant.

Moreover RCS analysis of the box has been been conducted at azimuth angle φ =0° and elevation angle θ=0° and [2-18] GHz frequency interval. The results have been plotted in Figure 49.
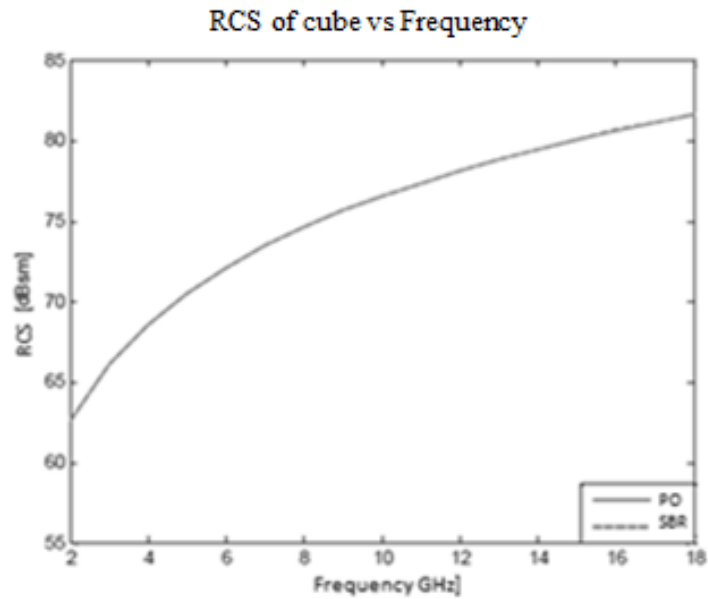
Figure 51 RCS of box vs frequency with PO and SBR methods at vertical polarization, φ =0° and θ=0°

Figure 51 shows that results obtained by PO and SBR perfectly match. Also RCS increases as frequency increases. As the frequency is increased, the wavelength gets smaller compared to the cube size. Since the electric field integral depends on wavelength, RCS of the single cube increases.
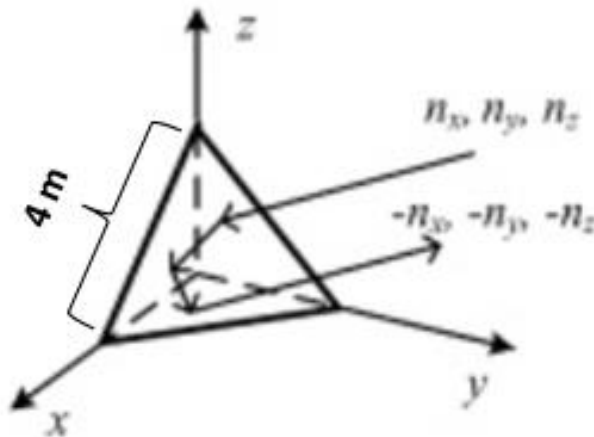
Figure 52 Geometry and dimensions of the corner refelctor

Geometry of a corner reflector is shown in Figure 52.The straight edges of the corner reflector are equal to 4m. The corner reflector consists of 3 triangular plates in total. RCS analysis has been conducted at azimuth angle φ=0° and elevation angle θ=[0°,

63

180°] with angular increments of 1° at vertical polarization. Number of rays illuminating the target at 2, 5 and 8 GHz frequencies with standard spacings of $\lambda/10$ are given in Table 5.

Table 5 Number rays vs frequency for the corner reflector case

Frequency [GHz]	Number of Rays
2	177000
5	1102200
8	1587000
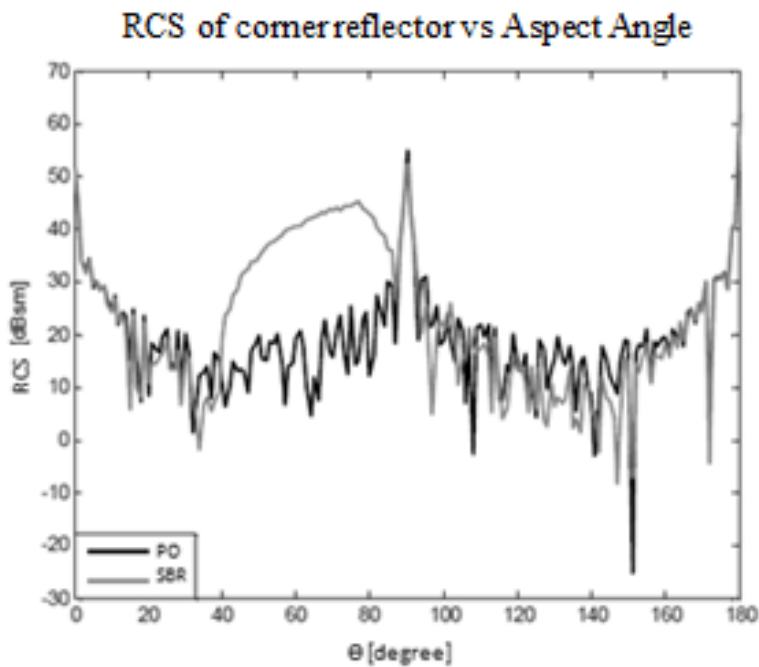
Figure 53 RCS of corner reflector vs aspect angle with PO and SBR methods at vertical polarization, 2 GHz

Figure 53 shows that inside elevation angle intervals of [40°-85°], results obtained from SBR and PO methods do not match due to multiple reflection effects between perpendicular surfaces of the corner reflector. Except these intervals, SBR and PO results match in regions where specular surface return effects are dominant.

Table 6 Computation time for RCS analysis of two boxes

Ray-triangle intersection test method	Number of Triangular Plates	Computation time [sec]
Badouel	73	1340
Moller-Trumbore	73	1060
Plucker	73	1000

Table 6 shows Plucker test method provides 25% reduction in computation time. Campared with the results of single box, one can conclude that Plucker test is the fast intersection test but does not always yields to same amount of acceleration compared to other tests. Plucker test causes an acceleration of 40% for single box case while producing 25% acceleration for the case of corner reflector. These results show that speed of Plucker test depends on many paramaters such as size and geometry of the target, size of elements forming the target, frequency that the analysis has been conducted etc. Scattering mechanisms triggered by multiple or single reflections can also effect the speed of Plucker test. In the case of corner reflector multiple reflection can ocur whereas in a single cube only single reflections can ocur.
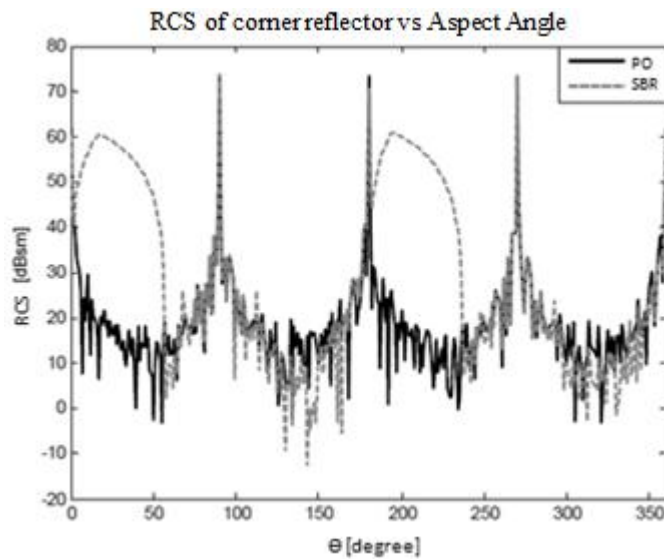
Figure 54 Monostatic RCS of corner reflector vs aspect angle with PO and SBR methods at vertical polarization, 8 GHz

Figure 54 shows inside elevation angle intervals of [5°-55°] and [190°-240°] results obtained from SBR and PO methods do not match due to multiple reflection effects

between the reflecting surfaces. Except these boundaries, SBR and PO results match in regions where specular turns are dominant.

In Figure 55 corner reflector is illuminated at $\varphi=0^o$ and $\theta=0^o$ and monostatic RCS values in frequency interval of [2-18] GHz is plotted.
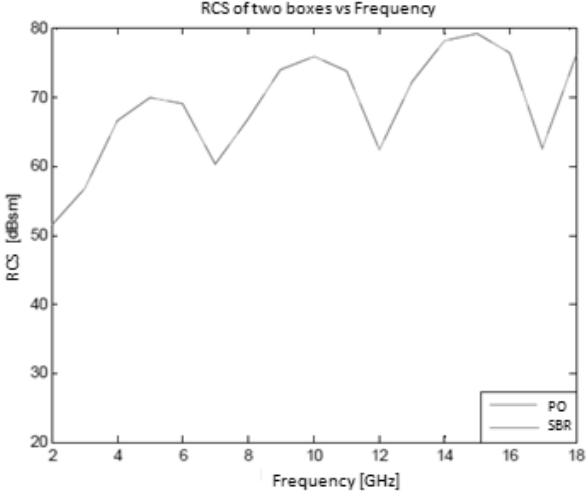
Figure 55 Monostatic RCS of the corner reflector vs frequency with PO and SBR methods at vertical polarization, $\varphi=0^o$ and $\theta=0^o$

Figure 55 shows that results obtained by PO and SBR perfectly match. Also RCS increases as frequency increases. As the frequency is increased, the wavelength gets smaller compared to the target size. Since the electric field integral depends on wavelength, RCS of the target increases.
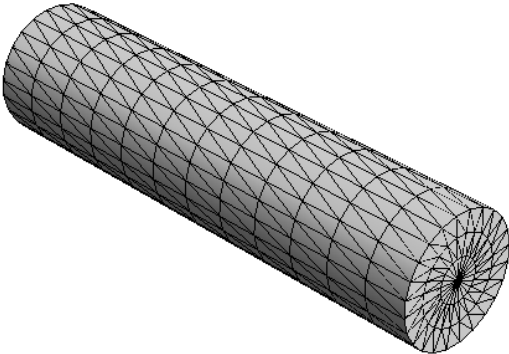
Figure 56 Meshed model of cylinder

Meshed model of cylinder consisting of 400 triangular elements is shown in Figure 56. The cylinder has a diameter of 3m and height of 10 m. Number of rays

66

illuminating the target at 1, 5 and 12 GHz frequencies with standard spacings of $\lambda/20$ are given in Table 2-7.

Table 7 Number rays vs frequency for cylinder case

Frequency [GHz]	Number of Rays
1	4350
5	70750
12	120500

Monostatic RCS values of cylinder geometry are presented at 1, 5 and 12 GHz in Figures 57, 58, and 59 respectively. RCS analyses have been conducted at azimuth angle $\varphi=0^o$ and elevation angle $\theta=[90°, 90°]$ with angular increments of 1° at vertical polarization using both SBR and PO methods.
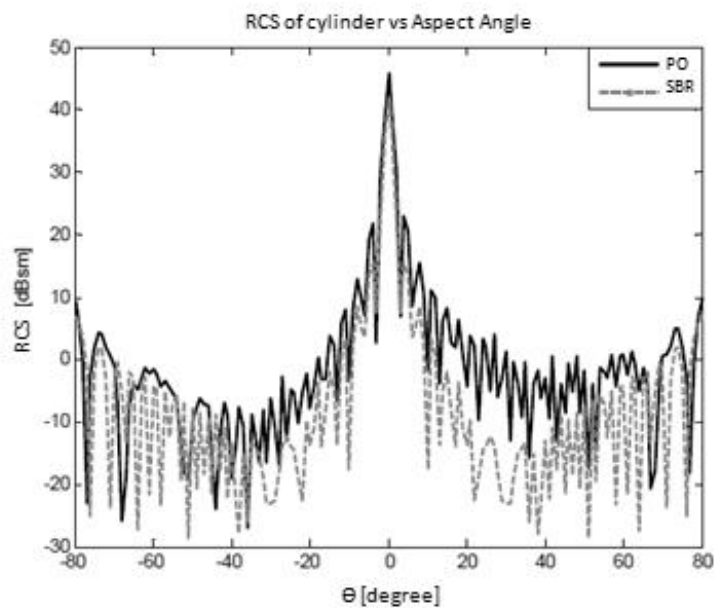
Figure 57 Monostatic RCS of cylinder vs elevation angle with PO and SBR methods at vertical polarization, 1 GHz

Figure 57 shows inside elevation angle intervals of [-35°,-15°] and [10°,65°] results obtained from SBR and PO methods do not match due to edge and corner effects. Except these boundaries, SBR and PO results match in regions where specular

surface returns are dominant. It is also observed that the RCS of the cylinder reaches maximum at θ=0°
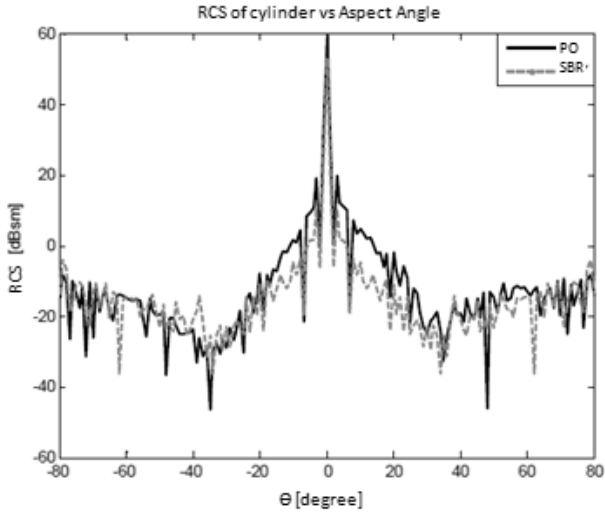
Figure 58 Monostatic RCS of cylinder vs elevation angle with PO and SBR methods at vertical polarization, 5 GHz

Figures 58 and 59 show that inside elevation angle intervals of [-20°,-80°] and [20°,80°]; [-15°,-80°] and [15°,80°] respectively, results obtained from SBR and PO methods do not match due to edge diffractions. Except these intervals, SBR and PO results match in regions where specular turns are dominant.
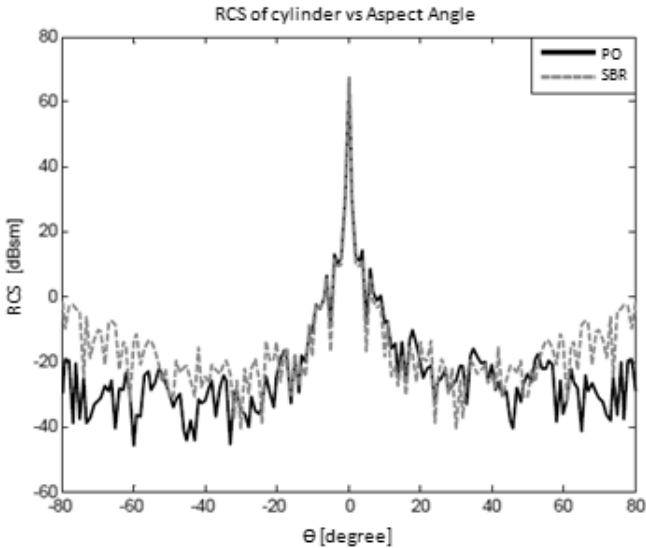
Figure 59 Monostatic RCS of cylinder vs elevation angle with PO and SBR methods at vertical polarization, 12 GHz

CHAPTER 3

APPLICATION OF SBR TO COMPLEX TARGETS

In the previous chapter, the SBR code is tested by using simple PEC objects. However, realistic targets possess much more complex geometries with several scattering mechanisms. The interactions between parts of complex geometries will affect dramatically the RCS values. At this point the SBR code, with its multiple scattering capability, will be superior to other ray based RCS prediction tools. The RCS prediction code developed in the previous chapter will be applied to complex targets in this chapter, in order to evaluate the performance of the method for realistic cases.

In the simulations, targets are modeled using large triangular patches. In order to calculate the monostatic RCS of a target from different aspect angles, two different methods are used. In the first method, the target kept fixed and the ray window in Figure 60 is rotated. This method is applied to simple shapes. On the other hand, in the second method the target is rotated while the ray window is kept fixed. Target rotation is explained in next section. After that detailed monostatic RCS results of complex targets such as F-117, eurofighter and F-16 aircrafts are presented.
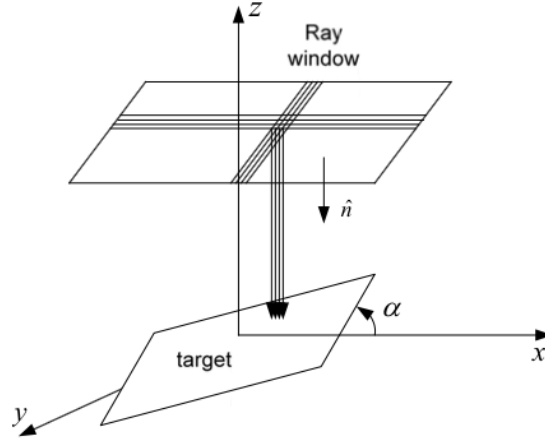
Figure 60 Simple target rotation geometry

3.1 Target Rotation

For the visualization of RCS variation, we obtain plots of RCS versus aspect angles. Aspect angle is the orientation of target relative to the source position which is a ray window. In order to calculate the RCS as a function of aspect angle, the target is rotated. In order to rotate the target in three dimensions, three basic rotation matrices are used;

$$R_x(\alpha) = \begin{bmatrix} 1 & 0 & 0 \\ 0 & \cos(\alpha) & -\sin(\alpha) \\ 0 & \sin(\alpha) & \cos(\alpha) \end{bmatrix} \tag{3.1}$$

$$R_y(\alpha) = \begin{bmatrix} \cos(\alpha) & 0 & \sin(\alpha) \\ 0 & 1 & 0 \\ -\sin(\alpha) & 0 & \cos(\alpha) \end{bmatrix} \tag{3.2}$$

$$R_x(\alpha) = \begin{bmatrix} \cos(\alpha) & -\sin(\alpha) & 0 \\ \sin(\alpha) & \cos(\alpha) & 0 \\ 0 & 0 & 1 \end{bmatrix} \tag{3.3}$$

Each of these matrices rotates a target in counterclockwise direction around a fixed coordinate axis, by an angle of α . Rotation direction is determined by the right-hand rules. Other rotation matrices are derived from these three basic matrices.

In our simulations, for rotating a target that is in STL mesh format, all vertices of triangular patches are rotated about the orthogonal axes of the global coordinate system. Simple rotation geometry is illustrated in Figure 61.
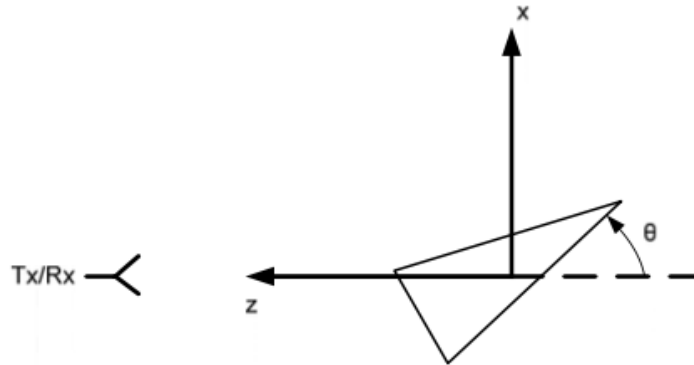
Figure 61 Fixed rotation around Y axis

3.2 Numerical Results

3.2.1 RCS Analysis of F-117 Aircraft

The first complex model that the RCS analysis is presented is a simplified model F-117 aircraft.

| (a) | (b) |
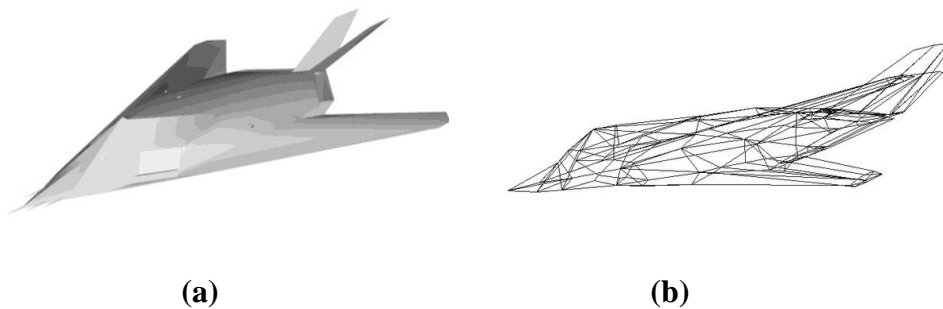
Figure 62 (a) Solid model of F-117 (b) Mesh geometry of F-117

Size of the aircraft model is 10m and the mesh model consists of 320 triangular plates. Figures 63 and 64 presents monostatic RCS values of F-117 at 1 GHz and 12 GHz respectively. The RCS analysis has been conducted at φ=0° azimuth angle and θ=[-80°,80°] elevation angle interval with angular increments of 1°.

Table 8 shows the number of rays shot into the target at 1 and 12 GHz frequency values. As the frequency level increases, number of rays in the analysis and computation time also increases. Results obtained by PO and SBR methods are compared in the plots.

Table 8 Number of rays vs frequency for F-117 case

Frequency [GHz]	Number of Rays
1	4350
12	640000
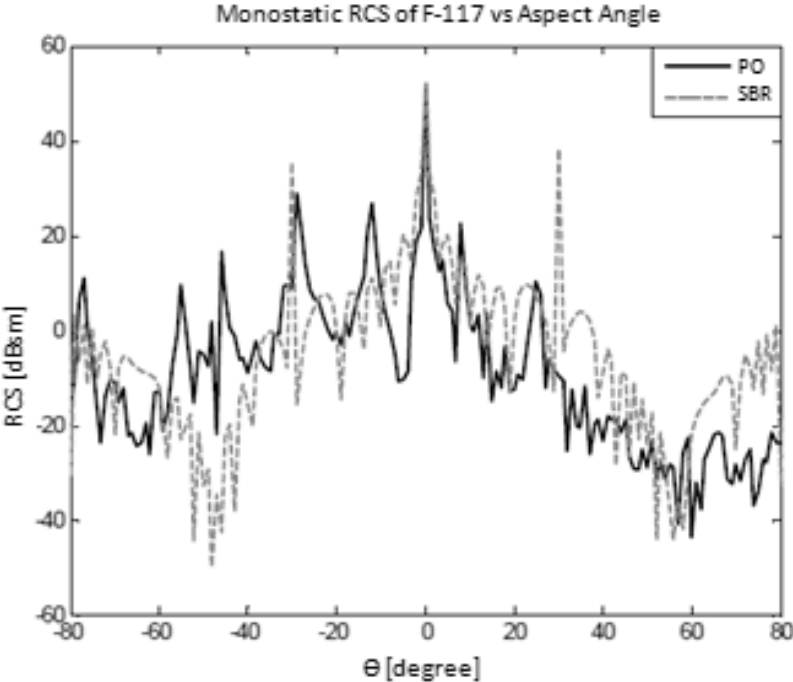
Figure 63 Monostatic RCS of F-117 vs elevation angle with PO and SBR methods at vertical polarization, 1 GHz

As seen in Figure 63 results obtained from PO and SBR methods have similar tendency in [+30°, -30°] elevation angle interval. Results deviate in other intervals due to multiple reflection and edge diffraction effects.

Table 9 Computation time for F-117 case

Ray-triangle intersection test method	Number of Triangular Plates	Computation time [sec]
Badouel	320	1920
Moller-Trumbore	320	1850
Plucker	320	1510

Table 9 presents the estimated computation times necessary for ray-triangle intersection tests with Badouel, Moller-Trumbore and Plucker methods. It can be concluded that Plucker test provides 20% less computation time than Badouel method does.
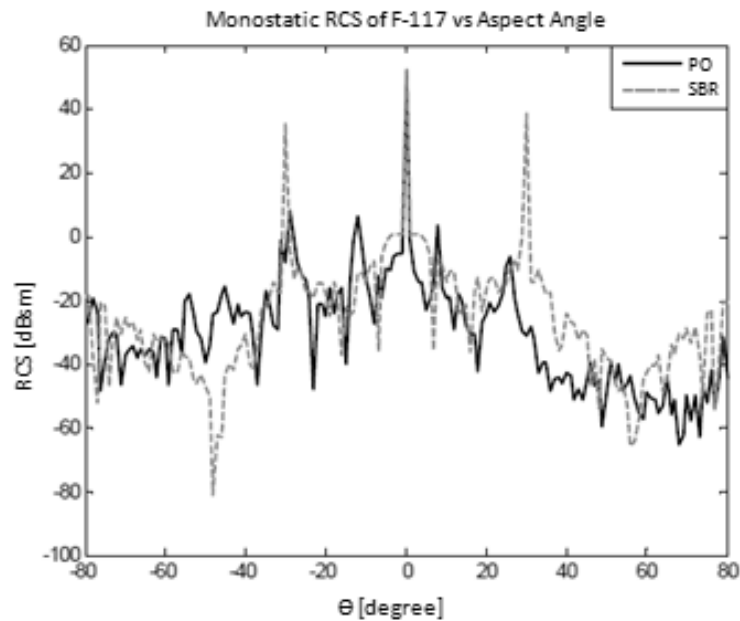
Figure 64 Monostatic RCS of F-117 vs elevation angle with PO and SBR methods at vertical polarization, 12 GHz

As seen in Figure 64 results obtained from PO and SBR methods have dissimilar tendency throughout the elevation angle interval. Results deviate due to multiple reflection and edge diffraction effects. At an elevation angle of (θ) 30° RCS result obtained from PO is -28 dBsm whereas SBR gives 39 dBsm.

3.2.2 RCS Analysis of Eurofighter Aircraft

The second RCS simulation on complex targets has been run on Eurofighter aircraft (Fig. 65). The length of the target is 18 m and consists of 955 triangular plates. A ray window big enough to illuminate this model consists of 4400 rays at 1 GHz with λ spacings.
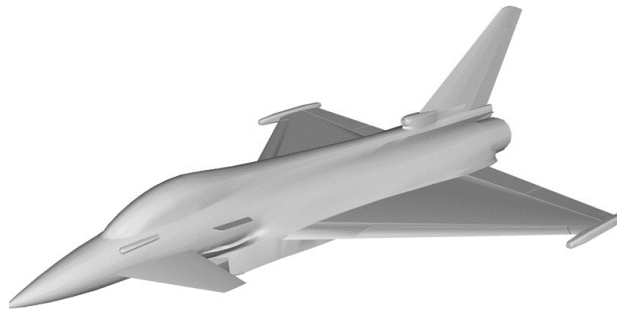
Figure 65 Eurofighter computer aided design model

RCS analysis for Eurofighter has been conducted at 1 GHz at an azimuth angle of φ=0° and elevation angle (θ) interval of [-90°,90°] at vertical polarization. Results obtained by SBR and PO have been compared in Figure 66.
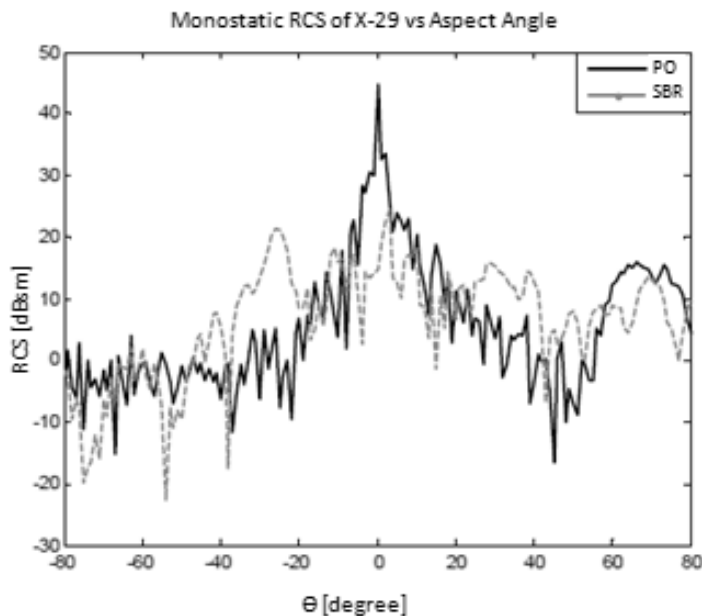
Figure 66 Monostatic RCS of Eurofighter vs elevation angle with PO and SBR methods at vertical polarization, 1 GHz

As seen in Figure 66 results obtained from PO and SBR methods have dissimilar tendency throughout the elevation angle interval. Results deviate due to multiple reflection and edge diffraction effects. It can be observed that maximum value occurs at an elevation angle of 0°.

Table 10 Computation time for Eurofighter case

Ray-triangle intersection test method	Number of Triangular Plates	Computation time [sec]
Badouel	955	3420
Moller-Trumbore	955	3350
Plucker	955	2810

Table 10 presents the estimated computation times necessary for ray-triangle intersection tests with Badouel, Moller-Trumbore and Plucker methods. It can be concluded that Plucker test provides 20% less computation time than Badouel method does.

3.2.3 RCS Analysis of F-16 Aircraft

The third RCS simulation on complex targets has been run on F-16 aircraft (Fig. 65). The length of the target is 16 m and consists of 12500 triangular plates. A ray window big enough to illuminate this model has been prepared with λ spacings and number of rays per frequency value has been provided in Table 11.

Table 11 Number rays vs frequency for F-16 case

Frequency [GHz]	Number of Rays
2	4350
8	110900
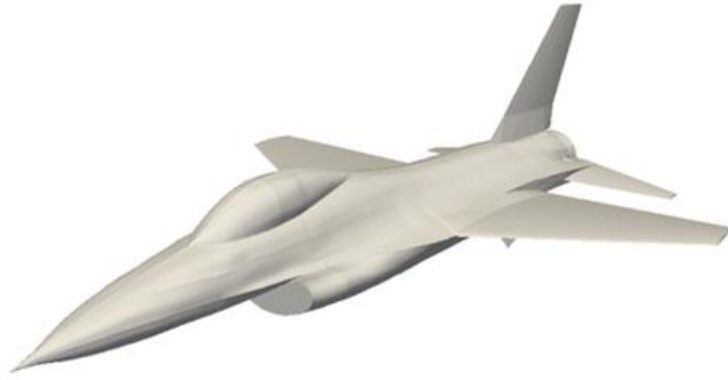
Figure 67 (a) Solid model of F-16

Monostatic RCS values of F-16 model illuminated at an azimuth angle of φ=0° and an elevation angle of θ=0° has been presented in Figure 68 in a frequency interval of [2-18] GHz.
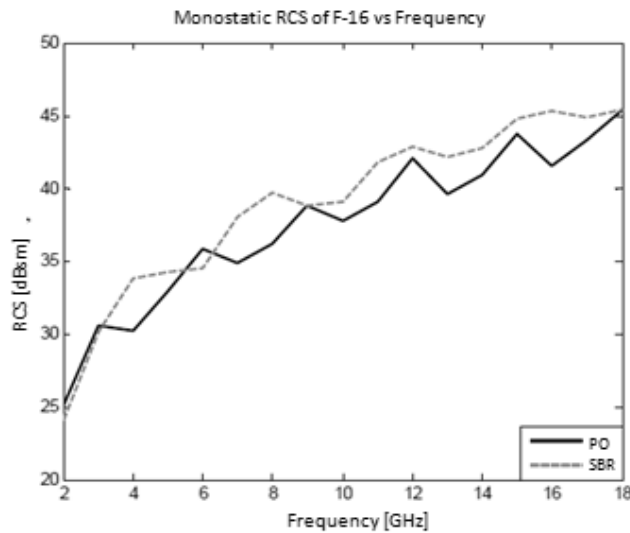
Figure 68 Monostatic RCS of F-16 vs frequency with PO and SBR methods at vertical polarization, φ=0° and θ=0°

In Figure 68, RCS results obtained by PO and SBR methods have been compared. It can be observed that PO and SBR curves have similar tendency in the frequency domain of interest. As the frequency is increased, the wavelength gets smaller compared to the aircraft size. Since the electric field integral depends on wavelength, RCS of the aircraft increases.

Monostatic RCS values of F-16 model illuminated at an azimuth angle of φ=0° and an elevation angle interval of θ=[0°, 180°] has been presented at vertical and horizontal polarizations in Figures 69 and 70 respectively. Also results obtained by SBR and PO have been compared in the Figures.
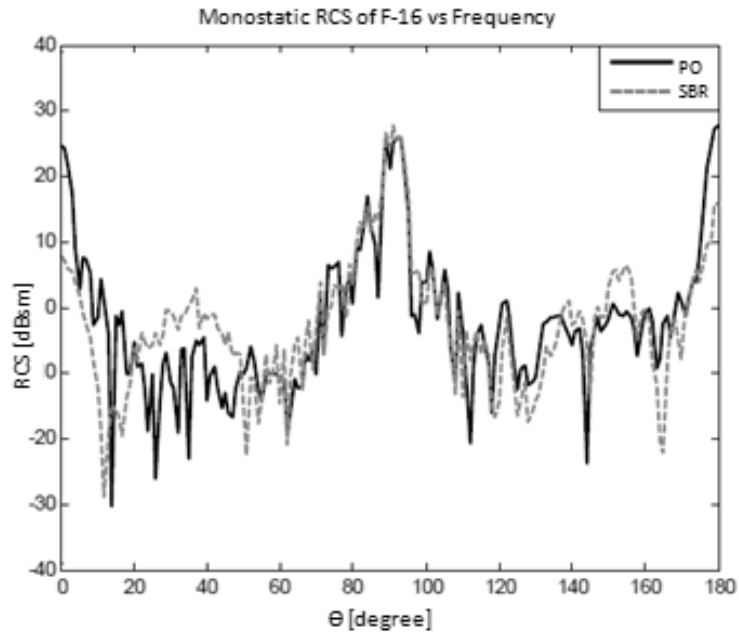


Figure 69 Monostatic RCS of F-16 vs elevation angle with PO and SBR methods at vertical polarization, 2 GHz

As seen in Figure 69 results obtained from PO and SBR methods have dissimilar tendency in the elevation angle intervals of [20°, 60°] and [150°, 160°] due to multiple reflections. PO and SBR results match perfectly in other intervals. It can be observed that maximum value occurs at an elevation angle of 0°.
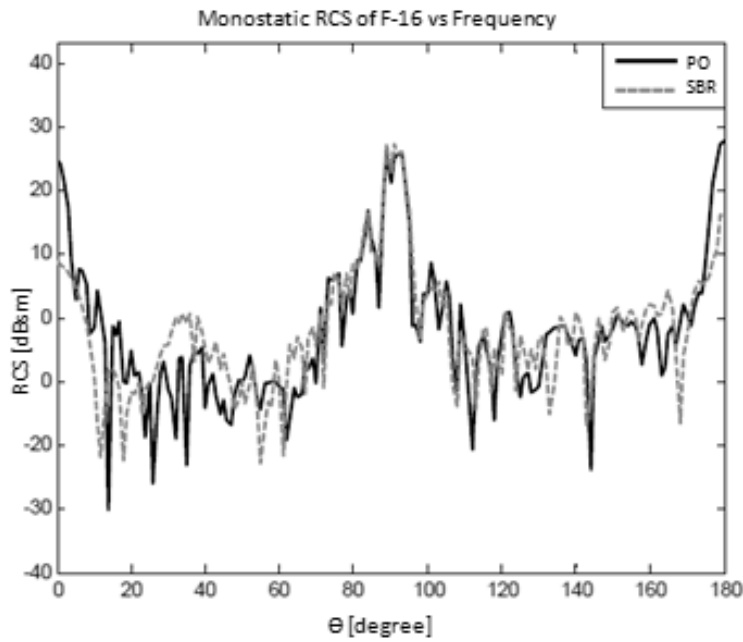
Figure 70 Monostatic RCS of F-16 vs elevation angle with PO and SBR methods at horizontal polarization, 2 GHz

As seen in Figure 70 results obtained from PO and SBR methods have dissimilar tendency in the elevation angle intervals of [25°, 50°] and [160°, 170°] due to multiple reflections. PO and SBR results match perfectly in other intervals. It can be observed that maximum value occurs at an elevation angle of 0°.

Table 12 Computation time for F-16 case

Ray-triangle intersection test method	Number of Triangular Plates	Computation time [sec]
Badouel	12500	9700
Moller-Trumbore	12500	8700
Plucker	12500	7000

Table 12 presents the estimated computation times necessary for ray-triangle intersection tests with Badouel, Moller-Trumbore and Plucker methods. It can be concluded that Plucker test provides 25% less computation time than Badouel method does.

Monostatic RCS values of F-16 model illuminated at an azimuth angle of φ=0° and an elevation angle interval of θ=[0°, 180°] has been presented at vertical and horizontal polarizations in Figures 71 and 72 respectively. Analysis has been

conducted at 8 GHz frequency with angular increments of 1°. Also results obtained by SBR and PO have been compared in the Figures.
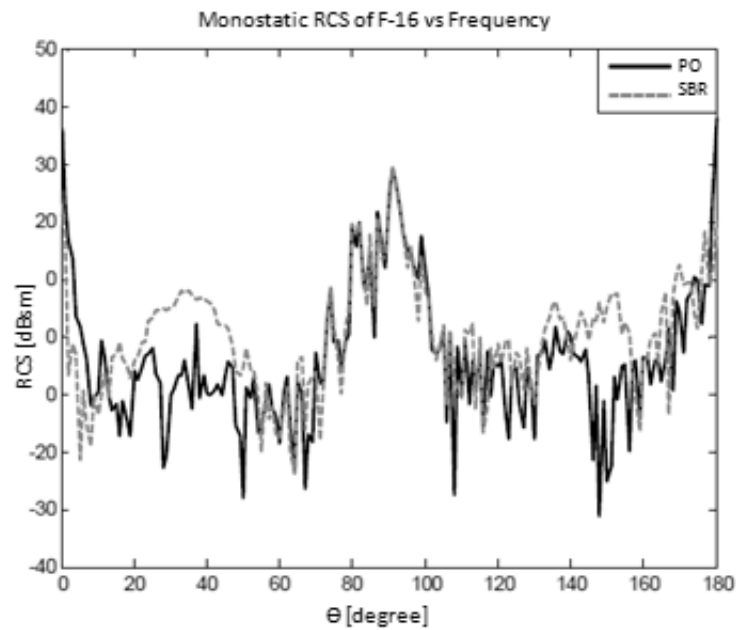
Figure 71 Monostatic RCS of F-16 vs elevation angle with PO and SBR methods at vertical polarization, 8 GHz

As seen in Figure 71 results obtained from PO and SBR methods have dissimilar tendency in the elevation angle intervals of [10°, 50°] and [140°, 160°] due to multiple reflections. PO and SBR results match perfectly in other intervals. It can be observed that maximum value occurs at an elevation angle of 0°.
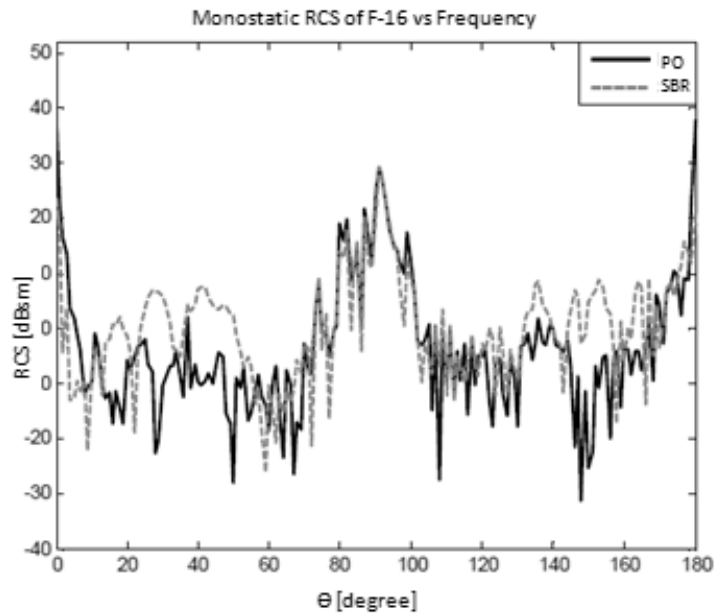
Figure 72 Monostatic RCS of F-16 vs elevation angle with PO and SBR methods at horizontal polarization, 8 GHz

As seen in Figure 72 results obtained from PO and SBR methods have dissimilar tendency in the elevation angle intervals of [10°, 60°] and [130°, 160°] due to multiple reflections. PO and SBR results match perfectly in other intervals. It can be observed that maximum value occurs at an elevation angle of 0°.

Monostatic RCS values of F-16 model illuminated at an azimuth angle interval of φ=[0°-360°] and an elevation angle interval of θ=90° has been presented at vertical and horizontal polarizations in Figures 73 and 74 respectively. Analysis has been conducted at 10 GHz frequency with angular increments of 1°. Also results obtained by SBR and PO have been compared in the Figures.
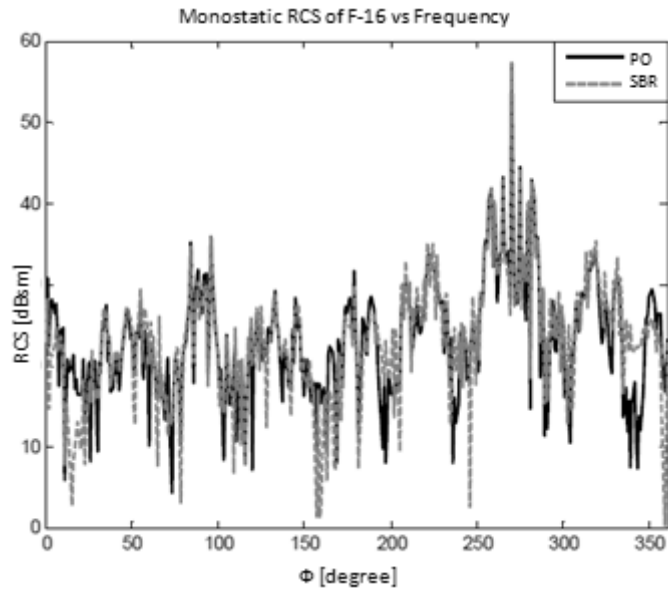
Figure 73 Monostatic RCS of F-16 vs elevation angle with PO and SBR methods at vertical polarization, 10 GHz

As seen in Figure 73 results obtained from PO and SBR methods have dissimilar tendency in the azimuth angle intervals of [10°, 25°] and [330°, 350°] due to multiple reflections. PO and SBR results match perfectly in other intervals. It can be observed that maximum value occurs at an azimuth angle of 270°.
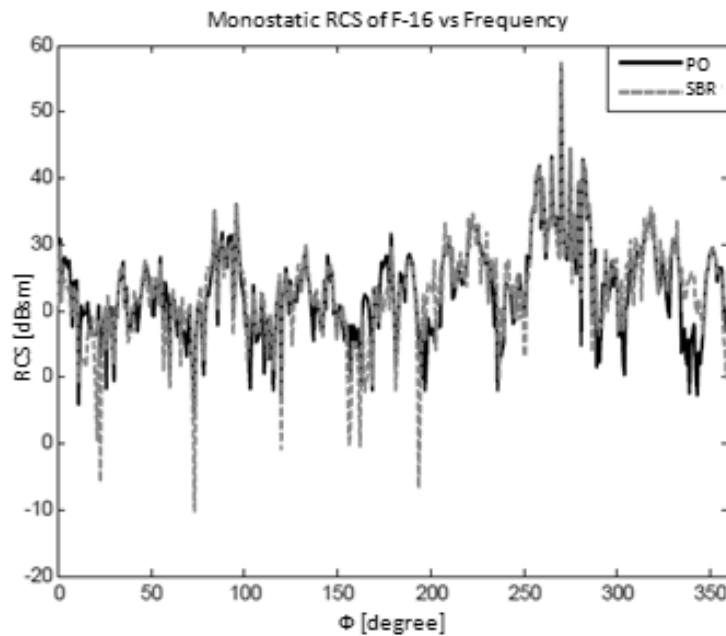
Figure 74 Monostatic RCS of F-16 vs elevation angle with PO and SBR methods at horizontal polarization, 10 GHz

As seen in Figure 74 results obtained from PO and SBR methods have dissimilar tendency in the azimuth angle interval of [330°, 350°] due to multiple reflections. PO and SBR results match perfectly in other intervals. It can be observed that maximum value occurs at an azimuth angle of 270°.

CHAPTER 4

DIFFRACTION EFFECTS IN RADAR CROSS SECTION ANALYSIS

The physical optics (PO) scattered field from perfectly electrically conducting structures is limited in accuracy because the PO current fails to closely approximate the exact current near surface discontinuities such as edges. ''The accuracy of the PO scattered field can be significantly increased by adding the fringe wave (FW) field, which takes into account the distortion of the current caused by edges. An approximation to the FW field can be calculated by integrating physical theory of diffraction equivalent edge currents along the illuminated part of the edges of the structure. These edge currents are determined from an integration of the FW current (the exact current minus the PO current) along incremental strips on the canonical wedge or half-plane. Throughout this study physical theory of diffraction equivalent edge currents will be considered, and these will be referred to as EEC's.

4.1 Equivalent Edge Currents

Closed-form expressions for EEC's have been derived for un-truncated (infinite) incremental wedge strips by *Michaeli* **[10]**, *Mitzner* **[17]**, and *Shore et al.* **[18]**. These EEC's will be called un-truncated EEC's in this study. For the analysis of bistatic radar scattering the un-truncated EEC's give an inadequate correction to the PO field due to the presence of the Ufimtsev singularity and the discontinuities of the calculated FW field across the current layers associated with the un-truncated strips. The Ufimtsev singularity occurs when the direction of observation is the continuation of an incident field grazing the face of the structure.

The above-mentioned problems associated with the un-truncated EEC's are eliminated by using truncated (finite) strips. Closed-form expressions for EEC's have been derived for truncated incremental half-plane strips by *Breinbjerg* [19] and by *Shore and Yaghjian. Cote et al.* have implicitly derived EEC's for truncated incremental strips on a right-angled wedge. Michaeli seems to be the only one who has derived EEC's for general truncated incremental wedge strips; the EEC's based on truncated wedge strips will in this report be called truncated EEC's. They apply to the analysis of bistatic radar scattering from three- dimensional structures with flat faces. However, from theoretical considerations, as well as numerical calculations, it appears that Michaeli's truncated EEC's contain non-removable singularities which give rise to numerical problems and thus hamper their application. The singularities are caused by the mathematical procedure applied to obtain closed-form expressions, and they occur for special directions of incidence and observation and for zero strip length." [22]

Discontinuities and nonremovable singularities in EEC's employed in general computer codes are unwanted for two reasons. First, the prediction of the scattered field for directions of observation close to discontinuities and nonremovable singularities is clearly inaccurate. Second, the nonremovable singularities give rise to numerical problems in computing the line integral along the edges of the structure. Although the nonremovable singularities usually are confined to a narrow angular region of observation, they do constitute a problem in applications in which the scattered field has to be calculated for all directions of observation. For those reasons, the untruncated EEC's and Michaeli's truncated EEC's are not suitable for the implementation of computer codes.

In this study truncated EEC's derived by *Johansen* [20] are utilized. "These EEC's do not have the above-mentioned singularity problems of the previously reported expressions, that is, they are well behaved for all directions of incidence and observation and they take a finite value for zero strip length. This means that the new truncated EEC's are, to the knowledge of the author, the first EEC's that are well suited for implementation in general computer codes. [22]
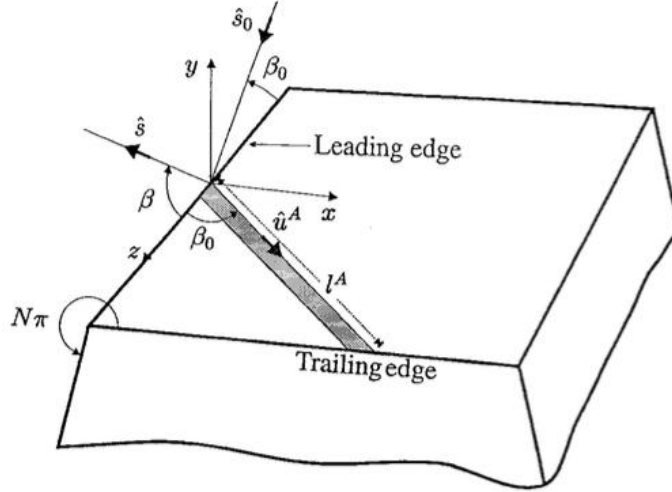
Figure 75 Three-dimensional view of a flat face of a three-dimensional structure. The truncated incremental strip extends from the leading edge to the trailing edge and is directed along the unit vector $\hat{\mathbf{u}}^A$ The directions of incidence and observation are $\hat{s}_0$ and $\hat{s}$, respectively $\mathbf{N\pi}$ is the exterior wedge angle, and it is assumed that

$$1 < N \leq 2$$

4.1.1 The Concept of Truncated EEC's

The configuration under consideration is a perfectly con- ducting three-dimensional structure with flat faces illuminated by a plane wave (see Fig. 75). In the far field of the structure, a high-frequency approximation to the FW field is calculated from a line integral along the illuminated part *C* of the edges of the structure. The truncated EEC's are represented by the magnetic current *MT* and the electric current *I,* so that the electric FW field is given by

$$\vec{E}^{fw} = jk \int_C (ZI_T \hat{s} \times (\hat{s} \times \hat{t}) + M_T \hat{s} \times \hat{t}) \frac{\exp(-jks)}{4\pi s} dC$$
(4.1)

Herein, *j* is the imaginary unit (the time factor *exp (jwt)* is suppressed), *k* is the wave number, *Z* is the intrinsic impedance of the ambient medium, $\vec{s} = \hat{s}s$ is the vector to the far-field observation point, and $\hat{t}$ is the edge unit tangent vector. The two adjoining faces at each edge are denoted by *A* and *B*. Introducing a local rectangular *xyz* system at the integration point with $\hat{z} = \hat{t}$ and $\hat{y}$ being the outward normal unit vector of face *A,* $\hat{s}$ is expressed as $\hat{s} = \hat{x}\sin\beta\cos\phi + \hat{y}\sin\beta\sin\phi + \hat{z}\cos\beta$ and the

propagation direction $\hat{s}_0$ of the incident plane wave is $\hat{s}_0 = -\hat{x}\sin\beta_0\cos\phi_0 - \hat{y}\sin\beta_0\sin\phi_0 + \hat{z}\cos\beta_0$ of incident plane wave is (see Figs. 73 and 74). Face B is located in the plane described by $\phi = N\pi$ where $N\pi$ is the exterior wedge angle. Throughout the section it is assumed that $1 < N \leq 2$.
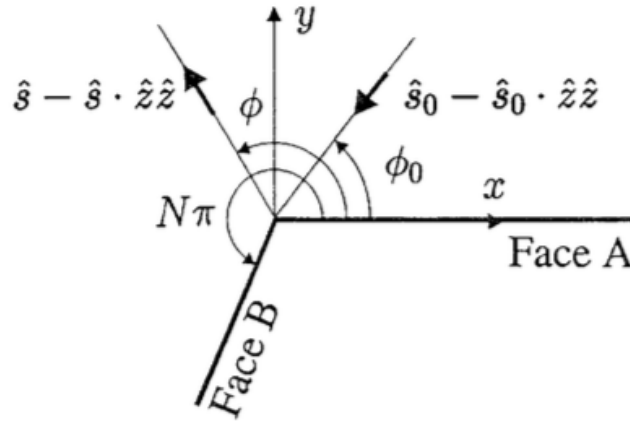
Figure 76 Two-dimensional view of the configuration shown in Fig. 75 in the plane

$$z = 0$$

The truncated EEC's are determined by a sum of two contributions, one from each of the faces A and B

$$M_T = M_T{}^A + M_T{}^B \quad \text{and} \quad I_T = I_T{}^A + I_T{}^B \tag{4.2}$$

Henceforth, the superscripts A and B refer to the contributions from the faces A and B, respectively. In this paper, the contribution from face A will be derived in detail, and the contribution from face B is then obtained from the result for face A using a substitution technique.

"The contribution from face A to the truncated EEC's, $M_T{}^A$ and $I_T{}^A$, is calculated analytically by integrating the FW current on face A of a wedge appropriately conforming to the structure along a truncated incremental strip with the length l^A. The strip extends from the leading edge (the edge at which the EEC's are placed) to the trailing edge and is directed along the unit vector $\hat{u}^A$ which is the intersection of

the Keller cone and the face A. as shown in Fig. 75. However, the integration of the exact FW current along the truncated incremental strip cannot be performed exactly in closed form, and thus, an asymptotic calculation is necessary. To this end, the truncated EEC's are expressed as the difference between the untruncated EEC's and the correction EEC's. **[22]**

$$M_T = M_{UT} + M_{cor} \quad \text{and} \quad I_T = I_{UT} + I_{cor} \tag{4.3}$$

Michaeli found that the untruncated EEC's can be expressed exactly in closed form, whereas closed-form expressions for the correction EEC's can only be obtained using an asymptotic technique. In the present paper, Michaeli's untruncated EEC's are used but a new asymptotic calculation of the correction EEC's is performed because Michaeli's correction EEC's contain nonremovable singularities.

The contribution from face *A* to the untruncated EEC's, $M_{UT}{}^A$ and $I_{UT}{}^A$, is obtained by integrating the FW current on face *A* along an untruncated incremental strip. The strip extends from the leading edge and is directed along $\hat{u}^A$.

Michaeli found that

$$M_{UT}^A = \frac{2jZH_{z0}\sin\phi}{k\sin\beta_0\sin\beta}\left(\frac{U(\pi-\phi_0)}{\mu+\cos\phi_0} + \frac{\sin\frac{\pi-\alpha}{N}}{N\sin\alpha(\cos\frac{\pi-\alpha}{N}-\cos\frac{\phi_0}{N})}\right) \tag{4.4}$$

and

$$I_{UT}^A = \frac{2j}{kN\sin\beta_0(\cos\frac{\pi-\alpha}{N}-\cos\frac{\phi_0}{N})} \cdot \left(\frac{H_{z0}\sin\frac{\pi-\alpha}{N}}{\sin\alpha}(\cot\beta\cos\phi - \mu\cot\beta_0) - \frac{E_{z0}\sin\frac{\phi_0}{N}}{Z\sin\alpha}\right) +$$

$$\frac{2jU(\pi-\phi_0)}{k\sin\beta_0(\mu+\cos\phi_0)}\cdot\left(H_{z0}(\cot\beta\cos\phi_0) - \frac{E_{z0}\sin\phi_0}{Z\sin\beta_0}\right) - \frac{2j\cot\beta_0 H_{z0}}{\frac{2j}{kN\sin\beta_0(\cos\frac{\pi-\alpha}{N}-\cos\frac{\phi_0}{N})}} \tag{4.5}$$

where H_{z0} and E_{z0} are the *z* components of the incident magnetic and electric field, respectively, at the origin of the local *xyz* system and $U(x)$ is the unit step function.

Moreover,

$$\mu = \frac{\sin\beta_0\sin\beta\cos\phi+\cos\beta_0(\cos\beta-\cos\beta_0)}{\sin^2\beta_0} \tag{4.6}$$

and α is the solution to $\mu = cos\alpha$ determined by

$$\alpha = -jLog(\mu + \sqrt{\mu^2 - 1}$$ (4.7)

with $Logz = \ln|z| + jArgz$ and $-\pi < Argz \leq \pi$. The square root in Eq. 4.7 is defines as

$$\sqrt{\mu^2 - 1} = \begin{cases} -\left|\sqrt{\mu^2 - 1}\right|, & \mu < -1 \\ j\left|\sqrt{\mu^2 - 1}\right|, & -1 < \mu < -1 \end{cases}$$ (4.8)

The only nonremovable singularity in M_{UT}^A and I_{UT}^A is the Ufimtsev singularity which occurs when $\mu = 1$ ($\alpha = 0$) and simultaneously, $\phi_0 = \pi$ that is, when the direction of observation is the continuation of an incident field grazing face A.

The contribution from face A to the correction EEC's, M_{cor}^A and I_{cor}^A, is obtained by integrating the FW current on face A along another untruncated incremental strip. This strip extends from the point of truncation at the trailing edge and is directed along $\hat{u}^A$. Michaeli found that

$$M_{cor}^A = -Zsin\beta_0 \frac{sin\phi}{sin\beta} L_x{}^A$$ (4.9)

and

$$I_{cor}^A = sin\beta_0 (L_z{}^A - cot\beta cos\phi L_z{}^A)$$ (4.10)

with

$$L_{x,z}^A = \int_{l^A}^{\infty} J_{x,z}^{fw,A} \exp(jku\hat{s} \cdot \hat{u}^A) \, du$$ (4.11)

where $J_{x,z}^{fw,A}$ denotes the x- and z components of the FW current on face A. "The approach used by Michaeli to calculate the integral $L_{x,z}^A$ in is as follows. First, the expressions for the exact FW current, which is given in terms of contour integrals in the complex plane, are inserted into the integral (4.11). Next, the order of integration is interchanged, the inner integral is calculated analytically and finally, the resulting integral is evaluated asymptotically for $L = kl^A sin^2\beta_0 \gg 1$. However, this asymptotic evaluation gives rise to two problems in the correction EEC's when N $\neq$

2. First, the correction EEC's tend to infinity as L → 0. The quantity L can become small for edge points close to corners in the evaluation of the integral (4.1). As discussed in [21], it is possible to avoid small values of L by omitting part of the edge which is close to comers. However, this approach is not robust in practical applications because the ca1culated field will depend on the ratio of the edge being omitted. Second, the correction EEC's contain nonremovable singularities for $\phi_0 = -(\pi + \alpha) + 2\pi$, and for $\alpha = \pi$, and they are caused by the fact that only few of the poles potentially nearby the saddle point are isolated in the decomposition [21], applied by Michaeli. For a detailed discussion on these singularities, the reader is referred to [22]. The singularities occur for various directions of incidence and observation. It should be noted that no singularity problems occur in the correction EEC's when N = 2. [22]

.

4.1.2 Derivation of New Correction EEC's

In this section, a new approach derived by *Johansen* [20] is used to calculate the correction EEC's. Instead of employing the exact expressions for the FW current when calculating the integral $L_{x,z}^A$ in (4.11), the asymptotic expressions for the FW current are employed. Thus, the first thing that will be dealt with in this section is the determination of the asymptotic expressions for the FW current.

4.1.2.1 Uniform Asymptotic Expressions for the FW Current on Face A

The *x* component of the FW current on face *A* is given by

$$J_x^{fw,A} = \frac{H_{z0}\exp{(-jkz\cos\beta_0)}}{j\pi N} \cdot \int_\Gamma \frac{\sin\frac{\xi}{N}\exp(jkx\sin\beta_0\cos\xi)d\xi}{\cos\frac{\xi}{N}-\cos\frac{\phi_0}{N}} \qquad (4.12)$$

where Γ is the steepest descent path trough π. Using the substitution

$$s = -\sqrt{\frac{2}{j}}\cos\frac{\xi}{2} \qquad (4.13)$$

where $\sqrt{j}$ means $(j\frac{\pi}{4})$, and a decomposition technique similar to the one applied by Michaeli **[10]** to isolate the pole potentially nearby the saddle point *(s = 0)*, the integrand in (4.12) is written as a sum of a simple pole term and a regular term so that

$$J_x^{fw,A} = \frac{\sqrt{2}H_{z0}\exp\left(-jk\hat{u}^A\cdot\vec{r}\right)}{\sqrt{j}\pi N} \cdot \int_{-\infty}^{\infty}\left(\frac{A}{s+\frac{a}{\sqrt{j}}} + R(\xi)\right)\exp(-kx\sin\beta_0 s^2)\,ds \quad \textbf{(4.14)}$$

Herein, $a = \sqrt{2}\cos\left(\frac{\emptyset_0}{2}\right), A = -\frac{N}{\sqrt{2j}}, \vec{r} = \hat{x}x + \hat{z}z$, and the regular term is

$$R(\xi) = \frac{\sin\frac{\xi}{N}}{\sin\frac{\xi}{2}(\cos\frac{\xi}{N}-\cos\frac{\phi_0}{N})} - \frac{A}{s+\frac{a}{\sqrt{j}}} \quad \textbf{(4.15)}$$

"The integration of the simple pole term in (4.14) is performed exactly and expressed in terms of a Fresnel function **[23]**. Since the quantity $R(\xi)$ given in (15) is regular near the saddle point, the integration of $R(\xi)$ in (14) is evaluated asymptotically for $kx\sin\beta_0 \gg 1$ using the standard steepest descent technique **[24]**." The result of these calculations is

$$J_x^{fw,A} = -2H_{z0}\exp(-jk\hat{u}^A\cdot\vec{r})$$
$$\cdot\left[\text{sign}\left(\cos\frac{\phi_0}{2}\right)F\left(\sqrt{2kx\sin\beta_0}\left|\cos\frac{\phi_0}{2}\right|\right) - \frac{1}{\sqrt{2j}\pi kx\sin\beta_0}(\frac{1}{2\cos\frac{\phi_0}{2}}\right.$$
$$\left. + \frac{\sin\frac{\pi}{N}}{N\left(\cos\frac{\pi}{N}-\cos\frac{\phi_0}{N}\right)})\right]$$

(4.16)

where *F* is a modified Fresnel function **[21]**

$$F(X) = \sqrt{\frac{j}{\pi}}\exp\left(jx^2\right)\int_{x}^{\infty}\exp(-jt^2)\,dt$$

(4.17)

A similar procedure is used to obtain the asymptotic result for $J_x^{fw,A}$

$$J_x^{fw,A} = -2\exp(-jk\hat{u}^A$$

$$\cdot \vec{r}) \left[\left(\frac{E_{z0}\sin\emptyset_0}{Z\sin\beta_0} \right. \right.$$

$$- H_{z0}\cot\beta_0\cos\emptyset_0 \Big) \text{sign}\left(\cos\frac{\emptyset_0}{2}\right) F\left(\sqrt{2kx\sin\beta_0}\left|\cos\frac{\emptyset_0}{2}\right|\right)$$

$$- \frac{E_{z0}\sin\emptyset_0}{Z\sin\beta_0 2\sqrt{2j\pi kx\sin\beta_0}\cos\frac{\Phi_0}{2}} + \frac{H_{z0}\cot\beta_0}{\sqrt{2j\pi kx\sin\beta_0}} \cdot \left(\frac{\cos\emptyset_0}{2\cos\frac{\emptyset_0}{2}}\right.$$

$$\left.\left.- \frac{\sin\frac{\pi}{N}}{N\left(\cos\frac{\pi}{N} - \cos\frac{\Phi_0}{N}\right)}\right)\right]$$

(4.18)

which applies for $kx\sin\beta_0 \gg 1$.

4.1.2.1 Expressions for the New Correction EEC's

The asymptotic expressions for the contribution from face A to the correction EEC's, M_{cor}^A in (4.9) and I_{cor}^A in (4.10), are now obtained by inserting the expressions (4.16) and (4.18) for the FW current into the integral $L_{x,z}^A$ (4.11).By using the relations

$$\int_{l^A}^{\infty} \frac{\exp\left(-jkusin^2\beta_0(1-\mu)\right)}{\sqrt{u}} du = \frac{2\sqrt{\pi}\exp\left(jL(\mu-1)\right)}{\sqrt{jk(1-\mu)}sin\beta_0} F(\sqrt{L(1-\mu)})$$

(4.19)

and

$$\int_{l^A}^{\infty} F\left(\sqrt{2kus}\sin\beta_0\left|\cos\frac{\emptyset_0}{2}\right|\right) \cdot \exp\left(-jkusin^2\beta_0(1-\mu)\right)du$$

$$= \frac{\exp\left(jL(\mu-1)\right)}{jksin^2\beta_0(\mu+\cos\phi_0)} \cdot \left(-F\left(\sqrt{2L}\left|\cos\frac{\Phi_0}{2}\right|\right)\right.$$

$$+ \frac{\sqrt{2}\left|\cos\frac{\Phi_0}{2}\right|}{\sqrt{1-\mu}} F(\sqrt{L(1-\mu)})$$

(4.20)

91

where μ and F are defined in (4.6) and (4.17), respectively, and $L = kl^A sin^2\beta_o$. the result for the new correction EEC's is obtained through a straightforward calculation **[22]**

$$M^A_{cor} = \frac{2ZH_{z0}sin\emptyset exp(jL(\mu - 1))}{jksin\beta sin\beta_0}$$

$$\cdot \left[\frac{-sign(cos\frac{\emptyset_0}{2})}{\mu + cos\phi_0}F\left(\sqrt{2L}\left|cos\frac{\phi_0}{2}\right|\right) + (\frac{\sqrt{1-\mu}}{\sqrt{2}(\mu + cos\phi_0)cos\frac{\phi_0}{2}}\right.$$

$$\left. - \frac{\sqrt{2}sin\frac{\pi}{N}}{N\sqrt{1-\mu}\left(cos\frac{\pi}{N} - cos\frac{\phi_0}{2}\right)}) \cdot F(\sqrt{L(1-\mu)}) \right]$$

(4.21)

and

$$I^A_{cor} = \frac{2exp(jL(\mu - 1))}{jksin\beta_0(\mu + cos\phi_0)}$$

$$\cdot \left[sign(cos\frac{\emptyset_0}{2}) \cdot (\frac{E_{z0}sin\phi_0}{Zsin\beta_0} - H_{z0}(cot\beta_0 cos\phi_0 + cot\beta cos\phi)) \right.$$

$$\cdot F\left(\sqrt{2L}\left|cos\frac{\phi_0}{2}\right|\right) + (\sqrt{2(1-\mu)} \cdot (-\frac{E_{z0}sin\frac{\phi_0}{2}}{Zsin\beta_0} + \frac{H_{z0}}{2cos\frac{\phi_0}{2}}$$

$$\cdot (cot\beta_0 cos\phi_0 + cot\beta cos\phi)$$

$$\left. + \frac{H_{z0}sin\frac{\pi}{N}(\mu + cos\phi_0)(cot\beta_0 - cot\beta cos\phi)}{N\left(cos\frac{\pi}{N} - cos\frac{\phi_0}{N}\right)(1-\mu)}) \cdot F(\sqrt{L(1-\mu)}) \right]$$

(4.22)

These asymptotic expressions apply for $L > 1$. The final expressions for the truncated EEC's are obtained by first calculating M^A_T and I^A_T by subtracting the above results (4.21), (4.22) from the untruncated EEC's (4.4), (4.5) (as shown in (4.3). Second, the contribution from face B is calculated using the results for M^A_T and I^A_T by replacing β_0 with $\pi - \beta_0$, β with $\pi - \beta$, ϕ_0 with $N\pi - \phi_0$, ϕ with $N\pi - \phi$. and l^A with l^B. Third, the contributions from the two faces are added to determine M_T, and I_T, see

(4.2). Finally, these expressions are inserted into the radiation integral (4.1) to determine the approximate FW field from the truncated EEC's. **[22]**

It is noted that M_{cor}^A, in (4.21) and I_{cor}^A, in (4.22) do not contain singularities for $\alpha = \pi$ ($\mu = -1$), $\emptyset_0 = -(\pi + \alpha) + 2\pi N$, and $L = 0$ as do the previously reported expressions **[21]**. Using the result of [6] it is shown that if $\phi_0 \neq \pi$, M_{cor}^A and I_{cor}^A remain bounded as $\mu \rightarrow 1$. If $\emptyset_0 = \pi$ and $\mu \rightarrow 1$, M_{cor}^A and I_{cor}^A are singular but this singularity (the Ufimtsev singularity) is cancelled by the singularity in M_{UT}^A and I_{UT}^A given by (4.4) and (4.5), respectively. This means that M_T and I_T are valid for all directions of incidence and observation. Furthermore, the fact that M_{cor}^A and I_{cor}^A are finite for $L = 0$ implies that no numerical problems arise for edge points close to comers when evaluating the integral (4.1). This is very convenient from a practical point of view. However, the field calculated from the truncated EEC's for edge points close to comers is a poor approximation to the exact field because no information on the distortion of the current near comers **[25]** is introduced.

4.1.3 Numerical Results

In this section results obtained by combining method of equivalent edge currents with SBR are presented. Results obtained for square plate, box, two boxes and F-16 aircraft are shown. First, data for square plate in the literature are used to validate the computer code consisting of combination of SBR, PTD and EEC methods.

For this purpose, case study mentioned in *Polka and Balanis* **[26]**, is handled. In this problem, Monostatic RCS of a square plate (Figure 77) mounted on xy plane and illuminated 10 GHz at an azimuth angle of φ=30° is investigated. Results for both vertical and horizontal polarizations have been presented in Figure 76 and compared with those obtained in **[26]**.
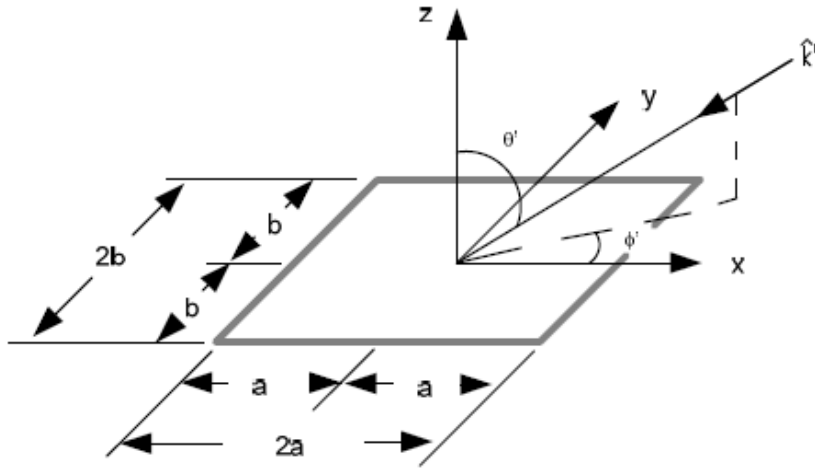
Figure 77 Square plate mounted on xy plane

| (a) | (b) |
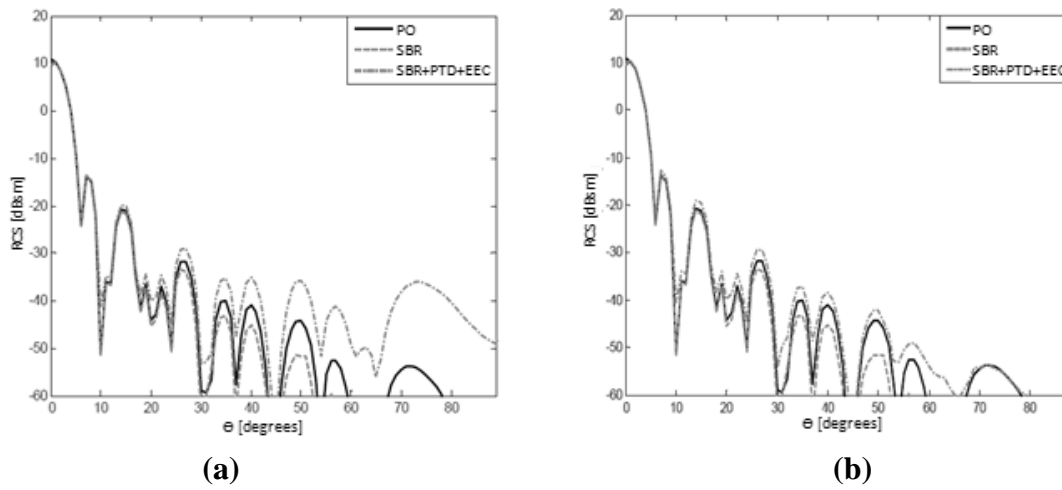
Figure 78 RCS results obtained by SBR, PTD and EEC **(a)** Horizontal polarization

(b) Vertical polarization
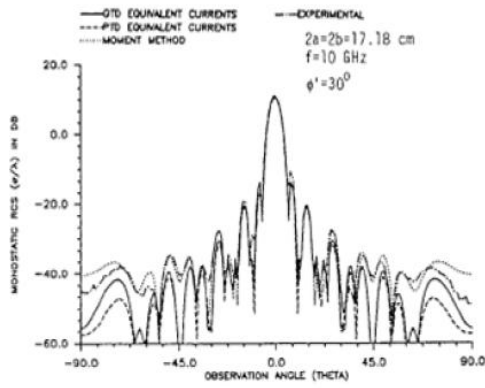
Figure 2. Monostatic RCS for a Square Plate (Soft Polarization)   Figure 3. Monostatic RCS for a Square Plate (Hard Polarization)
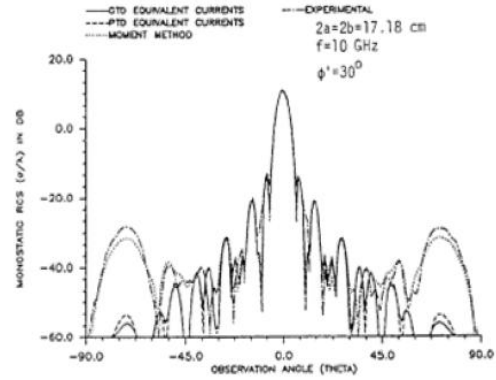
Figure 79 RCS results obtained by Polka and Balanis **(a)** Horizontal polarization **(b)** Vertical polarization

As shown in Figure 78, diffraction effects are dominant at horizontal polarization when elevation angle θ is greater than 30 degrees. On the contrary, at vertical polarization diffraction effects are weak. The results presented by Polka and Balanis in Figure 79 are compatible with SBR, PTD and EEC code. Therefore the code is validated by the literature results.

After the code is validated, the fist simulation has been run on a cube (Fig 80) consisting of 24 triangular elements with dimensions x=7 m, y=7 m and z=7 m.
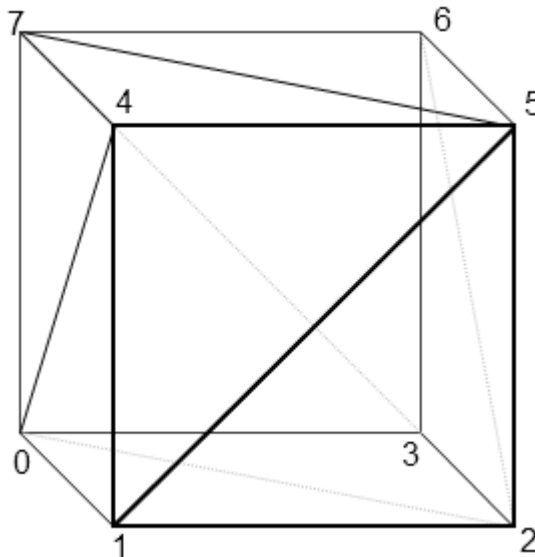
Figure 80 Meshed model of the box

Radar cross section of the cube has been investigated at 2 GHz frequency and 91° diffraction angle, at vertical and horizontal polarizations. In Figures 81 and 82 change in RCS due to changing elevation angle; whereas in Figures 81 and 84 change in RCS due to changing azimuth angle have been examined.

In Figures 81 and 82, RCS of the box has been plotted at an azimuth angle of 0° and elevation angle interval of $[0^o\text{-}180^o]$ with angular increments of 1°
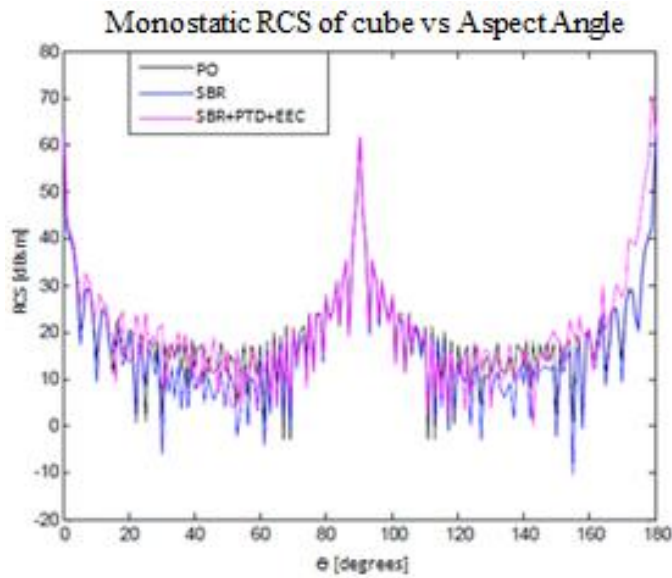
Figure 81 RCS of cube with SBR, PTD and EEC at vertical polarization

As shown in Figure 79, diffraction effects are dominant at elevation angle intervals of [170°-180°]. In other angular ranges, since diffraction effects are weak, SBR, PTD and EEC results are compatible with SBR results.
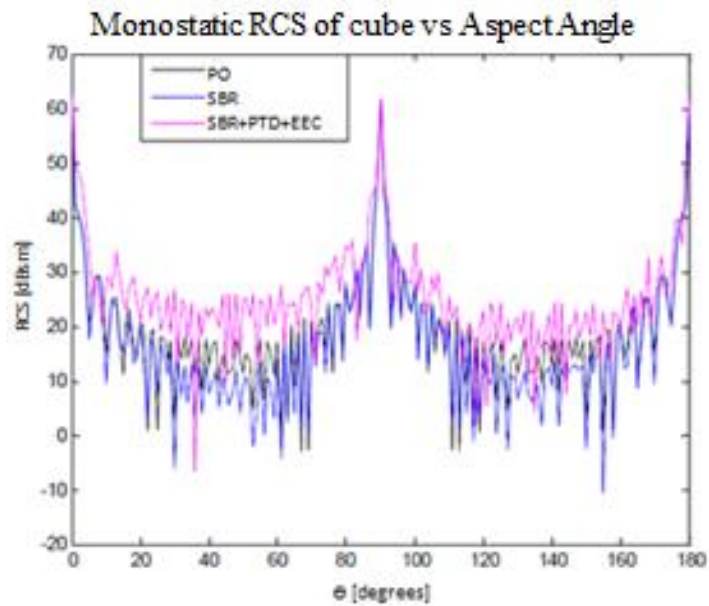
Figure 82 RCS of cube with SBR, PTD and EEC at horizontal polarization

As shown in Figure 82, diffraction effects are dominant at elevation angle intervals of [10°-85°] and [105°-170°]. Especially in [10°-85°] region the difference in RCS levels is almost 10 dBsm. In other angular ranges, since diffraction effects are weak, SBR, PTD and EEC results are compatible with SBR results.

In Figures 81 and 82, RCS of the cube has been plotted at an elevation angle of 90° and azimuth angle interval of $[0^o\text{-}360^o]$ with angular increments of 1° at vertical and horizontal polarizations respectively. The results have been obtained at 2 GHz frequency and diffraction angle has been set to 91° in order to take diffraction effects of all edges into consideration.
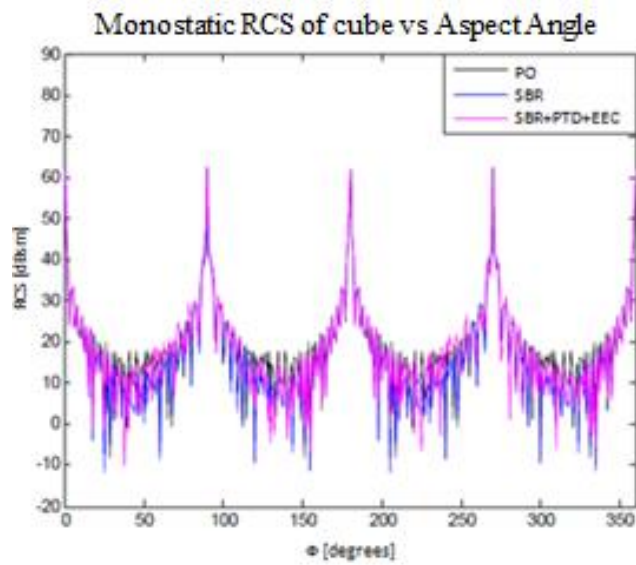
Figure 83 RCS of the cube with SBR, PTD and EEC at vertical polarization

As shown in Figure 83, SBR, PTD and EEC results are compatible with SBR results when the target is illuminated at vertical polarization in azimuth direction.
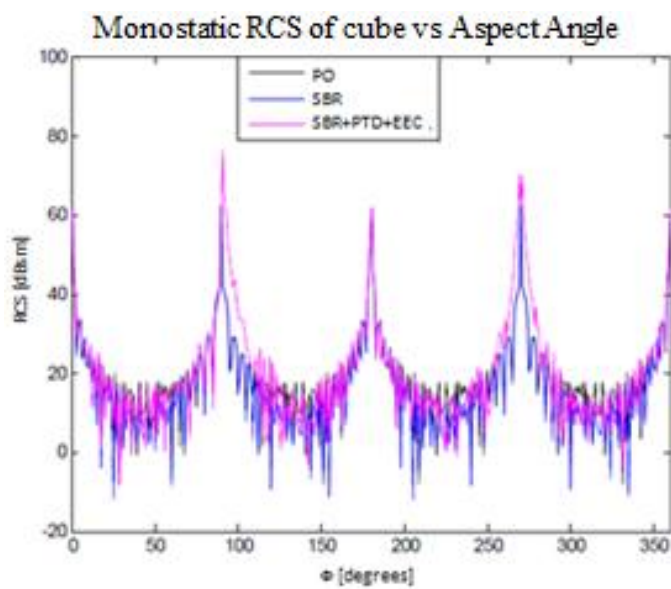
Figure 84 RCS of the cube with SBR, PTD and EEC at horizontal polarization

As shown in Figure 84, diffraction effects are dominant at azimuth angle (ϕ) intervals of [90°-110°] and [270°-290°]. In other angular ranges, since diffraction effects are weak, SBR, PTD and EEC results are compatible with SBR results.

The third problem handled to investigate is the corner reflector (Fig. 83). The straight edges of the corner reflector are equal to 4m. The results have been obtained at 8 GHz frequency and diffraction angle has been set to 91° in order to take diffraction effects of all edges into consideration. The corner reflector has been modeled using 3 triangular elements i.e. 1 triangle on each surface.
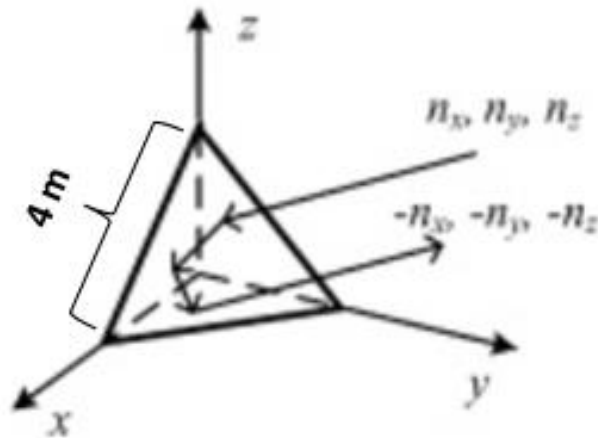
Figure 85 3D Model of corner reflector

In Figures 86 and 87, RCS of the corner reflector has been plotted at an azimuth angle of 0° and elevation angle interval of [0°-180°] with angular increments of 1° at vertical and horizontal polarizations respectively.
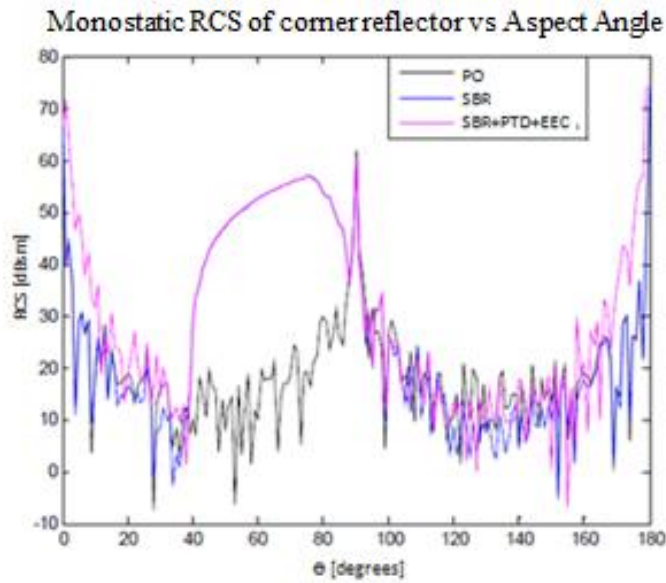
Figure 86 RCS of the corner reflector with SBR, PTD and EEC at vertical polarization

As shown in Figure 86, diffraction effects are dominant at elevation angle (θ) intervals of [0°-40°] and [150°-180°]. In other angular ranges, since diffraction effects are weak, SBR, PTD and EEC results are compatible with SBR results.
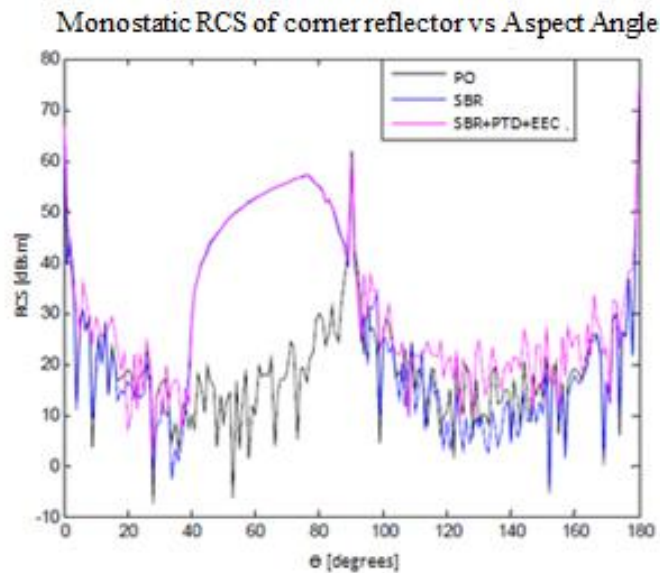
**Figure 87** RCS of the corner reflector with SBR, PTD and EEC at horizontal polarization

As shown in Figure 87, diffraction effects are dominant at elevation angle (θ) intervals of [110°-170°]. In other angular ranges, since diffraction effects are weak, SBR, PTD and EEC results are compatible with SBR results.

In Figures 88 and 89, RCS of the corner reflector has been plotted at an elevation angle of 90° and azimuth angle interval of [0°-360°] with angular increments of 5° at vertical and horizontal polarizations respectively.
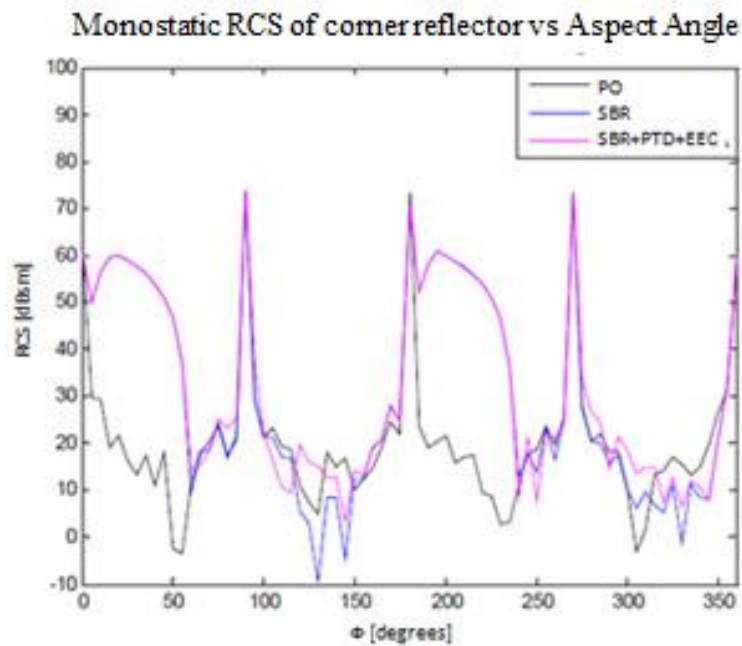
Figure 88 RCS of the corner reflector with SBR, PTD and EEC at vertical polarization

As shown in Figure 88, diffraction effects are dominant at azimuth angle (ϕ) intervals of [100°-150°] and [100°-150°]. In other angular ranges, since diffraction effects are weak, SBR, PTD and EEC results are compatible with SBR results.
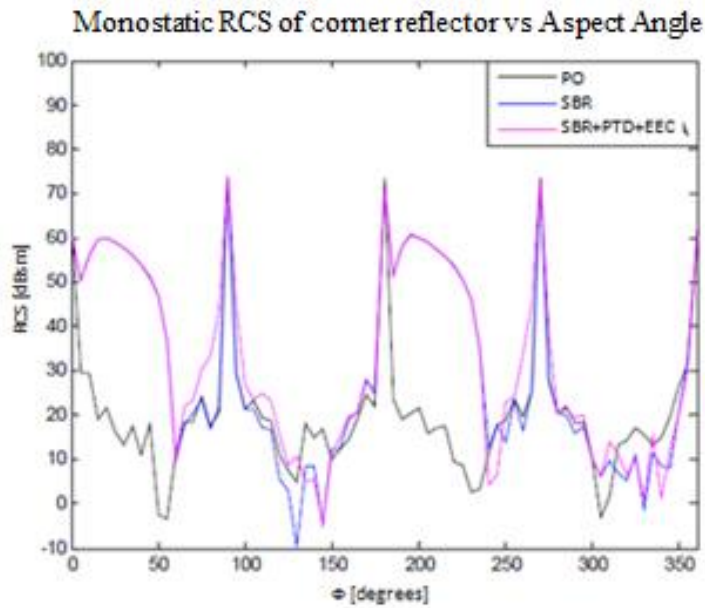
Figure 89 RCS of corner reflector with SBR, PTD and EEC at horizontal
polarization

As shown in Figure 88, diffraction effects are dominant at azimuth angle (ϕ)
intervals of [60°-150°] and [250°-270°]. In other angular ranges, since diffraction
effects are weak, SBR, PTD and EEC results are compatible with SBR results.

The last problem investigated is the F-16 aircraft case (Fig. 90). The dimensions of
the aircraft are x=15 m, y=10 m, z=4 m. The results have been obtained at 10 GHz
frequency and diffraction angle has been set to 30° and 90° in order to take
diffraction effects of all edges into consideration. RCS values obtained at vertical and
horizontal polarizations and by PO, SBR and SBR, PTD and EEC methods have
been compared in related plots.

(a)   (b)
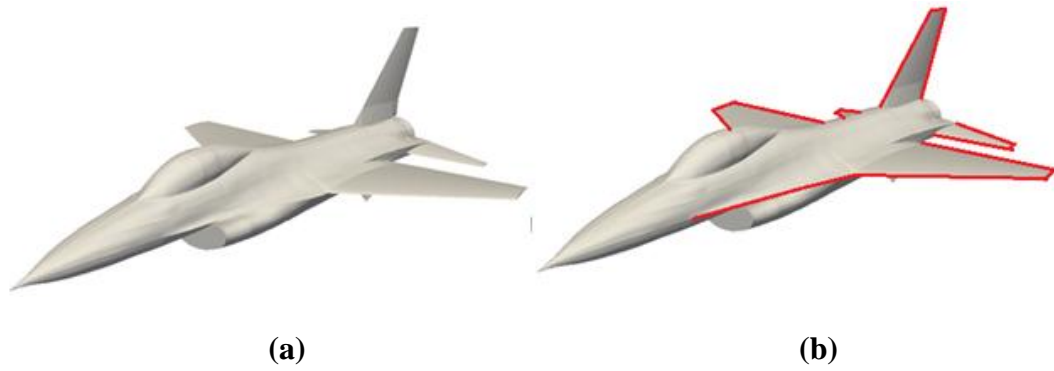
Figure 90 (a) 3D CAD model of F-16 **(b)** Dominant edges on diffraction when diffraction angle is 30° and 90°

In Figures 91 and 92, RCS of F-16 aircraft has been plotted at an elevation angle of 90° and azimuth angle interval of [0°-360°] with angular increments of 5° at vertical and horizontal polarizations respectively. The results have been obtained at 8 GHz frequency and diffraction angle has been set to 91° in order to take diffraction effects of all edges into consideration.
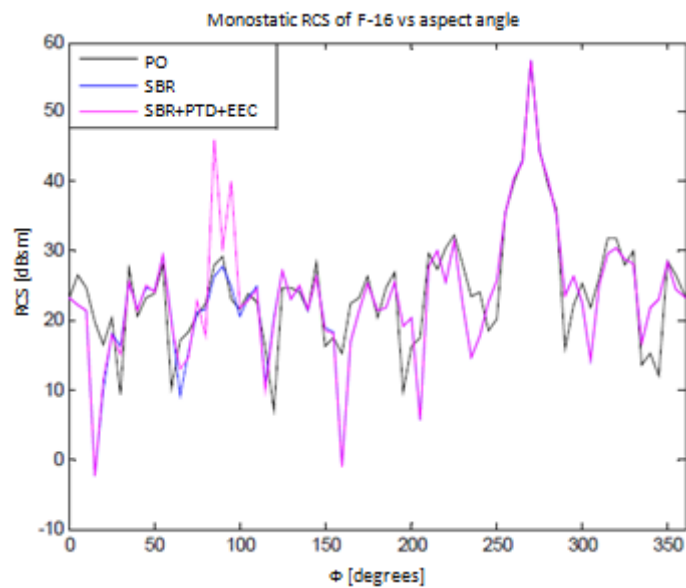
Figure 91 RCS of F-16 with SBR, PTD and EEC at vertical polarization
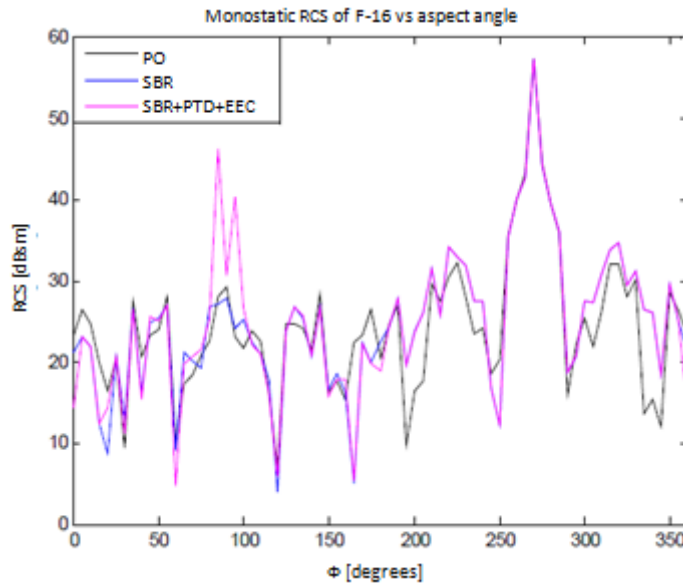
Figure 92 RCS of F-16 with SBR, PTD and EEC at horizontal polarization

As shown in Figure 91 and 92, diffraction effects are dominant at azimuth angle (ϕ) interval of [65°-100°]. Main physical features on the aircraft which contribute to diffraction are leading and trailing edges of wing, horizontal and vertical tails. In other angular ranges, since diffraction effects are weak, SBR, PTD and EEC results are compatible with SBR results.

In Figures 93 and 94, RCS of F-16 has been plotted at an azimuth angle of 0° and elevation angle interval of $[0^o\text{-}180^o]$ with angular increments of 1° at vertical and horizontal polarizations respectively. The results have been obtained at 10 GHz frequency and diffraction angle has been set to 90° in order to take diffraction effects of all edges into consideration.
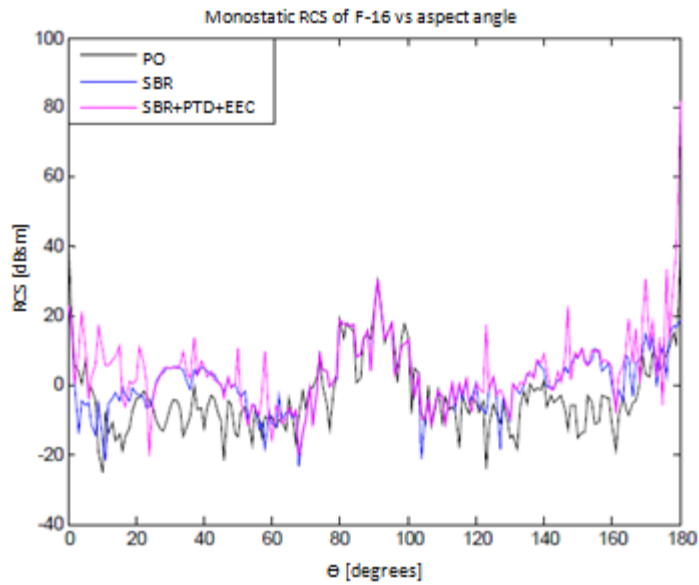
Figure 93 RCS of F-16 with SBR, PTD and EEC at vertical polarization

As shown in Figure 93, diffraction effects are most dominant at an elevation angle (θ) of 180°. 180° elevation angle coincides with the rear side of the aircraft. Also in elevation angle interval of [0°,-22°] SBR and SBR, PTD and EEC results do not match due to diffraction effects. In other angular ranges, since diffraction effects are weak, SBR, PTD and EEC results are compatible with SBR results.
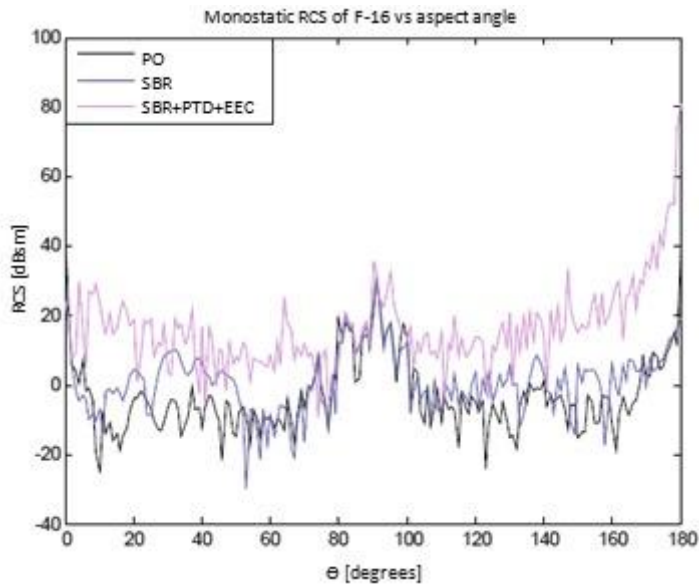
Figure 94 RCS of F-16 with SBR, PTD and EEC at horizontal polarization

As shown in Figure 94, diffraction effects are most dominant at elevation angle (θ) intervals of [0°-75°] and [91°-180°]. In other angular ranges, since diffraction effects are weak, SBR, PTD and EEC results are compatible with SBR results.

Figure 95 presents monostatic RCS values of F-16 with respect to frequency when azimuth and elevation angles are both set to 0°. The frequency interval in the analysis is [2-18] GHz with increments of 1 GHz.
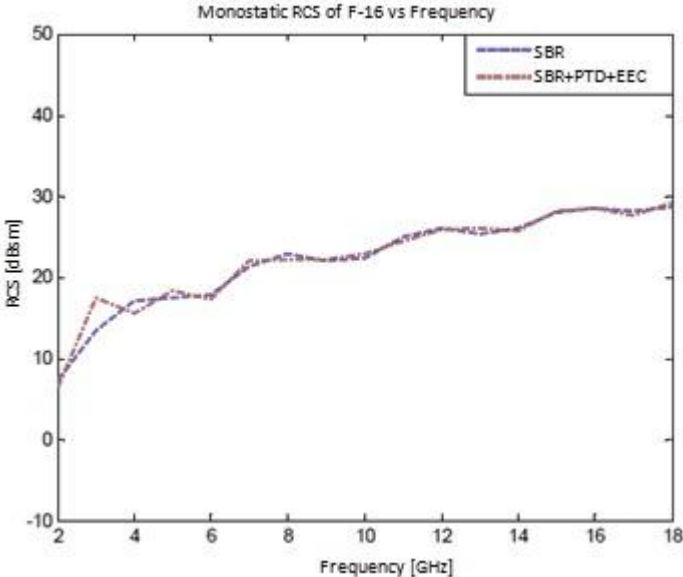
Figure 95 RCS of F-16 with respect to frequency with SBR, PTD and EEC at vertical polarization

As shown in Figure 95, diffraction effects are most dominant at frequency (θ) interval of [2-5] GHz. In other frequency ranges, since diffraction effects are weak, SBR, PTD and EEC results are compatible with SBR results

CHAPTER 5

MODELLING AND RCS SIMULATION OF AIRCRAFT COCKPIT

In the literature, rectangular cavity was used to represent a structure such as a cockpit in an air vehicle and has been flush mounted in the sidewall of a finite circular cylinder **[27, 28]**. In this study, fuselage of the air vehicle is modeled as finite elliptical cylinder and a large cavity is mounted inside the finite elliptical cylinder. Shooting and bouncing ray method is used for the cavity, and finite elliptical cylinder effects were accounted for via the Uniform Geometrical Theory of Diffraction (UTD) and Shooting and Bouncing Ray (SBR) method. RCS of cylindrical cockpit and rectangular cavity have been investigated at a frequency interval of [1-12] GHz.

5.1 Radar Cross Section of a Rectangular Cavity in a Finite Cylinder

In this section, effects of scattering from cylindrical surface superposed on rectangular cavity on RCS is investigated. In literature, cockpit of the aircraft is modeled as a rectangular cavity inside finite cylindrical surface. **[28]**
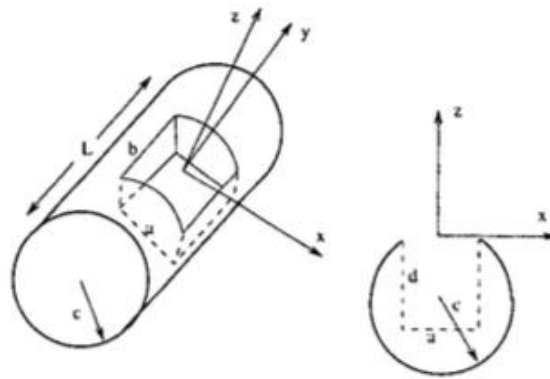
Figure 96 Cylinder with a flush mounted rectangular cavity. The cavity extends over $-\frac{a}{2} \leq x \leq \frac{a}{2}, -\frac{b}{2} \leq y \leq \frac{b}{2}, -\mathbf{d} \leq \mathbf{z} \leq \mathbf{0}$. The cylinder length=L and radius=c.

Aperture integration (AI) of the waveguide modes was used for the cavity. Creeping wave effects were accounted for via the Uniform Geometrical Theory of Diffraction (UTD). External scattering from the cylinder was handled by curved edge GTD. This AI/UTD technique was previously used for a cavity in a finite, flat ground plane **[2]**.

5.1.1 Diffraction Mechanisms and Model

Three diffraction mechanisms are considered. RCS due to

(a) the cavity,

(b) creeping wave interactions of the cavity and cylinder, and

(c) exterior scattering by the cylinder edges."

This is shown in Figs. 97 and 98. **"The cavity contribution (a) is found by using propagating waveguide modes to obtain the equivalent magnetic currents in the aperture. Then, aperture integration is used to obtain the radiated field. Reciprocity is applied [27]** to obtain the solution for cavity excitation by a plane wave. Combining the results gives us the RCS due to cavity effects. The interaction (b) of the cavity and cylinder is readily incorporated by using UTD **[27]** The creeping waves, when added to AI, provide an improvement beyond the $\theta = 90°$ direction.

108

The exterior diffractions (c) originate from the edges of the cylinder and aperture. Interactions with the waveguide modes are not part of this process. The effect is included via curved edgc GTD **[28]**. Other methods are possible. *e.g.* PO/PTD. Such refinements were deemed to be not, worthwhile for this application
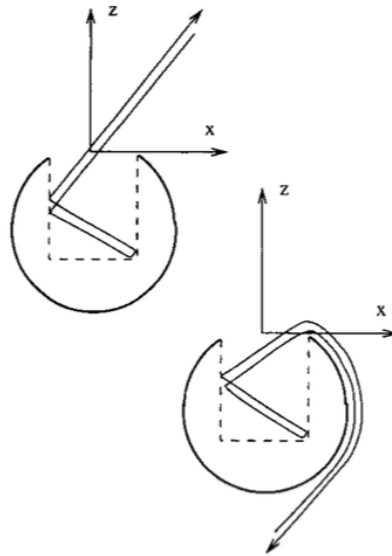
Figure 97 Excitation of cavity modes via topside and bottom side illumination.
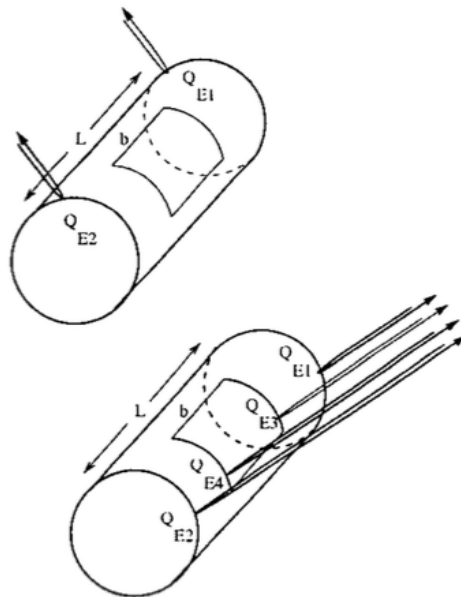
Figure 98 External scattering by the cylinder, showing the possibility of two or four diffraction points. The cylinder has a length=*L*, and aperture length=*b*.

5.1.2 Results and Discussion

The AI/UTD were used to compute the monostatic RCS in the $\emptyset = 0$ plane for a 1 by 1 m aperture in a cylinder. The cavity depth is 2 m and the frequency is 5 GHz. The cylinder radius is 2.5 m and the length is 5 m.

Fig. 99 shows $RCS_{\emptyset\emptyset}$ and $RCS_{\theta\theta}$ using AI/UTD. The external part of the geometry can be interpreted as a cylinder with an absorbing cavity. The total RCS represents a cylinder with a perfectly reflecting cavity. We also note that the cylinder RCS has a discontinuity; this is due to the appearance/disappearance of the diffraction points Q_{E3} and Q_{E4}, in Fig. 96. In the shadow, region $\theta \geq 90°$, creeping waves couple into the cavity, reflect, and then reradiate. This effect is very weak as compared to the cylinder's external scattering
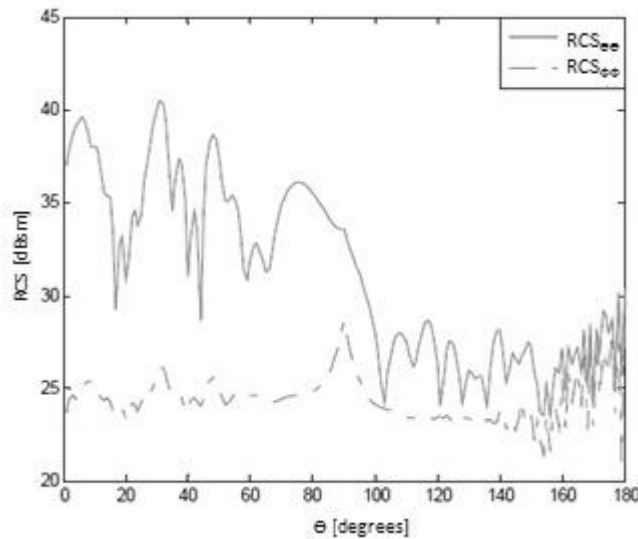
Figure 99 Monostatic RCS of the finite cylinder with a rectangular cavity using AI/UTD
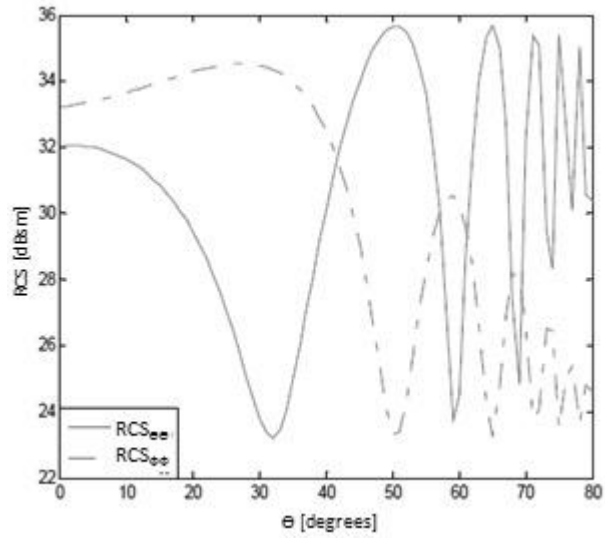
Figure 100 Monostatic RCS of the finite cylinder with a rectangular cavity using SBR

Fig. 100 shows $RCS_{\emptyset\emptyset}$ and $RCS_{\theta\theta}$ using SBR. There is a phase difference of $180°$ between horizontal and vertical polarizations in angular ranges other than $\theta = [0° - 20°]$. Also, as θ increases $RCS_{\theta\theta}$ component increase whereas $RCS_{\emptyset\emptyset}$ component decreases.

CHAPTER 6

CONCLUSIONS

6.1 Summary of the Thesis

In the scope of this study, a MATLAB code has been developed in order to calculate radar cross section of compex shapes using shooting and bouncing rays method.

Shooting and bouncing rays method is a ray tracing method based on geometric optics (GO) and phyical optics (PO) methods. Ray paths are calculated by geometric optics, whereas the interaction of surface currents and electric field is handled by physical optics. Aperture integration (AI) method is also adopted.

Wave frequency, number of rays shot into the target, polarization of the wave, target geometry and aspect angle are the major input parameters of the code. Based on these parameters, the code predicts the RCS of a complex shape.

SBR code can handle reflaction effects which mainly occur due to specular surface returns. Diffraction, on the other hand, occurs whenever an incident ray comes accross an edge or a corner. Edge and corner diffraction mechanisms are mainly handled by diffraction theories such Physical Theory of Diffraction, Geometric Theory of Diffraction (GTD)) and Uniform Theory of Diffraction (UTD). Equivalent Edge Currents (EEC's), recently developed by Michaeli, is another method that can handle diffraction effects. EEC method is used in the scope of this study. Therefore, it can be concluded that, the code developed is a hybrid of SBR and EEC.

In order to validate the code, RCS of some primitive shapes such as flat square, cylinder, and corner reflector is calculated and compared with the values pulished in

the literature. Complex shapes, on the other hand, are decomposed into planar triangles and saved as STL formats. The code performs ray-traingle intersection test and based on the results of intersection tests, calculates the contribution of each triangle. Finally, RCS of the whole target is calculated by summing up the contribution of each ray. This is performed in the aperture integration phase. Complex shapes that are analyzed in the scope of the study are F-16, F-117 and eurofighter aircrafts.

Since SBR is a ray tracing based approach, a fast ray-triangle intersection test algorithm shall be utilized to enhance SBR method. Badouel, Moller-Trumbore and Plucker methods have also been implemented for ray-triangle intersection test in various problems involving targets consisting of large number of triangular plates. As a result of the study, it is concluded that Plucker test method yields lower computation times than other two intersection test methods.

Results obtained by PO, SBR and SBR+EEC methods for complex and primitive shapes have been compared and differences have been examined. While the above mentioned codes provide perfect matches at regions where specular surface returns are dominant, significant deviations between the results arise at regions where diffraction effects are dominant.

In the scope of this study, contribution of a rectangular shaped cockpit inside a circulor shaped aircraft fuselage to the RCS of the aircraft has been analyzed using the methods in the literature.

Finally, all the analysis conducted under this study have been performed based on 'Perfectly Electric Conducting (PEC)' material assumption. Therefore the planar reflection coefficient is assmued to be 1. Effect of radar absorbing materials is not taken into consideration.

6.2 Discussion and Future Work

Electromagnetic analysis methods based on ray tracing or physical optics approaches such as SBR are approximate techniques. While external excitations can be modeled by these techniques, internal excitations cannot be handled. On the other hand, approximate techniques can provide fast results with relatively low computation

effort. Full wave solution techniques, also called current based techniques such as Method of Moments (MoM), Multi Level Fast Multipole Method (MLFMM) and Finite Element Method (FEM) do not include any approximations but require higher computation power and provide more accurate results compared to the above mentioned simpler approximate techniques.

In order to obtain faster and more accurate results, approximate and full wave techniques can be combined resulting in a hybrid method. This approach can also provide a solution of the diffraction problem.

Use of radar absorbent materials in the future fighter aircrafts is inevitable. Therefore any RCS code should be compatible of solving problems that include dielectric materials. This can be achieved through the development of dielectric material attenutaion models and modifying planar reflection coefficients used in electric field integrals.

BIBLIOGRAPHY

[1] Meng H. 2011., Acceleration of Asymptotıc Computational Electromagnetics Physical Optics – Shooting And Bouncing Ray (PO-SBR) Method Using CUDA, Graduate College of the University of Illinois at Urbana-Champaign.

[2] Ling H., Chou R. ve Lee S.W., 1989, Shooting and Bouncing Rays: Calculating the RCS of an Arbitrarily Shaped Cavity, IEEE Trans. on Antennas and Propagation, vol. AP-37, no.2, pp.194-205.

[3] Ling H., Lee S.W. ve Chou R.C., 1989, High Frequency RCS of Open Cavities with Rectangular and Circular Cross Section, IEEE Trans. AP-S, pp.648-654.

[4] Altıntaş A., Pathak P.H. ve Liang M.C., 1988, A Selective Modal Scheme for the Analysis of EM Coupling Into or Radiation from Large Open-Ended Waveguides, IEEE Trans. Antennas and Propagat., Vol. 36, No.1, January 1988, pp.84-96.

[5] Baldauf J., Lee S.W., Lin L., Jeng S.K., Scarborough S.M., Yu C.L., 1991,High Frequency Scattering from Trihedral Corner Reflector and Other Bechmark Targets: SBR versus Experiment, IEEE Trans. Antennas and Propagation., Vol. 39, No.9, September, pp.1345-1351.

[6] Badouel, F., 1990, An Efficient Ray-Polygon Intersection, Graphic Gems, Academic Press, pp.390-393.

[7] Moller T. ve Trumbore B., 1997, Fast, Minimum Storage Ray/Triangle Intersection.Journal of Graphics Tools 2(1), 21–28.

[8] Pathak P.H., Burnside W.D. ve Marhefka R.J., 1980, A Uniform GTD Analysis of the Diffraction of Electromagnetic Waves by a Smooth Convex Surface, IEEE Trans. Antennas and Propagat., vol. AP-28, no.5, September, pp.631-642.

[9] Paknys R., Kashyap S. ve Louie A., 2001, Radar Cross Section of a Rectangular Cavity in a Finite Cylinder, IEEE AP-S International Symposium, Orlando, FL, pp. 718-721.

[10] Michaeli A., 1984, Equivalent Edge Currents for Arbitrary Aspects of Observation, IEEE Trans. on Antennas and Propagation, vol.AP-32, no.3, March, pp.252-258.

[11] Shevtsov M., Soupikov A. ve Kapustin A., 2007, Ray-Triangle Intersection Algorithm for Modern CPU Architectures, GraphiCon'2007 Russia, Moscow, June 23-27.

[12] Shoemake, K., 1998, Plucker Coordinate Tutorial. Ray Tracing News 11(1).

[13] Erickson, J., 1997, Plucker Coordinates. Ray Tracing News 10(3).

[14] Huang C.C., Pathak P.H., Lai C.Y. ve Moffatt D., 1982, Analysis of Electromagnetic Backscatter from an Inlet Cavity Configuration, Ohio State University ElectroScience Laboratory Tech. Rept. 712661, prepared for Hanscom AFB, Oct.

[15] Mittra R., Lee J., 1993, Aoyagi P., A hybrid Yee algorithm/scalar-wave equation approach, Microwave Theory and Techniques, IEEE Transactions.

[16] Chu F., Huang C., 1989, On the calculation of the Fourier transform of a polygonal shape function, J. Phys. A: Math. Gen. 22 L671.

[17] Mitzner K.M., 1974, Incremental Length Diffraction Coefficients, Aircraft Division Northrop Corp. Tech. Rep. AFAL-TR-73-296, Apr.

[18] Shore R. and Yaghjian A. D., 1989, "Correction to 'Incremental diffraction coefficients for planar surfaces,'" IEEE Trans. Antennas Propugat., vol. 37, p. 1342, Oct..

[19] Breinbjerg 0., 1992, "Higher order equivalent edge currents for fringe wave radar scattering by perfectly conducting polygonal plates,'' IEEE Trans. Antennas Propagat., vol. 40, pp. 1543-1554, Dec..

[20] Johansen P. M., 1996, ''Uniform Physical Theory of Diffraction Equivalent Edge Currents for Truncated Wedge Strips'', IEEE transactıons on antennas and propagatıon, vol. 44, no. 7.

[21] Michaeli A., 1987 ,"Equivalent currents for Tecond-order diffraction by the edges of perfectly conducting polygonal surfaces," IEEE Trans. Antennas Propagat., vol. AP-35, pp. 183-190, Feb.

[22] Johansen P. M., 1995, "Physical theory of diffraction equivalent edge currents for truncated wedge strips," Rome Lab. Rep. RL-TR-958.217, Hanscom AFB, MA

[23] Gennarelli C. and Palumbo L., 1984,"A uniform asymptotic expansion of a typical diffraction integral with many coalescing simple pole singularities and a first-order saddle point," IEEE Trans. Antennas Propagat., vol. AP-32, pp. 1122-1124.

[24] Felsen L. B. and Marcuvitz N., 1973, Radiation und Scattering qf Waves. Englewood Cliffs, NJ: Prentice-Hall, , ch. 4.

[25] Hansen T. B., "Corner diffraction coefficients for the quarter plane,"IEEE Trans. Antennas Propagat., vol. 39, pp. 976-984, July 1991.

[26] Balanis A.C. ve Polka L.A., 1989, Non-principal Plane Scattering from Perfectly Conducting, Flat, Rectangular Plates, Antennas and Propagation Society International Symposium, AP-S. Digest, vol. 3, pp. 1278 – 1281, 26-30 Jun.

[27] Paknys, R., S. Kashyap, and A. Louie, \Radar cross section of a rectangular cavity in a finite cylinder," IEEE AP-S International Symposium, 718{721, Orlando, FL, 2001.

[28] Paknys, R., F. Hyjazie, S. Kashyap, and A. Louie, \Radar cross section of a rectangular cavity in a finite ground plane," IEEE AP-S International Symposium, 2842{2845, Orlando, FL, July11- 16, 1999.

[29] McNamara, D. A., C. W. I. Pistorius, and J. A. G. Malherbe, Introduction to the Uniform Geometrical Theory of Di®raction, Artech House, Boston, 1990.

[30] Pathak, P. H., W. D. Burnside, and R. J. Marhefka, \A uniform GTD analysis of the diffraction of electromagnetic waves by a smooth convex surface," IEEE Trans. on Antennas and Propagat., Vol. 28, No. 5, 631{642, September 1980.

[31] Casciato, M. D. and K. Sarabandi, ''High-frequency radio wave diffraction from singly curved, convex surfaces | A heuristic approach'' IEEE Proc. - Microw. Antennas Propag., Vol. 151, No. 1, 43{53, February 2004.

CURRICULUM VITAE

PERSONAL INFORMATION

Surname, Name: Çakır, Mustafa Kağan

Nationality: Turkish (TC)

Date and Place of Birth: 3 August 1983, Ankara

Marital Status: Married

Phone: +90 505 552 41 92

email: kagan.cakir@gmail.com

EDUCATION

Degree	Institution	Year of Graduation
MSc.	METU Mechanical Engineering	2008
BSc.	METU Mechanical Engineering	2005
High School	Ankara Gazi Anadolu High School	2001

WORK EXPERIENCE

Year	Place	Enrollment
2005 - Present	TUSAŞ Aerospace Industries Inc.	Technical Specialist
2004	Bosch Sanayi Ve Ticaret A.S.	Intern Eng. Student
2003	Türk Traktör A.Ş.	Intern Eng. Student

FOREIGN LANGUAGES

Advanced English, Intermediate German